THE DESIGN OF A MOBILE SYNTHETIC APERTURE COLLIMATED GAMMA DETECTOR FOR PASSIVE HEU SOURCES

A Thesis
Presented to
The Academic Faculty

by

Michael Raymond Chin

In Partial Fulfillment
of the Requirements for the Degree
Masters of Science in Nuclear Engineering in the
Woodruff School of Mechanical Engineering

Georgia Institute of Technology
August 2013

THE DESIGN OF A MOBILE SYNTHETIC APERTURE COLLIMATED GAMMA DETECTOR FOR PASSIVE HEU SOURCES

Approved by:

Dr. Glenn Sjoden, Advisor
School of Nuclear and Radiological Engineering
Georgia Institute of Technology

Dr. Nolan Hertel
School of Nuclear and Radiological Engineering
Georgia Institute of Technology

Dr. Chaitanya Deo
School of Nuclear and Radiological Engineering
Georgia Institute of Technology

Dr. Ce Yi
School of Nuclear and Radiological Engineering
Georgia Institute of Technology

Date Approved: June 14, 2013

This thesis is dedicated to my mother and father, Marie Kretschmar and Trevor Chin, for their support has fostered a personal lifelong love of science. I would also like to thank Effie White for helping me through the stress of the Ph.D. qualification exam and for helping me proofread this thesis.

ACKNOWLEDGEMENTS

Special thanks goes to Kevin Manalo for various sanity checks on my work and for being available to bounce ideas as well as various technical support. I would also like to thank my advisor, Dr. Sjoden, for guiding my endeavors into the realm of science and nuclear engineering. I would also like to thank my committee members, Dr. Nolan Hertel, Dr. Chaitanya Deo, and Dr. Ce Yi, for volunteering to oversee the merits of this work.

TABLE OF CONTENTS

LIST OF TABLES

LIST OF FIGURES

SUMMARY

This thesis covers the individual work of Michael Chin as part of the sponsored research project funded by the U.S. State Department in support of a computational design of a "Mobile Pit Verification System" (MPVS), a mobile “drive by” passive radiation detection system to be applied in Special Nuclear Materials (SNM) storage facilities for validation and compliance purposes. The MPVS system is intended to enable a comprehensive, rapid verification and validation of stored nuclear weapon core physics packages containing SNM, or so-called “weapon pits,” in weapon materials and stockpile storage facilities. The MPVS platform is designed to move at a constant speed and accumulate a signal for each stored weapon pit container. The gamma detector was selected to be a $4 \times 4 \times 8$ cubic inch CsI detector while the neutron detector array designed for the “Transport Simulation and Validation of a Synthetic Aperture SNM Detection System (T-SADS).” The T-SADS project was used in conjunction with this work. The T-SADS project was a 3 year effort funded by the Department of Energy/National Nuclear Security Administration (DOE-NNSA), which was completed on May 2013.

The computational design effort for this project was completed in April 2013, and leveraged novel computational radiation transport methods, algorithms, and SNM identification methods. This included a synthetic aperture collection approach, and a new gamma ratio methodology for distinguishing between Naturally Occurring Radioactive Materials (NORM) and weapon class SNM materials. Both forward and adjoint transport methods were utilized to characterize the adjoint reaction rate as a function of inter-

source spacing, collimation thickness, linear and angular field of view, source age, source type, source geometry, and mobile platform speed. The integrated count was then compared with background radiation and the associated probabilities of detection and false alarm were then computed.

Publications resulting from this research were published in PHYSOR 2012, presented at the 53rd annual Proceedings of the International Nuclear Materials Management (INMM), and at the Mathematics & Computation 2013 Conference.

Chapter 1: Introduction

1.1. Introduction

The Mobile Pit Verification System (MPVS) is a mobile platform consisting of a five energy-group neutron block with three banked helium-3 tubes per neutron block and two 4 × 4 × 8 cubic inch Cesium Iodide (CsI) scintillating gamma detectors shown in Figure 1.1. The initial designs differed slightly from the finalized design in that the CsI detectors were 1 inch diameter cylinders, but for reasons discussed below the geometry was modified to a set of rectangular parallelepiped CsI detectors.

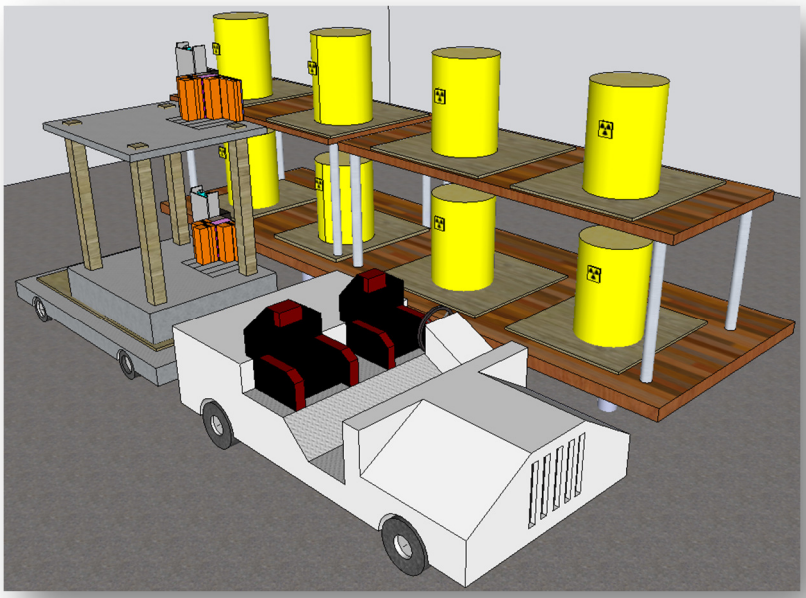

Figure 1.1: Conceptualization of the Mobile Pit Verification System with the dual 4 × 4 × 8 in^3 CsI gamma detector block and the five modular T-SADS neutron blocks being towed by a baggage tug. The system is looking at SNM canisters spaced one meter apart. All objects shown to scale.

This system was designed to characterize neutron and photon emissions from $^{235}_{92}U$, $^{238}_{92}U$, and $^{239}_{94}Pu$ sources and make estimations on the mass of SNM inside weapons pit

storage containers whose designs such as the AL-R8 and the AT-400A are available from open literature. To simplify our analysis, a hybrid model that has characteristics of both the AL-R8 [1] and the AT-400A [2] weapons pit storage containers were used for the SNM pit geometry. The gamma detector system is capable of incorporating a set of modular tungsten collimator plates to reduce Out-of-Field (OOF) photons from adjacent sources.

The initial set of uranium and plutonium source distributions were provided by the ORIGEN-ARP code by Oak Ridge National Laboratory (ORNL) [3] while the gamma cross sections were generated using the CEPXS library [4] for the variety of materials expected to be present in the source canister. The number of groups for the gamma photons was selected to be 24 with certain energy bins emphasizing certain key gamma lines present in $^{238}_{92}U$, such as the 1.001 MeV gamma line.

The adjoint reaction rate analysis took place in two distinct analysis steps: The first phase of the analysis involved characterizing the gamma radiation transport as it tracks through the various materials inside the SNM pit and is tallied as an output on the surface of the "source box"; the second phase of the analysis treats the output from the source box plane as an input streaming in the direction of the gamma detector. A few reference MCNP calculations were performed with both phases simultaneously modeled, i.e. the source canister and the detector platform were fully modeled.

The tungsten collimation was performed with a series of adjoint transport calculations where the adjoint reaction rate was summed over three regions of interest: In-Field, Mid-Field, and Out-of-Field (OOF). These photon count rates are then multiplied by a window of time that varies on multiple factors: Inter-source spacing,

angular and linear Field of View (FOV), and source-collimator distance. The In-Field photon tallies are then compared to rates of normal background radiation as a function of energy as well as the Out-of-Field tallies from which an optimal speed of detector movement can be deduced. A separate quasi-analytic and quasi-computational equation was formulated to provide an upper limit on the counts detected by leveraging the adjoint flux and geometric streaming terms while neglecting the effects of scattering and absorption.

The OOF contribution from adjacent sources can be generalized by tallying uncollided and collided photon fluence across the detector face and performing a transport correction calculation as a function of distance while in the presence of multiple sources. For simplification only three sources were considered with an inter-source spacing of one meter. This would represent one line of an SNM rack; current estimates from published literature indicate two racks of SNM would fit in a standard single-story room. Therefore it is possible to either bank multiple sets of detectors, each recording data from one SNM rack, or performing multiple passes with the same detector configuration.

The results from this analysis can then be used in conjunction with gamma line ratio techniques to validate the presence of SNM and determine whether or not any material has been diverted. Furthermore, this will allow concrete determination of quantities of SNM in kilograms and whether or not the spectral intensity corresponds to Highly Enriched Uranium (HEU) or plutonium. This would provide a significant improvement in current Materials Control & Accountability (MC&A) safeguards verification protocols since a rapid passive assessment from a moving detector platform

could, with over-the-counter electronics and detectors, characterize radiation signatures from SNM and determine the masses (from isotopic contributions to certain gamma energy bins) and rough geometric configuration of the sources inside.

1.2. SNM Canister Development

A hybridized model of the SNM canisters was developed from two canisters found in open literature: AL-R8 [1] and AT-400A [2]. The basic design consists of either a spherical shell of SNM or a solid ball of SNM with 1 Significant Quantity (SQ) masses of HEU (25 kg) or WGPu (8 kg) respectively. The radius of the sphere was adjusted so that the 1 SQ mass quantity was preserved across models. The SNM has a 1 cm aluminum cladding, and the SNM/cladding combination is positioned axially in the center of the 30 cm × 30 cm × 77.2 cm cylinder. There is an air gap between the cladding and a layer of polyethylene packing material (Celotex [5]) along the inner lining of the outer cylindrical shell. The cylindrical shell is made of stainless steel 316 (SS-316). For tallying purposes, two separate arbitrary "boxes" were considered: the inner source box and the outer source box. The inner source box is positioned to contain the SNM ball while the outer source box contains the entire SNM canister. Further information can be found in Section 3.4. Particular interest was paid to the YZ plane of the outer source box, as this surface will be directly modeled with the detector platform (see Section 3.7). The SNM canister was modeled both in MCNP and PENTRAN and tally data exist for both models along all surfaces of the inner and outer source box. Spatial distributions for the source exist (via the njdump option in PENTRAN) for the YZ and XY planes of the SNM canister in both MCNP and PENTRAN. The PENTRAN

models were originally modeled with S_{30} data, but were later ran with S_{42} data to reduce fine-mesh error from ray-effect.

Chapter 2: Theory and Application of Adjoint and Forward Transport

2.1. Background of Adjoint and Forward Transport

The basic form for a fixed source multigroup transport problem comes in the form shown in Eq. 2.1 and Eq. 2.2.

$$H\psi_g = q_g \qquad \text{Eq. 2.1}$$

$$H^{\dagger}\psi_g^{\dagger} = \sigma_{dg} \qquad \text{Eq. 2.2}$$

Where H and $H^{\dagger}$ are the multigroup forward and adjoint transport operators shown in Eq. 2.3 and Eq. 2.4, ψ_g and $\psi_g^{\dagger}$ are the forward angular flux $[\frac{particles}{cm^2\ sr}]$ and adjoint expected counts per particle (a unitless parameter which characterizes the particle "importance" relative to the detector located at position $\vec{r}$ with energy E_g and direction $\widehat{\Omega}$), respectively, and q_g is the fixed source magnitude in $[\frac{particles}{cm^3\ sr}]$, and σ_{dg} is the detector absorption cross section bounded from energy E_1 to E_G [6].

$$H = \widehat{\Omega}\cdot\nabla + \sigma_g(\vec{r}) - \sum_{g'=1}^{G}\int_{4\pi}\sigma_{s,g'\to g}\left(\vec{r},\widehat{\Omega}'\cdot\widehat{\Omega}\right)d\Omega' \qquad \text{Eq. 2.3}$$

$$H^{\dagger} = -\widehat{\Omega}\cdot\nabla + \sigma_g(\vec{r}) - \sum_{g'=1}^{G}\int_{4\pi}\sigma_{s,g\to g'}\left(\vec{r},\widehat{\Omega}\cdot\widehat{\Omega}'\right)d\Omega' \qquad \text{Eq. 2.4}$$

Note that the adjoint operator reverses the direction of streaming, and inverts the scattering group-to-group energy coupling and directional terms. It is important to note that the operator H is not self adjoint, that is:

$$\langle\psi\ H\phi\rangle \neq \langle\phi\ H\psi\rangle \qquad \text{Eq. 2.5}$$

Where ψ and ϕ are arbitrary functions of $\left(\vec{r}, E, \widehat{\Omega}\right)$ satisfying requisite boundary and continuity conditions [6]. Since Eq. 2.5 is not self-adjoint, it is possible to reformulate a version of Eq. 2.5 using a reciprocity relationship through the use of the adjoint operator shown in Eq. 2.4. The generalized optical reciprocity relationship [6] shows that for given volumetric unit sources $Q_1\left(\vec{r}, \widehat{\Omega}\right) = \frac{1}{V_1}\delta\left(\widehat{\Omega} - \widehat{\Omega}_1\right)$ and $Q_2\left(\vec{r}, \widehat{\Omega}\right) = \frac{1}{V_2}\delta\left(\widehat{\Omega} - \widehat{\Omega}_2\right)$ with

$$\iint Q_1\left(\vec{r}, \widehat{\Omega}\right)\Phi_2\left(\vec{r}, -\widehat{\Omega}\right)d\Omega dV = \iint Q_2\left(\vec{r}, -\widehat{\Omega}\right)\Phi_1\left(\vec{r}, \widehat{\Omega}\right)d\Omega dV \qquad \text{Eq. 2.6}$$

The rate of particle absorption in V_2 produced in V_1 is represented as:

$$P_{2\to1} = \sigma_1 \int_{V_1} \phi_2(\vec{r})\ dV \qquad \text{Eq. 2.7}$$

Likewise for the reciprocal case:

$$P_{1\to2} = \sigma_2 \int_{V_2} \phi_1(\vec{r})\ dV \qquad \text{Eq. 2.8}$$

This leads to the volumetric absorption optical reciprocity relation:

$$\sigma_2 V_2 P_{2\to1} = \sigma_1 V_1 P_{1\to2} \qquad \text{Eq. 2.9}$$

Eq. 2.9 is in a form that is analogous to the forward-adjoint reciprocity relationship in Eq. 2.10. However, this elementary formulation does not include particle fluxes and the "adjoint" term is embedded in the optical absorption probabilities $P_{2\to1}$ and $P_{1\to2}$.

2.2. Overview of Forward and Adjoint Response

By applying the principle of reciprocity through inverting the relationship between the source and detector (i.e. the forward source emits particles from the source to

the detector, while the adjoint source emits "detector response particles" toward the forward source and is aliased to the detector via the detector response cross section) leads to the reciprocity relationship between forward and adjoint:

$$\langle \psi^{\dagger} H \psi \rangle = \langle \psi H^{\dagger} \psi^{\dagger} \rangle \qquad \text{Eq. 2.10}$$

The angular forward flux is subject to the free-surface convex boundary conditions $\psi\left(\vec{r}, E, \widehat{\Omega}\right) = 0 \ \forall \ \hat{n} \cdot \widehat{\Omega} < 0$. Likewise for the adjoint flux, $\psi^{\dagger}\left(\vec{r}, E, \widehat{\Omega}\right) = 0 \ \forall \ \hat{n} \cdot \widehat{\Omega} > 0$ where the transport operators H and $H^{\dagger}$ are both continuous functions of space [6].

By substituting Eq. 2.3 and Eq. 2.4 into Eq. 2.10 we obtain the Reaction Rate Equivalency between forward and adjoint reaction rates:

$$R\left[\frac{particles}{second\ basis}\right] = \langle \psi_g \sigma_{dg} \rangle = \langle \psi_g^{\dagger} q_g \rangle \qquad \text{Eq. 2.11}$$

Using variations of Eq. 2.11, the reaction rate can be computed using alternatives based on leakage emission by expanding the "basis" in Eq. 2.11 in terms of area (via current importance coupling) or volume (via scalar flux/importance coupling). Note the volumetric basis does not utilize a μ directional cosine as is needed in a current coupled response term that is, by definition, part of the current term. For the purposes of our analysis, a reaction rate for a volumetric source basis was considered, since a volumetric source was constructed as an artificially thin volumetric source placed in characteristically low density ($1.203 \times 10^{-3} \frac{g}{cm^3}$) ANSI dry air medium.

The volumetric basis reaction rates can be calculated via Eq. 2.12 and Eq. 2.13 for forward and adjoint reaction rates respectively.

$$R_{fwd} = \langle \varphi \sigma_d \Delta V_d \rangle \quad \text{Eq. 2.12}$$

$$R_{adj} = \langle \varphi^{\dagger} q_{fwd} \Delta V_s \rangle \quad \text{Eq. 2.13}$$

In the most general terms, full angular fluxes can be used; however, a typical convention is to integrate over all angles to yield scalar values, so that φ is the scalar flux $(\frac{photons}{cm^2\ s})$, σ_d is the isotropic detector absorption macroscopic cross section $(\frac{1}{cm})$, and ΔV_d is the detector volume (cm^3). Regarding Eq. 2.13, $\varphi^{\dagger}$ is the scalar adjoint importance (unitless), q_{fwd} is the volumetric forward source $(\frac{photons}{cm^3\ s})$, and ΔV_s is the source volume (cm^3).

Likewise, the same can be written for the adjoint current basis response reaction rates:

$$R_{adj} = \left\langle {J^{\dagger}}^{+} q^{-}_{fwd} \Delta A_s \right\rangle \quad \text{Eq. 2.14}$$

Where J^{+} is the forward current $(\frac{particles}{cm^2\ s})$ streaming from the surface source, σ_d is the isotropic detector absorption macroscopic cross section $(\frac{1}{cm})$, and ΔV_d is the detector volume (cm^3). Likewise for the adjoint case: ${J^{\dagger}}^{+}$ is the adjoint current $(unitless)$ streaming from the detector face, the q^{-}_{fwd} term is the forward source divided by the source area $(\frac{particles}{cm^2\ s})$, and ΔA_s is the area of the source plane coupling both regions (cm^2). Note that the forward current implies a negative directionality (that is, the source emits particles in the –X direction) which is coupled with the adjoint current with positive directionality (that is, the adjoint source emits "particles" in the +X direction). This was the case for our analysis.

2.3. Time-Gating and Background Treatment

One of the strategies used to maximize the counting rate at the detector is to time-gate the signal by selectively turning on the detector whenever it is in the FOV of the detector. This minimizes the count rate from other adjacent sources (although it does not completely eliminate it) as shown in Section 5.6. This also allows us to make an assumption about the time-independence of the models by validating a steady state calculation without having to calculate any functional time dependence. In other words, an adjoint steady state calculation can be performed and the reaction rates (photons per second) can then be multiplied by the amount of time spent during the time gating process in order to achieve an absolute count. This count is then checked against the background spectra for certain energy lines of interest to see if it passes the threshold for statistical significance.

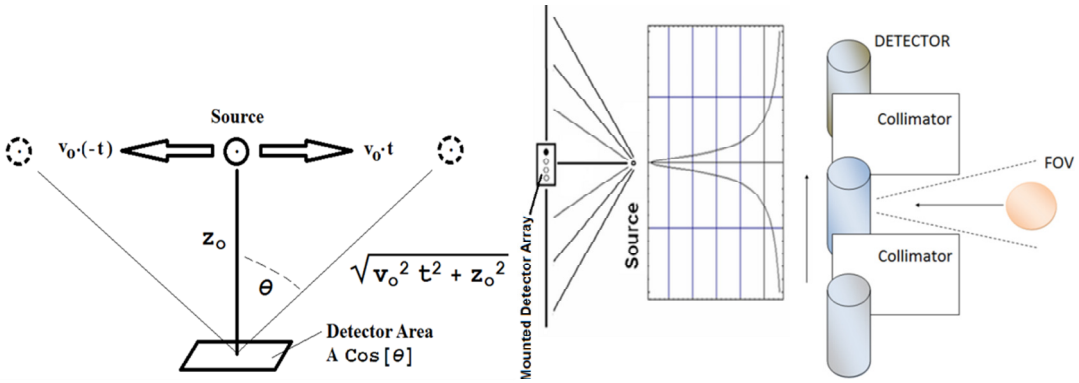

Figure 2.1. MPVS Concept, where the flat detector area shown (at Left) must be collimated as it moves past the SNM Source container, and detectors move past the source within a fixed gate time, where most all counts are recorded in close proximity to the source, as is shown on a normalized scale (Center). To prevent interference from other sources, collimators (shielding) must surround the detectors (shown at Right). If required, depending upon background interference count rates, multiple detector "trains" must be used to pass by the source with time gating and count integration, detecting when the source and detector are in the proper "Field of View" (FOV), delimited by the collimation; the minimum detector accumulation of radiation counts ("signal") from an SNM source is determined from vehicle speed.

In a single instant of time, the number of incident neutrons or gammas arriving (uncollided) on the detector front surface can be estimated with Eq. 2.15.

$$R_g(x) = \frac{(S_g)}{4\pi({z_0}^2 + x^2)} A_d cos\theta = \frac{(S_g)}{4\pi({z_0}^2 + x^2)} \frac{(A_d\ z_0)}{({z_0}^2 + x^2)^{1/2}} \qquad \text{Eq. 2.15}$$

Where:

- $R_g(x)$ is the incident response ***rate*** *(#/sec)* for energy group *g* for an SNM source located at position *x; x* is tangent to the vehicle path.
- $x = v_0 t$ is the distance from SNM to the center of the Field of View (FOV), where v_0 is the detector platform speed.
- S_g is the number of source particles for energy group *g (#/sec)*;
- θ is the source-detector angle (degrees), up to a maximum detector-FOV angle bounded by a competing source adjacent to the source undergoing a scan (as shown in Figure 2.1).
- A_d is the area of the detector front surface.
- z_0 is the fixed distance to the shelved SNM source.

Note that in Eq. 2.15, $({\mathrm{z}_0}^2 + \mathrm{x}^2)$ is the distance squared from the detector to the SNM, and $\frac{(\mathrm{A}_d\ \mathrm{z}_0)}{({\mathrm{z}_0}^2+\mathrm{x}^2)^{1/2}}$ is the cosine-projected detector front surface area viewed relative to a minimum fixed detector-SNM distance direction. The peak *rate* at a detector face C_{peak} is obtained from:

$$C_{peak} = \lim_{x \to 0} R_g(x) = \left(\frac{\mathrm{S}_g \mathrm{A}_d}{4\pi {\mathrm{z}_0}^2}\right) \qquad \text{Eq. 2.16}$$

To properly estimate the number of incident particles (neutrons or gammas), if the SNM source area is small compared to the separation distance (which can be corrected for with a transport correction function if this is not the case) and most of the region between SNM and detector is filled with air, the total counts that could be detected can be determined from the integration of Eq. 2.15 over the gate time interval $[-\tau, \tau]$ when the

detector platform crosses the detector FOV (with a minimum source-detector distance at time $\tau = 0$):

$$C_{g,uncollided} = \int_{-\tau}^{\tau} dt\, R_g(x) = \int_{-\tau}^{\tau} dt \frac{\mathrm{S}_g}{4\pi(\mathrm{z_0}^2 + (\mathrm{v_0 t})^2)} \frac{(\mathrm{A}_d\ \mathrm{z_0})}{(\mathrm{z_0}^2 + (\mathrm{v_0 t})^2)^{1/2}} \quad \text{Eq. 2.17}$$

Or, completing the integration analytically, with $L = v_0\ \tau$ being the "half time distance," the path length covered over the time for the platform to pass at the vehicle speed to cover half of the maximum FOV; the total path traveled is 2L, from [-L,L]:

$$C_{g,uncollided} = \frac{S_g A_d}{4\pi {z_0}^2} \left(\frac{2Lz_0}{v_0({z_0}^2 + L^2)^{1/2}} \right) = \quad C_{peak} \left(\frac{2Lz_0}{v_0({z_0}^2 + L^2)^{1/2}} \right) \quad \text{Eq. 2.18}$$

Simplifying the second term in Eq. 2.18, this is effectively a cosine corrected counting time:

$$T_p = \frac{2L}{v_0} \left(\frac{z_0}{({z_0}^2 + L^2)^{1/2}} \right) = T_r \left(\frac{z_0}{({z_0}^2 + L^2)^{1/2}} \right) = T_r \cos\theta_{max} \qquad \text{Eq. 2.19}$$

Where $\left(T_r = \frac{2L}{v_0}\right)$ is the "Real" Counting Time and θ_{max} is the maximum slant angle for the path geometry as noted. Therefore, T_r is the total time period when the detector array platform is moving through the detector FOV over the gate time $[-\tau, \tau]$ accumulating counts from the SNM source storage container package.

As an example, considering L = 90 cm, and v_0= 5 mph = 223.52 cm/s, with z_0=40 cm, $T_r = 0.805$ s and $T_p = 0.327$ s; for 2.5 mph = 111.8 cm/s, $T_r = 1.610$ s and $T_p = 0.654$ s. Given that these times are very short, depending upon the background, and source terms, several detector modules may be required to integrate the signal as the detector train passes a source; this will be investigated in this work with real source terms and transport calculations with coupled detector response. A practical count time for

consideration is on the order of a range from 0.25 to 0.75 seconds, depending upon Field of View versus vehicle speed, or an average of ~0.5 seconds of background accumulation.

Multiple time-gated detectors operating on the mobile platform forms an enlarged "synthetic aperture" detector if detector signals are summed with respect to each energy bin. If the source signature has low intensity and/or must reject a high background, the synthetic aperture approach enables verification of the SNM presence with respect to the Currie limit as the detector platform vehicle passes each SNM source at speeds that make the system tractable for rapid, large scale facility monitoring.

With a synthetic aperture approach, accumulation of a background signal can be minimized, while simultaneously minimizing signal to noise ratio with time gating. To obtain a satisfactory signal to noise response from passive collection, multiple detectors should be mounted and collimated on the MPVS vehicle. As vehicle speeds or mean backgrounds increase, more detectors forming the synthetic aperture could be required. The required number of detector assemblies is determined by a number of factors, such as the SNM mass and type, distance to the detector, inter-source spacing, angular and linear FOV, detector platform speed, and background count rate.

To outline an approach to determine the number of the detector assemblies we employ the traditional Currie Detection Limit formulation shown in Knoll [7]. To integrate a normalized Gaussian to yield 95% of the area, the limits needed are $\pm 1.96\ \sigma$ from the central mean (maximum). Based on the procedure outlined by Currie, the decision threshold will be established by, and is significantly dependent upon, the local detector background signal. Principally, we can assume that the total integrated counts

comes from signal plus background. Assuming the radiation signal is quite weak and difficult to distinguish from background, the number of detected counts is determined by subtracting the background counts from the total counts; the variance associated with this for the detected counts, by propagation of error is shown in Eq. 2.20:

$$\sigma_D{}^2 = \sigma_B{}^2 + \ \sigma_T{}^2 \approx 2\sigma_B{}^2 \qquad \text{Eq. 2.20}$$

Therefore, with $\sigma_B{}^2 = \dot{B}T_C$ the uncertainty in the detected counts can be expressed as:

$$\sigma_D \approx \sqrt{2\dot{B}T_C} \qquad \text{Eq. 2.21}$$

Where $\dot{B}$ = Background count rate and T_C = Counting time. Therefore, the Currie limit (L_C), depicted as the "Signal Decision Threshold Value" line in Figure 2.2, is established so that the minimum detectable activity for 5% ($1.96\ \sigma\ above\ the\ mean$) probability of false alarm (PFA) is:

$$L_C = 1.96\sqrt{2\dot{B}T_C} \qquad \text{Eq. 2.22}$$

In this case, the false alarm counts are not accounted for in the background variance (only up to 95% of the background area is accounted).

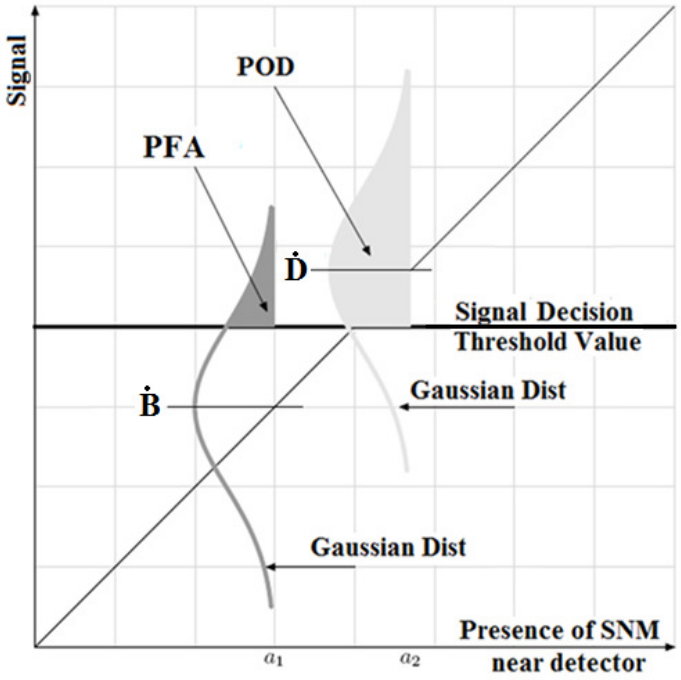

Figure 2.2: Contributions from counts depicting Probability of False Alarm (PFA) shown in dark grey and Probability of Detection (POD) shown in light grey for a given detection threshold. The distribution on the left is the background source while the distribution on the right is the source spectrum of interest.

Then, assuming real activity may be truly present, for a 95% probability of detection (POD), with propagation of error, the Real Activity Threshold counts is determined by:

$$N_T = L_C + 1.96\sqrt{2\dot{B}T_C + \dot{D}T_C} \qquad \text{Eq. 2.23}$$

Where:

- L_C = Currie limit number of counts attributed to background variance
- $\dot{B}$ = Background count rate
- T_C= Counting time (seconds)
- $\dot{D}$ = Detected count rate
- N_T= Real Activity Threshold Counts

The Real Activity Threshold Counts (N_T) may be expressed by using a fraction of background for the detected count rate, e.g.$\dot{D} \to 0.05\dot{B}$, or, in the limit that $\dot{D} \to 0$, then:

$$N_{T,min} = 1.96\left(2\sqrt{2\dot{B}T_C}\right) \qquad \text{Eq. 2.24}$$

The factors of 1.96 in Eq. 2.22 through Eq. 2.24 relate to the area of assumed Gaussian distributions to account for a 5% false alarm rate, and a 95% detection probability, respectively. We can consider T_C as the accumulated counting time from multiple detector assemblies:

$$T_C = n_d T_r \qquad \text{Eq. 2.25}$$

Where T_r is the real counting time for a single time gated detector assembly as used in Eq. 2.19, and n_d is the number of detector assemblies towed along the weapon pits using the MPVS inspection vehicle. In a later section, Section 4.15, we include a parameter study of vehicle speeds for this application. Choice of an appropriate time gate as the detector symmetrically passes the SNM source to be verified is key to minimizing signal to noise; this should be readily achievable by an RFID system and/or laser or optical triggering system on electronics.

Background gamma radiation was investigated based on a spectrum collected using a CsI(Na) detector 2" diameter and 3" length in a basement laboratory at the University of Florida [8]. The spectrum was corrected to a count-per-second basis with volume scaling for our larger detectors. The scaled spectrum is given in Figure 2.3 for the 60 cm long, 5.08 cm diameter CsI detector.

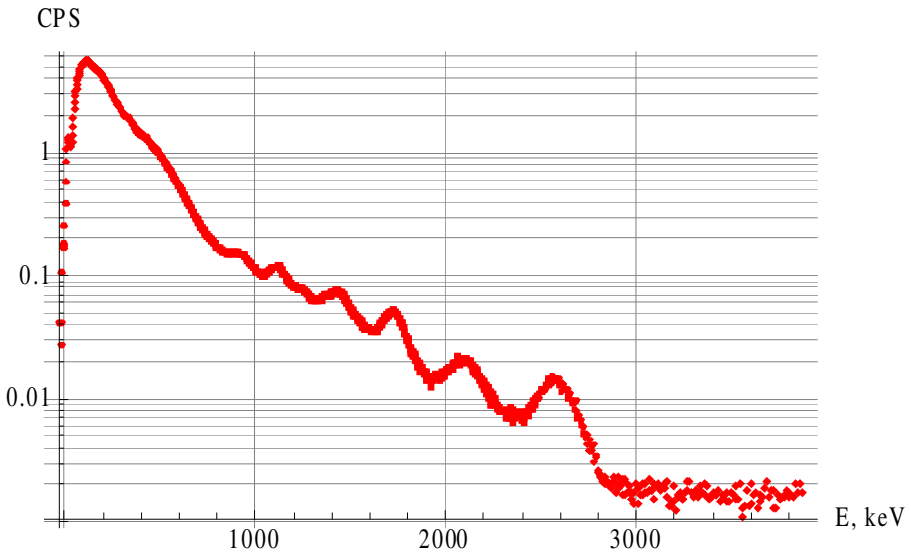

Figure 2.3: Contributions from background gamma radiation, as detected, in the detector, in CPS (counts per sec) vs. keV photon energy, scaled to detector design volume for a large, cylindrical MPVS CsI detector (5.08 cm dia x 60 cm tall); this is a representative background for initial assessments.

We applied the spectrum from Figure 2.3 as a representative background spectrum. This spectrum was used as a baseline, and we corrected the count conversion efficiency for detector response to yield the true counts observed by applying the gamma adjoint computed for this detector (presented later in Sections 4.8 and 4.9) over a 24 energy group structure (see Section 4.8). This is then tuned for energy bin isolation of specific gamma lines of interest for HEU and WGPu detection. The baseline true background exposure count rate was used to establish a Currie Limit (as in Eq. 2.22), and a minimum detectable threshold (Eq. 2.24), required to traverse the field of view in the mobile pit detector assuming a 0.5s integration time. The minimum integrated counts to warrant a detectable signature for the cylindrical CsI detector are presented in Table 2.1 below. Similar values for a $4 \times 4 \times 8$ in^3 CsI detector are shown in Table 2.2. Since the 999-1002 keV bin captures the 1001 keV line region of interest in energy Group 16,

values indicate approximately 4 to 5 total counts in this energy bin are required to achieve a floor for a detectable SNM signature at 1001 keV. This will be used later to highlight thresholds for vehicle speed with this design.

Table 2.1: (Left to Right) 24 Group structure for integrated Backgound counts for base background rate, Currie limit (5% PFA), and Minimum detectable rate limit (95% POD) for 60cm cylindrical detector; energy values indicate upper bin energy in keV; values below 300 keV were not considered.

Base Background, Bdot, CPS			Currie Limit, Background in 0.5s (Lc)			Count Det Limit in 0.5s (N_{tmin})		
Group	E, keV	BG, cps	Group	E, keV	Lc (0.5s)	Group	E, keV	N_{tmin} (0.5s)
1	2750	1E-04	1	2750	0.023	1	2750	0.047
2	2749	5.822	2	2749	4.729	2	2749	9.458
3	2250	0.652	3	2250	1.582	3	2250	3.165
4	2210	12.041	4	2210	6.801	4	2210	13.603
5	1832	0.016	5	1832	0.244	5	1832	0.488
6	1830	4.473	6	1830	4.145	6	1830	8.290
7	1760	1.926	7	1760	2.720	7	1760	5.440
8	1740	0.620	8	1740	1.543	8	1740	3.086
9	1736	20.451	9	1736	8.864	9	1736	17.727
10	1520	2.416	10	1520	3.046	10	1520	6.092
11	1500	38.196	11	1500	12.113	11	1500	24.227
12	1260	3.458	12	1260	3.645	12	1260	7.289
13	1240	8.348	13	1240	5.663	13	1240	11.326
14	1200	4.315	14	1200	4.072	14	1200	8.143
15	1180	54.066	15	1180	14.412	15	1180	28.824
16	1002	1.083	16	1002	2.040	16	1002	4.079
17	999	17.242	17	999	8.139	17	999	16.277
18	956	1.630	18	956	2.502	18	956	5.005
19	954	121.247	19	954	21.582	19	954	43.164
20	767	2.952	20	767	3.368	20	767	6.735
21	765	25.802	21	765	9.956	21	765	19.912
22	743	1.717	22	743	2.568	22	743	5.137
23	741	3890.870	23	741	122.259	23	741	244.517
24	300	0	24	300	0	24	300	0

Figure 2.4 depicts the adjoint based detector efficiency for gamma detection computed for the cylindrical detector.

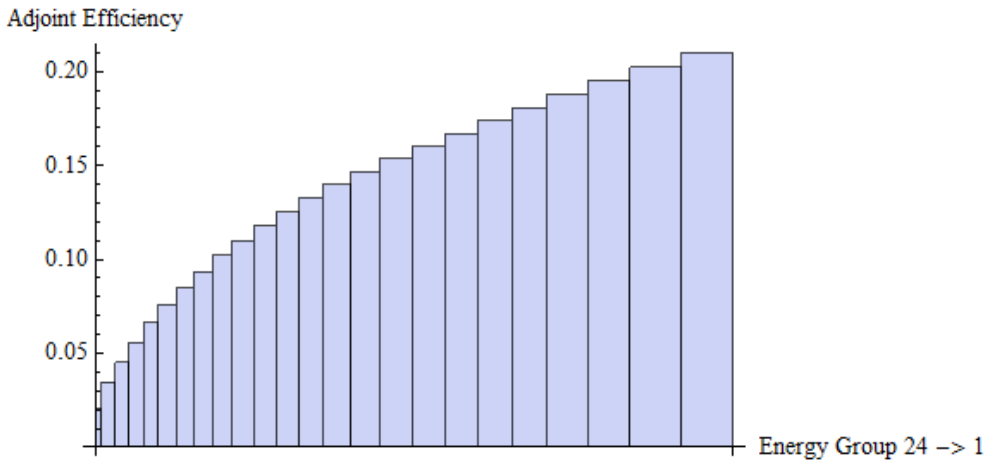

Figure 2.4: Adjoint efficiency of 60 cm 5.08 cm diameter detector with increasing energy and decreasing group number. (Group energy bins can be found in Table 3.2)

Table 2.2: (Left to Right) 24 Group structure for integrated Backgound counts for base background rate, Currie limit (5% PFA), and Minimum detectable rate limit (95% POD) for 4 × 4 × 8 in^3 CsI detector; energy values indicate upper bin energy in keV; values below 300 keV were not considered.

Base Background, Bdot, CPS			Currie Limit, Background in 0.5s (Lc)			Count Det Limit in 0.5s (N_{tmin})		
Group	E, keV	BG, cps	Group	E, keV	Lc (0.5s)	Group	E, keV	N_{tmin} (0.5s)
1	2750	1E-04	1	2750	0.020	1	2750	0.039
2	2749	8.365	2	2749	5.669	2	2749	11.338
3	2250	1.058	3	2250	2.016	3	2250	4.032
4	2210	18.968	4	2210	8.536	4	2210	17.073
5	1832	0.014	5	1832	0.230	5	1832	0.459
6	1830	6.929	6	1830	5.159	6	1830	10.319
7	1760	3.009	7	1760	3.400	7	1760	6.799
8	1740	0.939	8	1740	1.899	8	1740	3.798
9	1736	29.977	9	1736	10.731	9	1736	21.462
10	1520	3.514	10	1520	3.674	10	1520	7.349
11	1500	54.936	11	1500	14.527	11	1500	29.055
12	1260	4.766	12	1260	4.279	12	1260	8.557
13	1240	10.956	13	1240	6.488	13	1240	12.975
14	1200	5.468	14	1200	4.583	14	1200	9.166
15	1180	65.101	15	1180	15.814	15	1180	31.629
16	1002	1.205	16	1002	2.152	16	1002	4.304
17	999	17.472	17	999	8.193	17	999	16.385
18	956	1.496	18	956	2.397	18	956	4.795
19	954	99.201	19	954	19.522	19	954	39.043
20	767	2.102	20	767	2.842	20	767	5.683
21	765	15.079	21	765	7.611	21	765	15.222
22	743	0.456	22	743	1.324	22	743	2.648
23	741	1294.390	23	741	70.516	23	741	141.032
24	300	0	24	300	0	24	300	0

Figure 2.5 depicts the adjoint based detector efficiency for gamma detection computed for the $4 \times 4 \times 8$ in^3 CsI detector. Comparing this with Figure 2.4 shows that the gamma detection efficiency of this detector is superior to that of the cylindrical detector design; the profile is flatter across the entire energy spectrum with the exception of the highest two energy groups. As seen in later sections of this thesis, the adjoint efficiency is also greater in the $4 \times 4 \times 8$ in^3 CsI detector compared to the $2 \times 4 \times 8$ in^3 CsI detector since the added thickness increases the effective count rate in the higher energy bins.

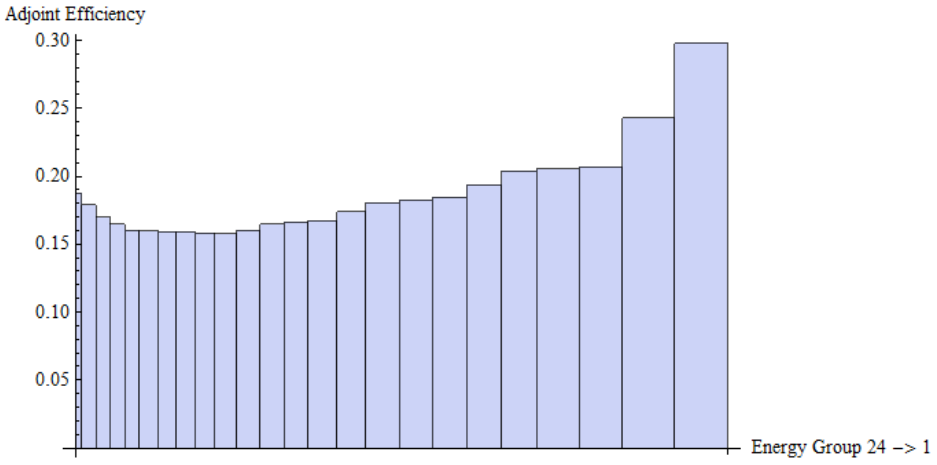

Figure 2.5: Adjoint efficiency of 4×4×8 in^3 CsI detector with increasing energy and decreasing group number. (Group energy bins can be found in Table 3.2.)

Neutron background data can be assumed to be based on data previously derived from NNSA work [9], according to SAND2008-4478 [10], neutron background radiation varies world-wide in magnitude by altitude, but the spectrum is fairly constant. Neutron background measurements are highly dependent on the respective hemisphere and specific latitudes where the background was collected, etc. In any case, Ziegler's data [11] provided a reasonable spectrum of neutrons, and the sea level total neutron flux (denoted as "Ziegler") in Figure 2.6 was determined to be an integral mean of 0.02

$\frac{neutrons}{cm^2\ s}$. From data in the SAND2008-4478 report, the Ziegler spectrum can be used as a reasonable estimate of 0.02 $\frac{neutrons}{cm^2\ s}$ at sea level, and with a multiplier of up to ~10 (or 0.2 $\frac{neutrons}{cm^2\ s}$) for regions near Los Alamos, NM. Therefore, our background assessments need to incorporate this in our detector time gating accumulations for source identification.

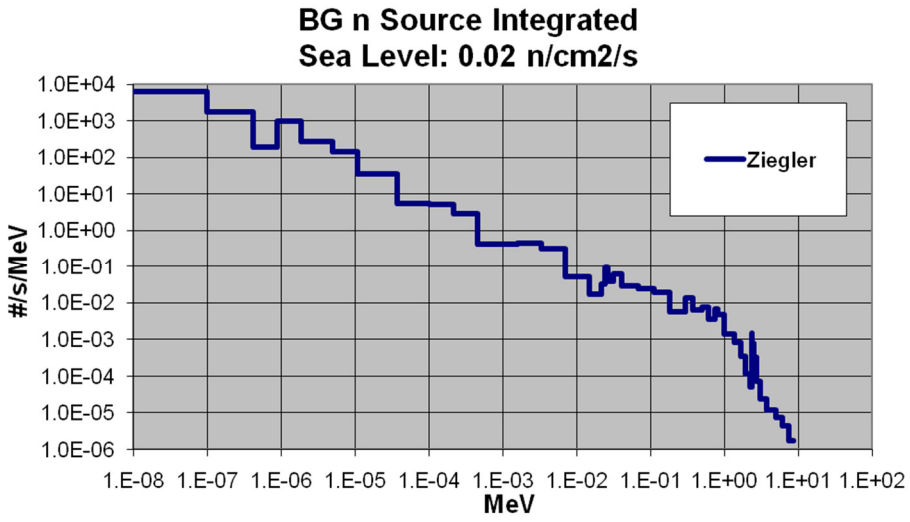

Figure 2.6: Ziegler's published neutron background radiation from [11] normalized to 0.02 $\frac{neutrons}{cm^2\ s}$.

While this data can be used to determine overall neutron background radiation, it is likely that the terrestrial neutron background radiation will be extremely small in the weapon pit storage facility in the presence of significant quantities of surrounding stored Pu masses yielding a relative "bath" of thermal neutrons driven by surrounding leakage multiplication sources. Therefore, consideration of isolating the neutron detectors with 1mm Cadmium layers was considered, since most of the distal scattered neutron background will likely be due to thermal neutrons. Neutrons were neglected for HEU sources since the rates of production were far too small to be detected; sources of ~50 $\frac{neutrons}{cm^2\ sr}$ emitted isotropically over a 4π shell or volume surface leads to fractions of a

neutron at the detector face roughly 30-50 cm away. Further information on neutron contribution to the age-since-separation technique for HEU and WGPu and the T-SADS neutron block can be respectively found in both Jessica Paul's Master's Thesis [12] as well as Matthew Molinar's Master's Thesis [13].

2.4. Deterministic Computational Models and Methods

PENTRAN is a 3-D Cartesian S_N discrete ordinates transport solver with Angle-Group-Space parallel decomposition built around the MPI architecture with high scalability to multiple processors. Deterministic methods allow global flux solutions to be measured across the entire problem space and across all energy groups; care must be taken to ensure quadrature selection is adequate; otherwise unphysical spatial discretization errors such as ray effect may occur in certain localized fine meshes. Previous studies by Al Basheer show that a quadrature selection of at least S_{32} is required for many shielding applications [14].

PENTRAN is capable of solving the linear Boltzmann transport equation by discretizing energy, angle, and space variables across a parallel computing environment by mapping each one as a virtual phase space. The multigroup transport formulation presented by Lewis and Miller (1993) is represented as Eq. 2.26. On the left hand side of the equation from left to right: losses due to free streaming of particles across a given fine mesh, losses due to collision within a given fine mesh. On the right hand side of the equation, from left to right: gains and losses from group-to-group scattering, gains and losses due to fission, and gains from independent source terms.

$$\widehat{\Omega}\cdot\nabla\psi_g\left(\vec{r},\widehat{\Omega}\right)+\sigma_g\left(\vec{r},\widehat{\Omega}\right)\psi_g\left(\vec{r},\widehat{\Omega}\right)$$

$$=\sum_{g'=1}^{g}\int_{4\pi}d\Omega'\sigma_{s,g'\longrightarrow g}\left(\vec{r},\widehat{\Omega}'\cdot\widehat{\Omega}\right)\psi_g\left(\vec{r},\widehat{\Omega}'\right) \qquad \text{Eq. 2.26}$$

$$+\frac{\chi_g}{k_o}\sum_{g'=1}^{g}\int_{4\pi}d\Omega'\nu\sigma_{f,g'}\left(\vec{r}\right)\psi_{g'}\left(\vec{r},\widehat{\Omega}\right)+q_{ind,g}\left(\vec{r},\widehat{\Omega}\right)$$

Where $\widehat{\Omega}$ is the incoming direction of the particle, $\nabla\psi_g$ is the angular flux gradient of group g, σ_g is the total cross section in group g, ψ_g is the angular flux at group g, $\widehat{\Omega}'$ is the outgoing direction of the particle, $\vec{r}$ is the reference spatial coordinate axis, χ_g is the fission neutron distribution, k_o is the criticality eigenvalue (not considered in fixed source problems), $\nu\sigma_{f,g'}$ is the fission source term (also not considered in fixed source problems), and $q_{ind,g}$ is the group-dependent independent external source term.

The angular variable is normalized such that integrating over all possible angles yields unity. In the code, angular dependencies are discretized using a series of expanded spherical harmonics (not shown here, for reference see Lewis & Miller [15]) to yield the Legendre expanded multigroup form of the 3-D Cartesian Linear Boltzmann Transport Equation, including fission sources and fixed sources (although only one or the other would be chosen in an iterative solution), shown as Eq. 2.27.

$$\left(\mu\frac{\partial}{\partial x}+\eta\frac{\partial}{\partial y}+\xi\frac{\partial}{\partial z}\right)\psi_g(x,y,z,\mu,\varphi)+\sigma_g(x,y,z)\psi_g(x,y,z,\mu,\varphi)$$

$$=\sum_{g'=1}^{G}\sum_{l=0}^{L}(2l+1)\sigma_{s,g'\longrightarrow g,l}(x,y,z)\ \Bigg\{P_l(\mu)\phi_{g',l}(x,y,z)$$

$$+2\sum_{k=1}^{l}\frac{(l-k)!}{(l+k)!}P_l^k(\mu)\left[\phi^k_{Cg',l}(x,y,z)\cos(k\varphi)\right. \qquad \text{Eq. 2.27}$$

$$\left.+\phi^k_{Sg',l}(x,y,z)\sin(k\varphi)\right]\Bigg\}$$

$$+\frac{\chi_g}{k_o}\sum_{g'}^{G}\nu\sigma_{f,g'}(x,y,z)\phi_{g',0}(x,y,z)+\sum_{g'=1}^{G}q_{ind,g}(\mu)$$

Where μ, η, and ξ are x, y, and z directional cosines for a given angular coordinate; ψ_g is the group g angular particle flux bounded from group 1 to group G; σ_g is the total group macroscopic cross section, l is the Legendre expansion index; $\sigma_{s,g'\longrightarrow g,l}$ is the l[th] Legendre moment of the macroscopic differential scattering cross section from group $g' \longrightarrow g$; $P_l(\mu)$ is the l[th] Legendre polynomial; $P_l^k(\mu)$ is the l[th] and k[th] Associated Legendre polynomial; $\phi_{g',l}$ is the l[th] Legendre scalar flux moment for group g; $\phi^k_{Cg',l}$ is the l[th] and k[th] cosine Associated Legendre scalar flux moment for group g, $\phi^k_{Sg',l}$ is the l[th] and k[th] sine Associated Legendre scalar flux moment for group g; χ_g is the average number of fission neutrons associated with energy group g per unit energy bin; k_o is the criticality eigenvalue for fission neutrons; φ is the azimuthal angle; and $\nu\sigma_{f,g'}$ is the average number of neutrons produced per fission multiplied by the macroscopic fission cross section. Since the problems solved for the MPVS are all fixed source problems,

$\nu\sigma_{f,g'}$ is set to 0 and the primary source is coming from $q_{ind,g}$ which is nominally isotropic unless a specific space-angle distribution is specified.

The quadrature sets used can range from level-symmetric quadrature sets to even-odd, Legendre-Chebyshev P_N-T_N [16], and icosahedral quadratures. For the purposes of this study, only Legendre-Chebyshev quadratures were used as our S_N order was consistently greater than 20 to avoid negative quadrature weights although other quadrature sets suitable for reflective boundary conditions could also be used for this research.

There are several differencing schemes used in PENTRAN to solve the partial differential equations shown in Eq. 2.27: Diamond Differencing (DD) [15], Diamond-Zero (DZ), Directional Theta-Weighted (DTW) [17], the predictor-corrector Exponential Directional-Weighted (EDW) scheme [18], and the predictor-corrector Exponential Directional-Iterative (EDI) [19]. PENTRAN is able to adaptively and automatically select the differencing scheme that will result in a converged solution [20]. Unless otherwise specified, all of the work presented in this study used the adaptive differencing strategy for evaluation of fluxes in all of the fine meshes. Since most of the MPVS models use air as a medium, the EDI scheme was predominant in most of the simulations. When available, preconditioned fluxes generated from the REPRO preconditioning tool were used to accelerate solutions for problems that share the same coarse mesh and fine mesh structure.

2.5. Stochastic Computational Models and Methods

The Monte Carlo code MCNP5 [21] developed by Los Alamos National Laboratory was used to validate transport data used in this work. Monte Carlo codes

work by simulating particles (histories) and track them as they are born, stream or scatter, and die by either leakage out of the system or absorption within a material. Like any Monte Carlo method, using a sufficient amount of histories is required in order to maintain reasonable statistics. Unless otherwise mentioned, all of the MCNP models used were analog simulations without use of variance reduction. Tallies are used to output data from the code for further interpretation and analysis. Examples of tally data used in the MPVS analysis include photon current across the outer source box in both the full source/detector models as well as the source canister models. Tallying the uncollided flux contribution in front of the CsI detector, as well as volumetric and pulse height tallies inside the detector volume were used in the later detector models.

As part of the MPVS project, the MCNP models of the SNM canister were performed by Jessica Paul [12] and photons and neutrons were tracked in the inner and outer source box. Photonuclear (γ, n) contribution is tracked in MCNP via the totnu card. Further information can be found in Jessica Paul's Master's Thesis [12].

Since coupled photon-neutron photonuclear data does not currently exist in any of the established multigroup libraries; we utilized the 24 group photon current from the outer source box MCNP data (with photonuclear contribution included) as input for both the volumetric and surface adjoint sources in the various detector configurations (such as the 1 inch diameter CsI and the $2 \times 4 \times 8$ in^3 and $4 \times 4 \times 8$ in^3 CsI geometries). This provides a hybridized approach in that PENTRAN runs implicitly use photonuclear data from MCNP data from the outer source box (although it doesn't track further secondary interactions). Since photonuclear interactions become more significant for higher

energies, it plays a more important role in detection of plutonium compared to HEU as the neutron signature is typically orders of magnitude higher for WGPu than HEU.

2.6. Implications of Deterministic Transport on Detector Properties

While the advantages of deterministic transport are numerous, it is important to note that a few things are not considered in any of the analyses shown below. The adjoint equation provides the detector efficiency but this is a theoretical maximum; effects due to dead time (defined as the cumulative sum of the scintillation time plus the electron multiplication time and the signal amplification time), signal losses in the photomultiplier tube (PMT) (as combinations of parameters such as relative light output and dynode efficiency), signal losses in associated electronics, inefficiencies present in preamplifiers, and thermionic emission of electrons (also known as the dark current) are not considered.

The scintillation detectors selected (1 inch diameter, $2 \times 4 \times 8$ in^3, $4 \times 4 \times 8$ in^3) for the MPVS conform to form factors commonly used in the nuclear industry. The cylindrical and parallelepiped form factors of the detector have non-reentrant boundaries, simplifying the leakage profile. The inorganic scintillator Cesium Iodide (CsI(Na)) was primarily chosen as it has higher density and atomic number compared to Sodium Iodide (NaI(Tl)) and has a fairly high light conversion efficiency in the inorganic scintillation family of detectors [22]. CsI detectors also have reduced background radiation compared to NaI detectors due to the lack of the potassium isotope ${}^{40}_{19}K$, although this comes at a cost since the absolute detection efficiency is lower in CsI compared to NaI. Although CsI(Na) has nominally around 85% of the light output at the PMT compared to CsI(Tl) it is more sensitive across a larger spectrum of wavelengths compared to CsI(Tl) [22],

which is an important consideration since photons are emitted from SNM sources over a very broad range of wavelengths. Certain material properties make CsI(Na) an attractive material as well: it is slightly hygroscopic and shares properties with other plastic materials such as shock, temperature, and vibration resistance compared to the brittle sealed environment of NaI(Tl). The ability to operate at room temperatures and their relatively inexpensive cost and maintenance is also a desirable quality.

As photons are fundamentally electromagnetic in nature they behave as both particles and waves; at higher energies suitable to the ionization of atoms the behavior is more reminiscent of particles. Photons with energies lower than 1.022 MeV interact through either the photoelectric effect or Compton scattering. Since photoelectrons typically have a very low energy it is safe to assume they are deposited in the detector (unless they are at the detector edge where leakage is more probable). The electronic transition from one atomic state to another is typically followed by the emission of a low energy X-ray or an Auger electron; these secondary reactions are typically not tracked in PENTRAN but can be tracked in MCNP assuming sufficient histories are run and secondary reactions are appropriately tracked with the physics card.

One important consideration resulting from Compton scattered photons is the spectral shift as photons downscatter to lower energies beneath the Compton Edge. This is represented as a functional dependence of detector properties (wavelength sensitivity), source spectrum, and detector size. The analyses presented in this thesis partially account for these effects excluding the aforementioned secondary particle interactions which are more important at lower energies. Since the main concern was the peak at the 1.001

MeV line, our analysis generally neglected spectral lines below 300 keV as they are not expected to leak from the detector.

One potential disadvantage with inorganic scintillators is the limited Full-Width Half Maximum (FWHM) compared to Dewar-enclosed, liquid Nitrogen cooled, High Purity Germanium (HPGe) detectors. However, recent research by Sjoden et al. [8] using the passive ASEDRA detection system shows high accuracy and precision in determining the presence of SNM using common CsI detectors. As the detectors are shared between the ASEDRA and the MPVS systems, it should be trivial to hybridize both the Age-Since-Separation technique pioneered by Maniscalco, Chapwick, and Sjoden [23] and Jessica Paul [12] with the ASEDRA system to further ensure correct identification and validation of SNM of various masses and sizes. If future funding is provided for laboratory testing of the MPVS platform, this option should be considered.

Chapter 3: Source and Cross Section Characterization

3.1. Objective and SNM Canister Background

In order to accurately determine the presence of HEU or WGPu it is necessary to characterize the spectral energy distribution of the sources both as a function of age and geometry. Applicable broad energy group boundaries that highlight key gamma lines were found by Sjoden et al. [9] for use in the T-SADS project, and a modified 24 group structure was performed.

SNM is typically stored in cylindrical steel containers stored on shelves in controlled environments. An open source literature review example is SNM storage at the Hanford site [24], shown in Figure 3.1. The SNM quantities were defined by the International Atomic Energy Agency [25] in 1 SQ units for HEU (25 kg) and WGPu (8 kg) in order to distinguish between SNM and naturally occurring radioactive materials (NORM).

Figure 3.1: SNM canister storage on racks at the Hanford Site [24]. Note that the dimensions of these canisters are smaller than those used in our analysis.

The inter-source spacing of 1 meter was determined via a trigonometric analysis of one of the images found in open source literature. Since the canister height is known it is

possible to determine trigonometrically the relative positions of the sources in the canister by converting image pixels to distances in centimeters. This distance is better visualized in Figure 1.1.

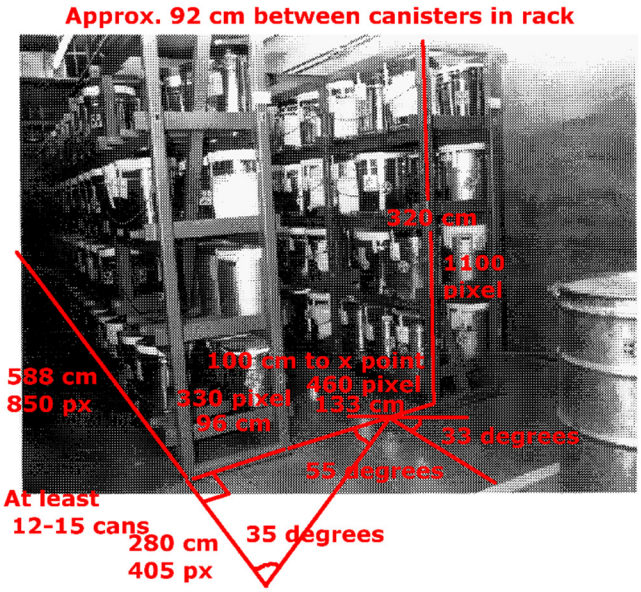

Figure 3.2: Trigonometric analysis of SNM canister storage to determine rough dimensions of canister placement. Original image from Higginson (1996). [24]

Weapons-grade material in SNM packages are typically stored in AL-R8 and AT-400A canisters; an example of the AL-R8 is shown in Figure 3.3. The AL-R8 canister is composed of a steel confinement canister, fiberboard, refractory insulation, and a pit support frame [26]. The fiberboard is specified as a polyethylene-like material called Celotex [5, 26-28], which is composed of equal parts carbon, oxygen, and hydrogen with an average density of 0.24 $\frac{g}{cm^3}$ [26].

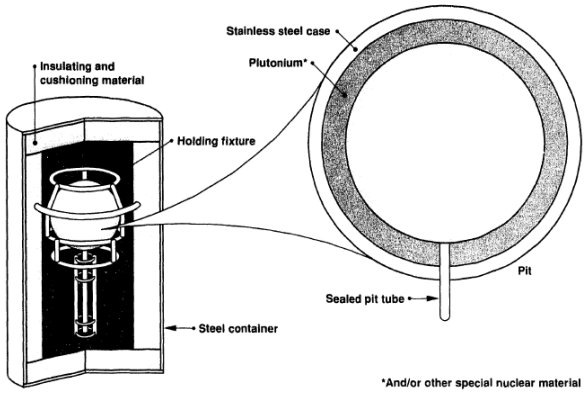

Figure 3.3: AL-R8 pit container used for a dismantled nuclear weapon at Pantex [29].

The AT-400A pit containers differ from the AL-R8 containers in that they have an additional inner confinement liner; polyurethane foam fills the space between the liner and outside container, and is also placed at the bottom and top of the container. The pit is held in place in the center of the liner by an aluminum support frame [26]. Figure 3.4 depicts this pit structure.

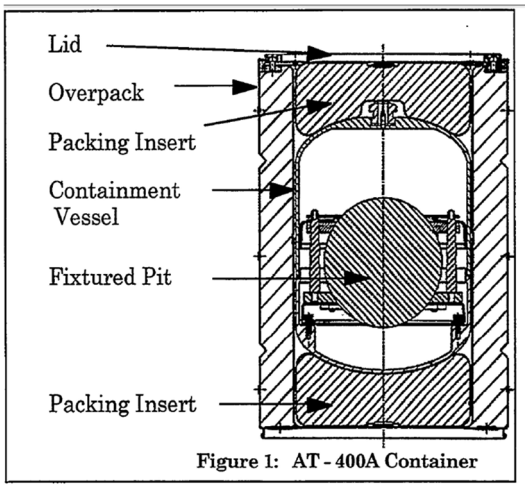

Figure 3.4: YZ cross section of AT-400A pit container for Pantex [1].

The overall dimensions and structure of both the AL-R8 and AT-400A containers were very similar; therefore we generalized both designs into a simplified, “hybrid

geometry" model and viewed this as sufficient to create standardized leakage source terms for HEU and WGPu SNM materials that could be stored in the canister. Table 3.1 depicts the dimensions for the AL-R8, the AT-400A, and our finalized "hybrid" geometry model for the MPVS source terms. For simplicity, the AL-R8 container was the principal basis for our "hybrid" geometry model.

Table 3.1: SNM canister configurations [1, 2, 24, 26, 29].

	Hybrid Model	**AL-R8**	**AT-400A**
Inner container radius/diameter (cm)	None	None	17.15/34.3
Outer container radius/diameter (cm)	26.924	23/46	25.1/50.2
Outer container height (cm)	76.2	76.0[1]	68.45
Outer container wall thickness (cm)	0.122	0.122	0.122
Packing material (thickness- cm) [composed of Celotex at 0.24g/cc or Polyurethane at 0.482g/cc]	7.0 side 5.0 top/bot	7.0 side 5.0 top/bot	6.98 side (14.07 edge 6.65 center) top/bot
Refractory fiber insulation (cm) [equivalent density at 0.128g/cc]	none	30.5x30.5x1.27 Below lid	none

3.2. Source Definition Generation via ORIGEN-ARP

The source terms for SQ masses, 25 kg of HEU and 8 kg of WGPu, were generated using ORIGEN/ORIGEN-ARP [3] modules that are isotopic depletion and decay analysis tools that are part of the Oak Ridge National Laboratory SCALE6 code system [30]. Our group found significant discrepancies between ORIGEN-ARP SCALE6 data compared to ORIGEN-ARP SCALE6.1 data, with source magnitude differences upwards of 10^7

[1] AL-R8 can also be manufactured in heights of 102.0, 127.0, and 152.0 cm depending on load size.

between these two code versions with the same input file; therefore the SCALE6 data was used for all of the analyses. The ORIGEN-ARP code system within SCALE6 produces a detailed output file accounting for all decay daughter products and their radiation contributions based on mass yield without consideration of transport effects. It also provides the unique gamma and neutron spectra as a function of age since separation per energy group for the material in question. Neutron contributions were based on the BUGLE-96 47 group structure, and gamma contributions were based on a customized 24 group structure which is shown in Table 3.2 [8, 31]. Data files used in this analysis conformed to the convention where adjoint energy bin structure used the suffix .adj and forward energy structure used the suffix .fwd.

Table 3.2: Forward and Adjoint 24 group structure for Gamma emissions.

Forward			Adjoint		
Group	**Upper Energy (MeV)**	**Lower Energy (MeV)**	**Group**	**Upper Energy (MeV)**	**Lower Energy (MeV)**
1	2.750	2.749	24	0.300	0.000
2	2.749	2.250	23	0.741	0.300
3	2.250	2.210	22	0.743	0.741
4	2.210	1.832	21	0.765	0.743
5	1.832	1.830	20	0.767	0.765
6	1.830	1.760	19	0.954	0.767
7	1.760	1.740	18	0.956	0.954
8	1.740	1.736	17	0.999	0.956
9	1.736	1.520	16	1.002	0.999
10	1.520	1.500	15	1.180	1.002
11	1.500	1.260	14	1.200	1.180
12	1.260	1.240	13	1.240	1.200
13	1.240	1.200	12	1.260	1.240
14	1.200	1.180	11	1.500	1.260
15	1.180	1.002	10	1.520	1.500
16	1.002	0.999	9	1.736	1.520
17	0.999	0.956	8	1.740	1.736
18	0.956	0.954	7	1.760	1.740
19	0.954	0.767	6	1.830	1.760
20	0.767	0.765	5	1.832	1.830
21	0.765	0.743	4	2.210	1.832
22	0.743	0.741	3	2.250	2.210
23	0.741	0.300	2	2.749	2.250
24	0.300	0.000	1	2.750	2.749

We note that this 24 group structure was used in previous research [8, 31] and selected because it isolates the key uranium and plutonium gamma emissions

(photopeaks), such as the 1001 keV line for $^{238}_{92}U$ in equilibrium with $^{234m}_{91}Pa$, and similar gamma emissions in a minimal gamma library applicable to this problem [8, 32]. The resulting neutron and gamma probability distributions were utilized in the MCNP Monte Carlo and PENTRAN 3-D S_N models to be discussed in the following sections.

Both 1 year old and 50 year old HEU (age since separation) were considered to show how the HEU signature changes with age due to the in-growth of decay daughters, specifically the $^{214}_{83}Bi$ isotope, and how this can affect the detectability of stored HEU. The average age of plutonium in the US stockpile ranges from 20 to 26 years, so 22.5year old plutonium was used [33].

3.3. Cross Section Generation

The macroscopic multigroup photon cross sections used for PENTRAN were generated using the code CEPXS from Sandia National Laboratories in the 24 photon energy groups of interest [34]. A table of the 24 energy group distribution is shown in Table 3.2. Since upscattering is not possible for photons, only downscatter cross sections were considered for the scattering kernel. The isotopic data for the HEU and the WGPu are shown in Table 3.3 and Table 3.4.

Table 3.3: Isotopic Makeup of HEU used in this study.

Isotope	Concentration (wtpt%)
U-235	90.0
U-236	0.664
U-238	8.5027
U-234	0.8334

Table 3.4: Isotopic Makeup of WGPu. Natural indicates natural composition of isotope which can be found in the SCALE6 Standard Composition Library.

Isotope	Concentration (wtpt%)	Isotope	Concentration (wtpt%)
Pu-238	0.02	C-Natural	0.023
Pu-239	93.279	Zr-Natural	0.01
Pu-240	5.911	Na-Natural	0.005
Pu-242	0.2	Fe-Natural	0.001
Pu-241	0.028	Mo-Natural	0.0009
Am-241	0.256	Al-Natural	0.0005
Ga-Natural	0.0335	U-238	0.2321

Legendre P_2 cross section moments were generated for all of the materials; this was done to computationally speed up calculations since the streaming terms of the transport equation were expected to be mostly isotropic. Furthermore, since P_2 moments preserve particle currents, this is acceptable as photon tallies coming out of the outer source box are desired. Available cross sections for materials include air, tungsten, lead, Celotex, stainless steel, cesium iodide, and NRC regulatory concrete. In all of the models, lead and concrete were not used but cross section data exist for future models (such as simulation of ground-scatter from the floor).

The compositions for most of the materials were gathered from the SCALE6 Standard Composition library [35]. Specifically, the air material was the ANSI standard Dry Air, and the steel was SS-316. This particular grade of steel is common in the nuclear industry due to its high strength and corrosion resistance [36]. Since the steel thickness is smaller than the fine mesh structure in the deterministic model, the steel and air densities were adjusted to preserve mass; this can be done by increasing the steel

thickness and decreasing the steel density in locations where mesh thickness was limited to a minimum size. This process can effectively be used to increase computational efficiency as fewer meshes are required in the model; the individual fine group fluxes are not significant enough in the steel region to warrant a high resolution meshing scheme. For example, the SS-316 steel density was decreased from the standard composition value of 8.16 g/cm^3 to 1.95 g/cm^3 using the proportionality equation:

$$\Delta\rho_1\Delta x_1 = \Delta\rho_2\Delta x_2 \qquad \text{Eq. 3.1}$$

Where ρ is density, and Δx is the thickness of the material in question; in this example, Δx_2 was increased to 0.5 cm to properly represent the mass for a very thin layer of stainless steel in the PENTRAN Cartesian mesh grid. Since the mass was preserved and the thickness itself was not increased by a large amount, the impact on the angular flux due to the increase in stainless steel thickness was small.

3.4. Source Box Surfaces and MCNP Models

Two "source boxes" were used as tallying regions of interest. The "inner" source box is a cube of dimensions equal to the outermost radius of the source ball. The "outer" source box encompasses the entire outer boundaries of the model. See Table 3.5 for specific dimensions of the inner and outer source boxes. Both boxes were defined to be used as a standardized metric for comparisons between continuous energy MCNP5 and multigroup PENTRAN. Intrinsic photons resulting from the decay of parent nuclides were added with photons from spontaneous and induced fission to form a total photon leakage term. The outward streaming photon leakage of the outer source box for a single surface was also used as a source term in our MPVS deterministic models.

For most of the PENTRAN runs, a volumetric source was used where the HEU/WGPu shell or solid resides. This was performed on a fine-mesh basis, and was automatically generated with the PENTRAN geometry meshing tool PENMSH-XP [37]. Since there are spectral boundary conditions along the edges of the problem, the volumetric sources were defined to be spatially isotropic. Since PENMSH-XP is a Cartesian fine mesh geometry creator, special attention was made to ensure that the source material mass fraction was within a percent or two of the actual theoretical mass.

Table 3.5: SNM pit dimensions for 1 SQ HEU and WGPu sources.

	HEU	**WGPu**
Solid Radius (cm)	6.7918	4.581
Solid Inner Source Box length(cm) × width(cm) × height(cm)	15.58 × 15.58 × 15.58	11.17 × 11.17 × 11.17
Solid Outer Source Box length(cm) × width(cm) × height(cm)	60 × 60 × 77.2	60 × 60 × 77.2
Shell Inner radius (cm) Outer radius (cm)	 12.458 13.087	 6.909 7.524
Shell Inner Source Box length(cm) × width(cm) × height(cm)	28.17 × 28.17 × 28.17	17.05 × 17.05 × 17.05
Shell Outer Source Box length(cm) × width(cm) × height(cm)	60 × 60 × 77.2	60 × 60 × 77.2

Each sphere was additionally surrounded by 1 cm of Aluminum cladding. In all models, the inner source box immediately surrounds this surface, and the outer source box surrounds the steel canister. Figure 3.5 and Figure 3.6 show cutaway views along the x-z and x-y planes, respectively for the HEU shell and HEU solid sphere sources.

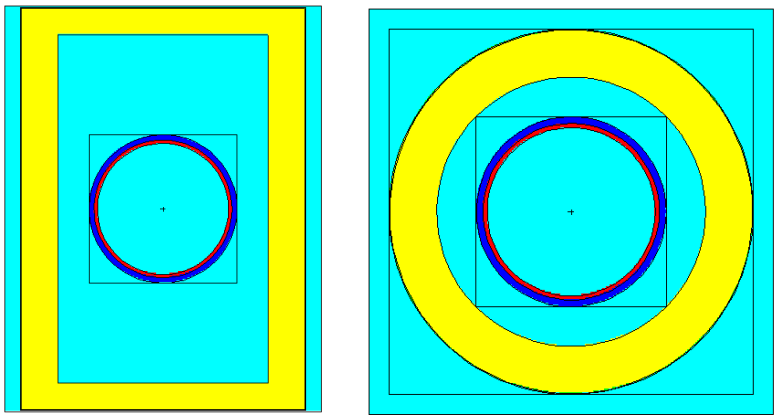

Figure 3.5: MCNP Monte Carlo geometry model of HEU shell source geometry cut along x-z and x-y planes. The inner most shell is HEU, the surrounding shell is aluminum. Air surrounds the shells and is contained by Celotex, which is surrounded by a thin layer of steel. Air makes up the remaining portion of the figure. Model originally generated as a part of Jessica Paul's Master's Thesis [12].

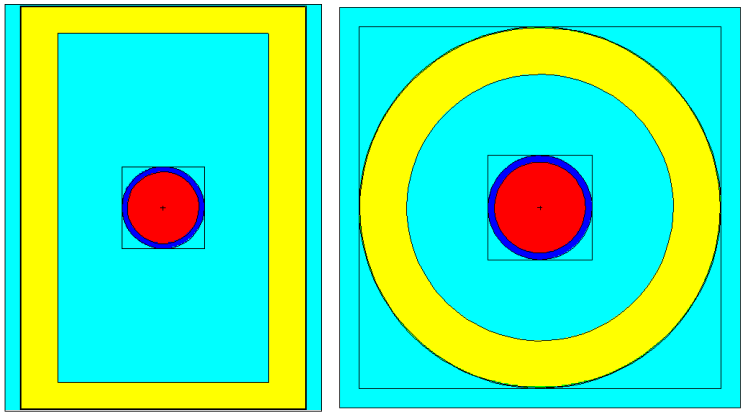

Figure 3.6: MCNP Monte Carlo model of HEU solid source geometry cut along x-z and x-y planes. The inner sphere is HEU, the surrounding shell is aluminum. Air surrounds the shells and is contained by Celotex, which is surrounded by a thin layer of steel. Air makes up the remaining portion of the figure. Model originally generated as a part of Jessica Paul's Master's Thesis [12].

Only intrinsic gammas were considered for the HEU pit, since the neutron contribution is very weak and not useful to have detectable significance. However, intrinsic gammas, neutrons, and gammas resulting from (n, γ) reactions must be considered for the WGPu pit. The source specification information and probability cards

in MCNP5 were defined from the gamma and neutron distributions per energy group derived from the ORIGEN code as discussed earlier.

The photon/neutron particle currents were recorded across each source box surface using surface current tallies with a cosine card, and the corresponding tally multiplier of source intensity as a function of time was aliased to that specified by the ORIGEN output. For the WGPu pit, each MCNP model was run twice, once for the determination of the intrinsic gammas via photon only transport mode, and again looking at the neutron, (n, γ) and fission photons via neutron transport mode with induced photons. The NONU card was included for all intrinsic gamma runs in the WGPu models so that no fission gammas were included. The TOTNU card was included for the fission induced/spontaneous gamma runs to account for all fission events. The results for both runs were combined to yield an integrated WGPu gamma signature. Monte Carlo tallies for all photon currents were binned in a manner consistent with the 24 group structure. These results were then compiled into a master SNM database for both HEU and WGPu of various ages and geometries with current leakages listed across all faces of the source boxes. Further details about the SNM Source Book can be found in the Appendix of Jessica Paul's Master's Thesis [12].

3.5. Special Nuclear Material Pit PENTRAN Models

The same procedures described in Section 3.4 are used to create 3-D model input decks in PENTRAN [19] using the PENMSH-XP [37] code with the same dimensions as Table 3.5 for both HEU and WGPu in both shell and solid ball geometries. One-eighth reflective symmetry was employed on -x, -y, and -z boundaries in order to both increase computational efficiency and fidelity. PENMSH-XP supports attribution of mass balance

[37], so that inaccuracies due to a "voxelized" Cartesian fine mesh structure are minimal, and the mass balances for materials of interest (particularly HEU and WGPu) were represented with less than 1% different than in the actual geometry, while less important materials (such as air or stainless steel) were discretized with at most 10% different in mass. A compromise was made in the fine mesh specifications to best approximate the mass balance; increasing the number of mesh cells along the outer boundaries of the problem is possible, but adds to the computational cost; an appropriate model was used to facilitate the accuracy and convergence required.

The coarse mesh boundary (the thin white line in Figure 3.7a) was selected so that the inner source box geometry aligns with the MCNP inner source box geometry; this was also performed to simplify tallying on the inner source box region.

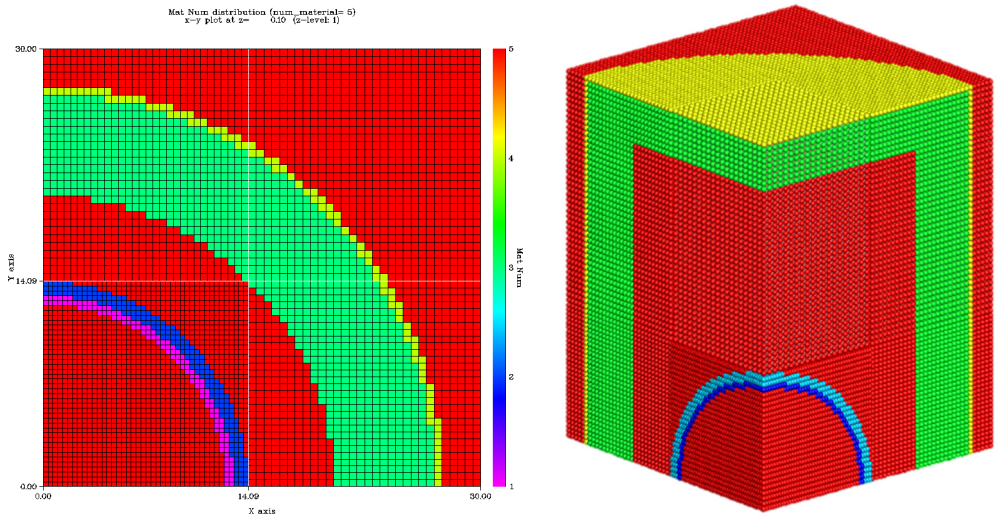

(a) (b)

Figure 3.7: PENTRAN model (a) x-y slice of HEU shell model, the innermost shell is HEU (Purple), surrounded by aluminum (Blue), ANSI Dry Air (Red) encompasses the space between the aluminum and next material, celotex (Green), Stainless Steel 316 (Yellow) surrounds the celotex, and air takes up the remaining space. Note that the "inner source box" is defined at X and Y boundaries of 14.09 cm for this particular model and was used as a metric for comparison between deterministic gamma leakages and Monte Carlo gamma leakages. (b) Isometric view of PENTRAN HEU shell model, 3-D perspective, rendered in *TecPlot 360*.

PENTRAN decomposes the Boltzmann transport equation Eq. 2.17 in angle, group, and space by tasking processors in a virtual computational phase space [19]. The 24 group problems contained ~200 million total equations using S_{26} Legendre-Chebychev P_N-T_N quadrature [16] executed on 64 processors using hybrid decomposition schemes (angle, energy, and spatial decomposition) and required 19 MFLOPS. All models were then later run using a Legendre-Chebyshev S_N quadrature value of S_{42} to mitigate ray effects present from the large amount of air in the models, and used the "group window" option in PENTRAN to sequentially run (and converge) each energy group since the cross sections used were down-scatter only [19]. A general trend observed was that spatial decomposition was more sensitive to variations in numerical convergence, particularly in the outer regions of the problem; decomposing the parallel phase space in angle and group was preferred.

Plots of the converged photon fluxes for Forward Group 16 (0.999 to 1.000 MeV) and Forward Group 24 (1.E-13 to 0.300 MeV) are presented in Figure 3.8; these indicate mild ray effects are present, however the large amount of incoherent scattering from the hydrogen elements in Celotex mitigates this effect [6].

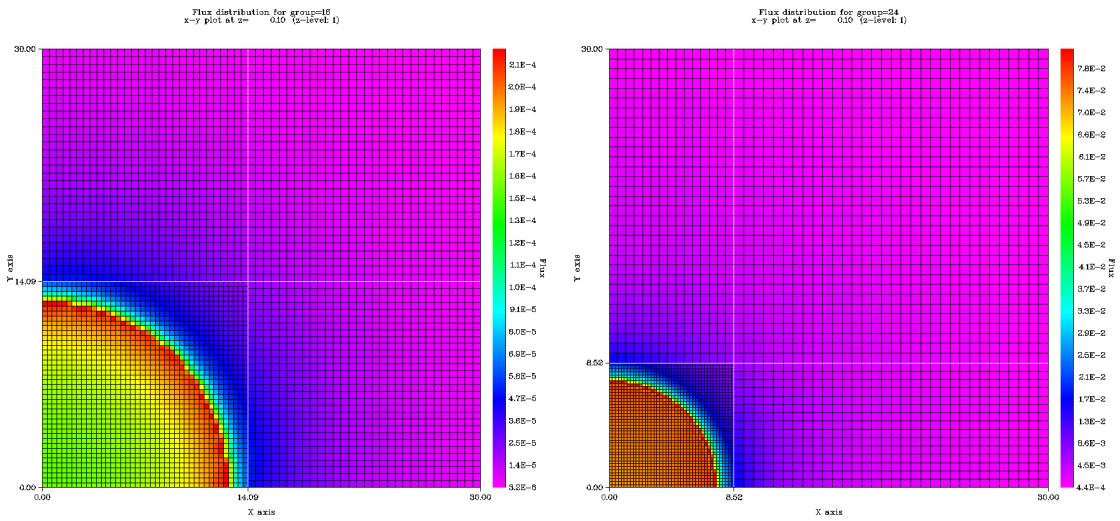

(a) (b)

Figure 3.8: PENTRAN results; (a) HEU intrinsic photon flux for Group 16 (0.999 MeV – 1.002 MeV) on an XY slice of the shell model. Group 16 was chosen since it is one of the likely candidates for detecting SNM gammas. (b) Plutonium intrinsic photon flux for Group 24 (1.0×10^{-13} MeV to 0.3 MeV) on an XY slice of the shell model.

3.6. Leakage Spectrum at Source Box Edge

The resulting leakage currents through a single surface of the inner and outer source boxes were compared for both the MCNP5 and PENTRAN models to verify agreement. Due to symmetry inherent in the models, leakage in the x-, y-, and z-axis directions are similar. For the purposes of this discussion, the percent difference is defined as:

$$Percent\ Difference = 100\left|\frac{2(J_{MCNP}-J_{PENTRAN})}{J_{MCNP}+J_{PENTRAN}}\right| \qquad \text{Eq. 3.2}$$

Where $J_{PENTRAN}$ is the photon leakage result from deterministic PENTRAN results, and J_{MCNP} is the photon leakage result from MCNP5 computations.

Convergence tolerances of the scalar flux in the PENTRAN models vary based on group, but are typically ~1.0×10^{-5}. The current leakage was determined by integrating

over the half space. The results showed the two models differed on average by less than 5% for most energy groups in the inner source box, and on average less than 10% for most energy groups of the outer source box [38]. Comparing computations using multigroup S_N gamma transport compared with continuous energy gamma transport can prove challenging to achieve overlapping agreement, particularly with rapid changes in the photon cross section over the lowest 15 energy groups. Increasing particle histories and rerunning the MCNP models until the statistical errors decrease should bring the two models into closer agreement, although current results are reasonable and consistent for analysis.

Figure 3.9 shows a normalized histogram plot of the 1 yr HEU shell outer source box photon leakage for both the MCNP5 and PENTRAN models. This same relationship between continuous energy MCNP5 and multigroup PENTRAN is continued for the solid 1 yr and both 50 yr cases. It should be noted that the histogram plots start at 0.741 MeV, although the data was computed from Monte Carlo cutoff, and the lower energies are not shown. This energy (0.741 MeV) was selected as the lower bound for the histograms, since the lower energy photons (with larger relative errors in the simulations) can easily be shielded.

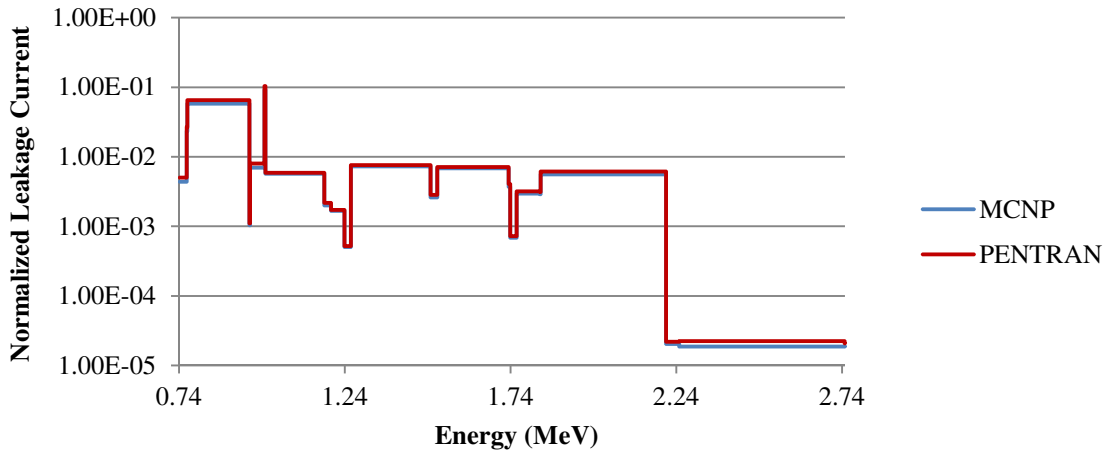

Figure 3.9: Normalized leakage source term for 1 yr HEU shell at surface of weapons pit canister. The results are from the MCNP5 and PENTRAN models. Normalization based on 6.42×10^4 Photons/s for MCNP and 4.62×10^4 Photons/s for PENTRAN.

As stated earlier, the source term for 50 yr HEU is expected to deviate from 1 yr HEU due to ingrowth of decay daughters. Figure 3.10 shows that this surely is the case. More high energy gammas are seen as more daughters appear along the decay chain such as $^{214}_{83}Bi$.

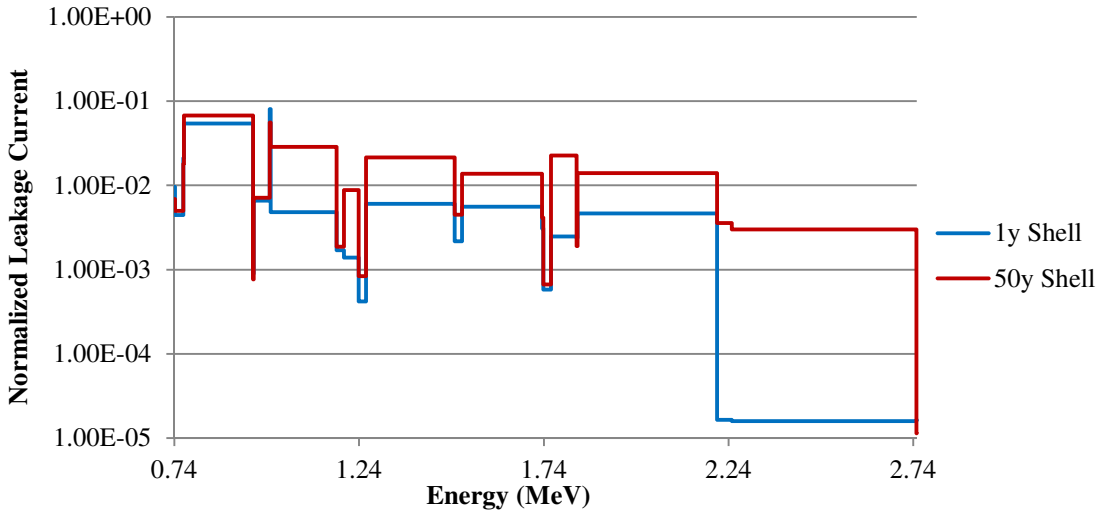

Figure 3.10: Comparison between leakage source terms for 1 yr and 50 yr old HEU. These results are from the MCNP5 models. (Based on 6.42×10^4 Photons/s for 1 y and 9.26×10^4 Photons/s for 50 y).

Comparing the solid and shell models for each type of SNM shows the impact of self-shielding on the gamma leakage through the canister. Figure 3.11 shows that the photon leakage is noticeably decreased when the weapon pit is in solid geometry form for 1 yr HEU. This trend continues in the 50yr HEU case. The yield of both models, however, is approximately equal, depicting the presence of the same aged SNM.

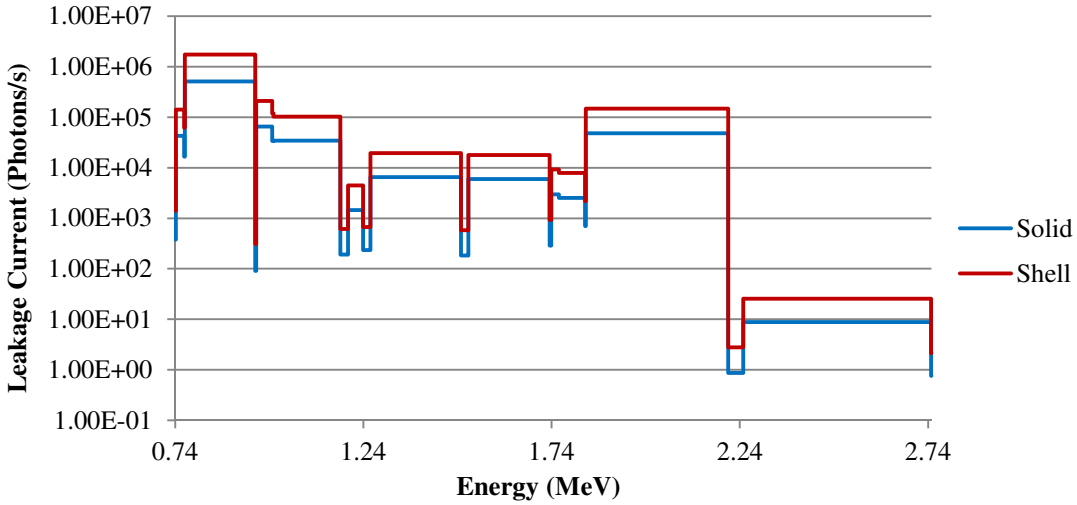

Figure 3.11: Comparison between shell and solid 1 yr HEU particle leakage. These results are from the MCNP5 model.

The continuous energy MCNP and multigroup PENTRAN intrinsic gamma leakage for WGPu were comparable at the outer source box. Figure 3.12 shows the outer source box normalized photon leakage for both models.

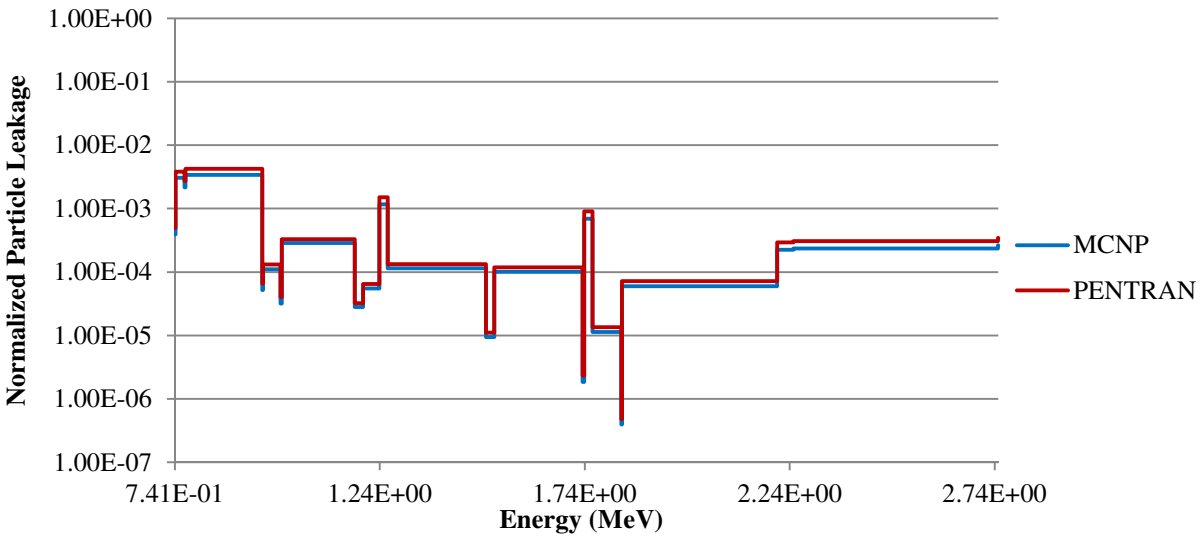

Figure 3.12: Normalized intrinsic photon leakage through +x plane of outer source box for WGPu shell in the Continuous Energy MCNP5 and multigroup PENTRAN models. Normalization is based on 1.83×10^{7} Photons/s for MCNP and 1.32×10^{7} Photons/s for PENTRAN.

Continuous energy MCNP5 was used to recover the contribution to the total photon leakage from neutron induced photons. PENTRAN was not used to find this information since at the time the necessary cross section libraries needed for coupled (n, γ) reactions was unavailable. Figure 3.13 shows the resulting normalized induced photon leakage through the +x plane of the outer source box.

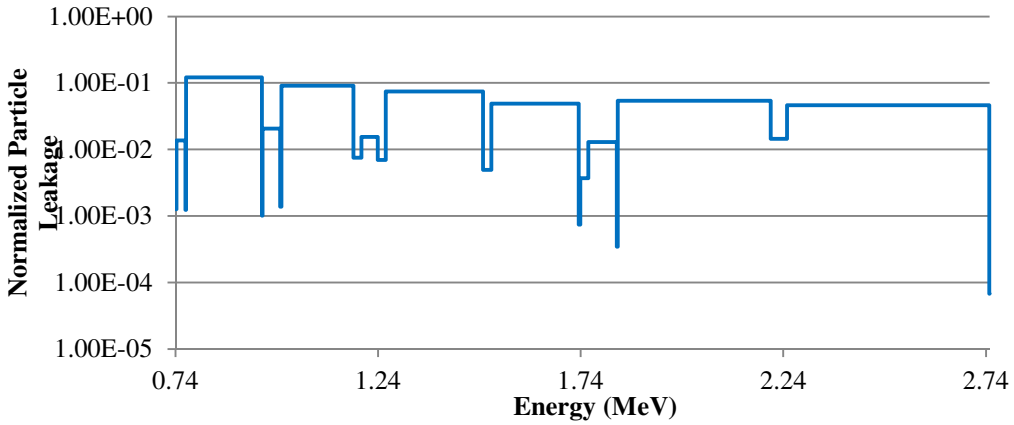

Figure 3.13: Normalized induced photon leakage through x+ plane of inner source box for WGPu shell model in MCNP5. Normalization based on 4.69×10^{4} Photons/s.

The contributions from both the intrinsic and induced photon results were combined then normalized with respect to the total photons per second over the energy groups. Figure 3.14 shows this compilation at the +x plane on the outer source box.

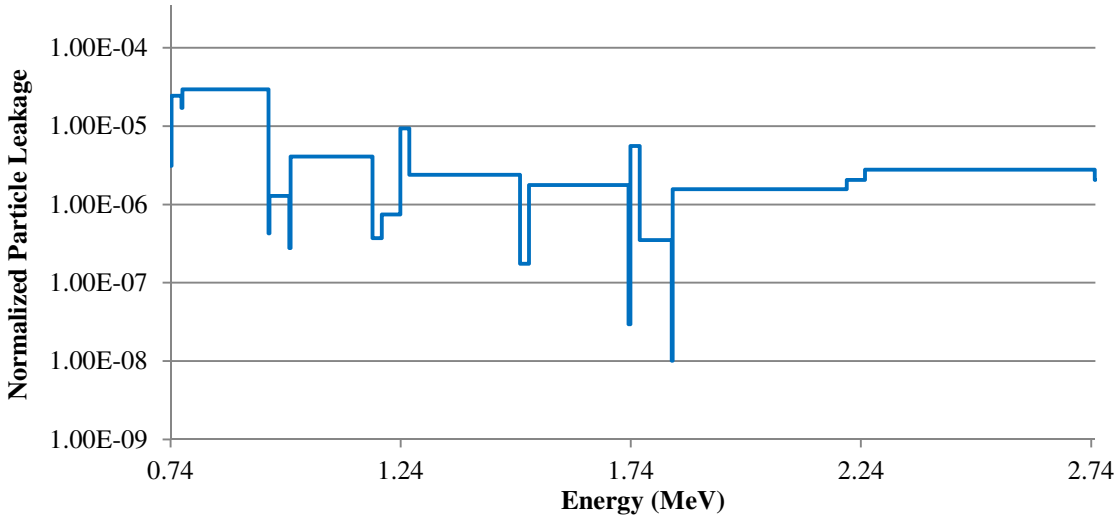

Figure 3.14: Normalized intrinsic and induced photon leakage through x+ plane of outer source box for WGPu shell model in MCNP5. Normalization based on 2.33×10^{9} Photons/s.

Neutrons were also taken into consideration for the WGPu source term. Figure 3.15 shows the normalized neutron leakage for the Bugle-96 47 group structure. Further details on the usage of the WGPu source term can be found in Jessica Paul's Master's Thesis [12]. The results from all of the figures in this section can be found in the SNM Source Book. This is an Excel spreadsheet that tabulates SNM based on age since separation, source geometry, and source material. Source magnitude along the outer edges of the source box for each plane are recorded for both MCNP5 and PENTRAN models. This is useful as users can simply model the SNM source of interest as a thin

volumetric source or a surface source with energy spectra "painted" on without performing the actual transport for the SNM source canister itself.

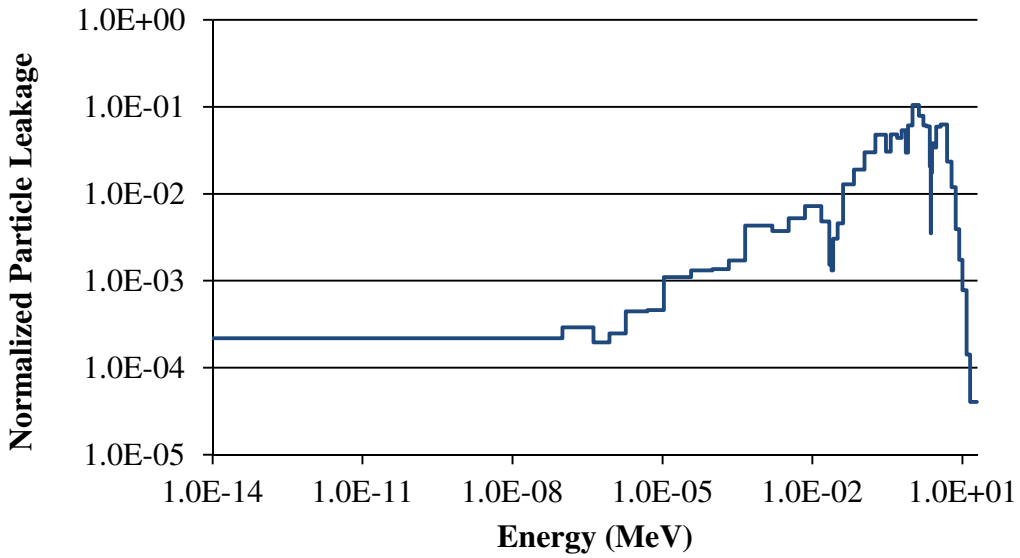

Figure 3.15: Normalized neutron leakage for WGPu shell model in MCNP5. Normalization based on 1.43×10^5 Neutrons/s.

3.7. Angle-Space Dependence of Outer Source Box

The results from the PENTRAN models were used to find the spatial distribution along the surface of the outer source box for the photon leakages of the HEU. This distribution will account for the spherical shape of the actual SNM pit in the center of the box. Each side of the source box has an x and z axis or y and z axis distribution while the top and bottom surfaces have an x and y axis distribution with the maximum number of photons leaking through the center of each plane. Figure 3.16a shows a representation of the leakage distribution across the top and bottom surfaces of the box and Figure 3.16b represents the leakage distribution for each of the four sides of the outer source box.

These distributions can be used to "paint" the leakage source term on a simplified box surface (with zero importance set inside if using Monte Carlo) to aide in creating models as depicted in Figure 3.17. These results are consistent with an isotropic source and can be considered an isotropic point source if the detector is far enough away.

Any results using the space-angle source box leakages do not use the simplistic isotropic source treatment; instead it is modeled fully (although it is normalized to a unit source strength of 1 across the YZ plane). This allows a fully consistent space-angle distribution to be used as a spatial source as seen in the $4 \times 4 \times 8$ in^3 CsI detector model with 10 cm long and 5 cm thick collimator seen in Section 4.9. An alternate viewpoint of Figure 3.16Figure 3.16a is shown in Figure 3.18 while Figure 3.16b is shown in Figure 3.19.

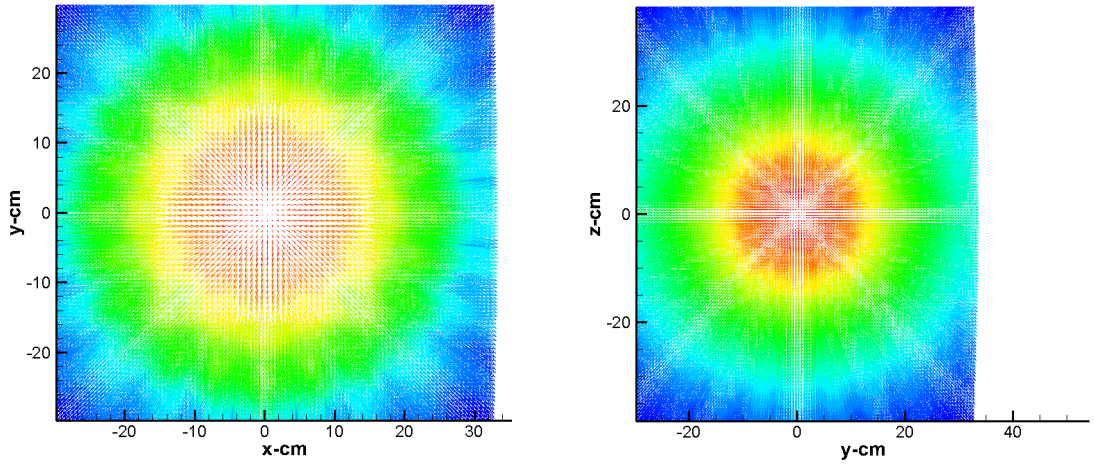

(a) (b)

Figure 3.16: (a) The relative contributions of photon leakage across the top and bottom surfaces (XY) of the Source Box for Group 14 (0.999 MeV to 1.002 MeV) photons in a 1 yr HEU shell source. (b). The relative contributions of photon leakage across the sides (YZ) of the Source Box for Group 14 (0.999 MeV to 1.002 MeV) photons in a 1 yr HEU shell source. Both models generated using njdump output from PENTRAN from S_{42} results.

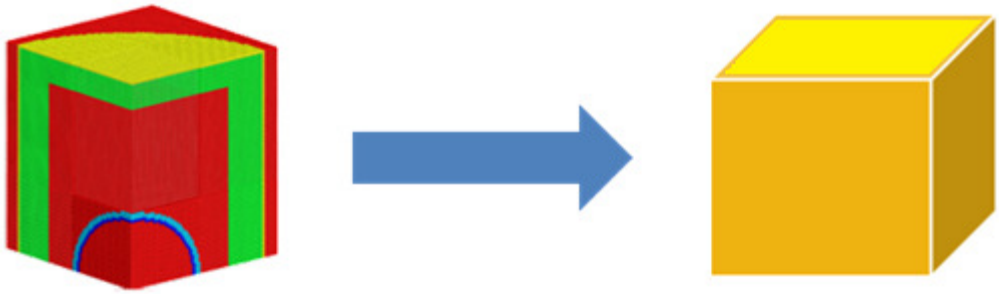

Figure 3.17: The complicated weapon pit geometry can be simplified so that the contents no longer need to be modeled and the leakage source term can be used in a "painted" distribution on the surface of a box. The bright yellow region indicates a quarter reflected symmetry source box XY plane where the leakage distribution can be applied.

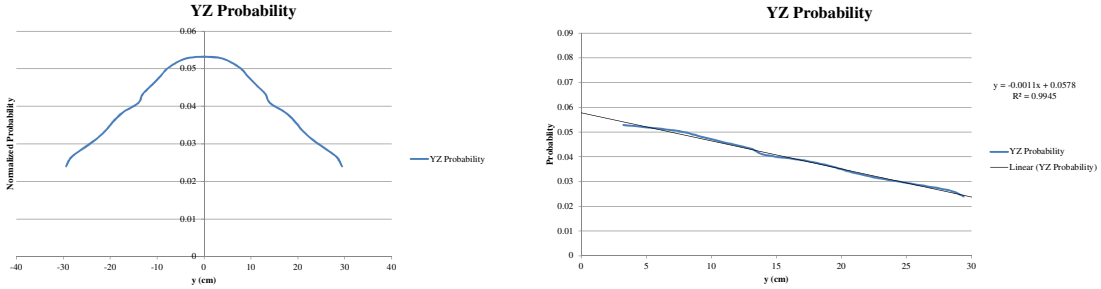

(a) (b)

Figure 3.18: Centerline (z=0) YZ Space-Angle Probability Distribution for Source Plane (a) and linear extrapolation across half of the source face (b).

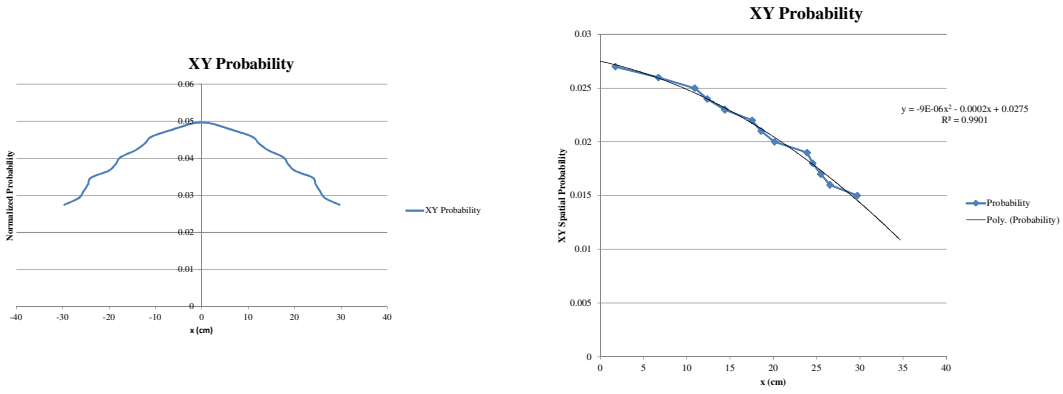

(a) (b)

Figure 3.19: Centerline (y=0) XY Space-Angle Probability Distribution for Source Plane (a) and quadratic extrapolation across half of the source face (b).

Chapter 4: Detector Optimization and Response

4.1. Objective

The purpose of this analysis was to determine the total number of counts in the detector as a function of energy and mobile platform speed for a series of passive gamma detector designs. Collimation was considered to minimize the Out-of-Field signal from adjacent sources. Open questions that were resolved from this analysis include the optimum collimation length, collimator thickness, energy-dependent adjoint and forward reaction rates (and whether these rates are larger than the minimum threshold for detection), mobile platform speed, and detector form factor. Neutron reaction rates were calculated on a neutron block basis for one simplified T-SADS neutron detector module, along with corresponding discussion on neutron adjoint importance. The main focus of this effort was to use the characterized gamma signatures from Section 3.6 and determine the effect of the In-Field sources and the OOF sources.

4.2. Gamma Collimation Methodology

When designing a passive gamma detection system it is necessary to consider and properly shield the impact of adjacent sources as well as the gamma background from the source of interest. To do this, tungsten collimation was chosen for both its availability, as well as its high density (~19 $\frac{g}{cm^3}$). A quick calculation using the Beer-Lambert attenuation law suggests that a single mean free path of 1.001 MeV directly impinging photons streaming through tungsten requires approximately 4 cm of shielding. However, one assumption we made during the start of our analysis was that the sources were

arranged in a series of two racks perpendicular to the detector assembly itself (assuming a room height of approximately 2 meters); this implies that photons will not be streaming directly towards the collimators but will instead travel obliquely through the collimator, so the actual distance traveled is x*sec(θ), where x is the thickness of the collimator.

Two transport models were developed to account for the thickness of the collimator: one "light" collimation scheme had a relatively small thickness of 1 cm, the other Mean Free Path (MFP) collimation scheme had a thickness of 5 cm. An analysis of this kind depends on multiple covariant factors: source-detector distance, source type (HEU or WGPu), source age, collimator length, and inter-source spacing. While the density of tungsten makes an excellent gamma attenuator, that same property makes it prohibitive on a mobile platform due to its tremendous weight. One question from this analysis was whether or not the 1 cm thick collimation would be adequate to shield most 'Out-of-Field' photons, or if the 1 MFP case was required.

There are several parameters that will determine an optimum collimation length. The most important one is the linear Field of View (FOV) of the detector. This value is related to the angular Field of View by multiplying the tangent of the angular Field of View with the collimator-to-source distance. That is,

$$linear\ FOV\ [cm] = \tan\theta * csd \qquad \text{Eq. 4.1}$$

Where θ is the angular FOV and csd is the collimator-to-source distance in cm.

This value must be less than the inter-source spacing; otherwise the detector will be looking at multiple sources simultaneously. For our analysis, the inter-source spacing

was assumed to be 1 meter, as the source canisters are quite large (60 cm × 60 cm × 77.2 cm). Furthermore, the In-Field and Out-of-Field areas were defined as the area directly opposite to the detector and far away from the collimator respectively (although these two areas differ depending on the model considered).

Another important factor in determining optimum collimation length is the angular Field of View of the detector. This value is calculated (in degrees) by:

$$\theta\ [^{\circ}] = \tan^{-1}\left(\frac{csd + d_{offset}}{l}\right)\left(\frac{180\ degrees}{\pi\ radians}\right) \qquad \text{Eq. 4.2}$$

Where csd is the collimator-to-source distance (cm), d_{offset} is the half-thickness of the detector (cm), and l is the collimator length (cm). An important point is that although the angular FOV can remain constant as the collimator-to-source distance is increased or decreased, the linear FOV will change as that distance is adjusted. Therefore the linear FOV is a more accurate representation of how much source is seen by the detector at any given time increment dt. For the purposes of our models, a collimator-to-source distance was analyzed in 10 cm increments from 30 cm to 50 cm. Generally (in absence of scattering effects) we would expect higher count rates as the detector is moved closer to the source since there is less $\frac{1}{4\pi r^2}$ source divergence. Although scattering is considered to P_2 truncation in the integral in the transport models, since the MPVS will be operating in a room temperature environment with standard temperatures and pressures (1 bar dry air atmosphere) we can generally assign low importance to anisotropies resulting from Compton scattering since the density of air provides a large mean free path and hence a minimal collision frequency. Since the detector platform is moving (we have assumed it

will move with a constant velocity), the time interval dt that the detector is exposed to a certain amount of radiation originating from the linear FOV along dx can be determined with:

$$dt\ [s] = \frac{linear\ FOV}{v_o} \qquad \text{Eq. 4.3}$$

Where v_o is a constant velocity (cm/s) along a linear FOV pathway as defined above in Eq. 4.1. The result from Eq. 4.3 is then multiplied by the adjoint or forward reaction rates to give a total detector count as a function of energy. The axial centerline photon adjoint reaction rates were calculated for In-Field, Out-of-Field, and Whole-Field source volumes for 1 year HEU shell and solid sources, 50 year HEU shell and solid sources, and 22.5 year WGPu shell and source models.

4.3. Initial Gamma Detector Design

The initial detector was considered to be a 2.54 cm radius, 60 cm tall cylinder of Thallium-activated CsI scintillation detector. Cesium iodide was selected since it has both a higher density (4.510 g/cc) as well as a higher atomic number than similar sized NaI detectors [22]. Our analysis neglects the impact of ancillary effects on net detector counts (light-conversion efficiency, dead time, or phosphorescence within phototube glass). We refer to detector efficiency as a function of energy of the average adjoint importance within the detector volume itself. This detector was to be operated as a pair of two cylindrical detectors working in tandem, with the total integrated signal collected via a standard Multi-Channel Analyzer in a Nuclear Instrumentation Bin (NIM-Bin). Figure 4.1 shows a diagram of the 2.54 cm radius CsI(Tl) detector configuration with both a 1 cm thick and 5 cm thick tungsten collimator.

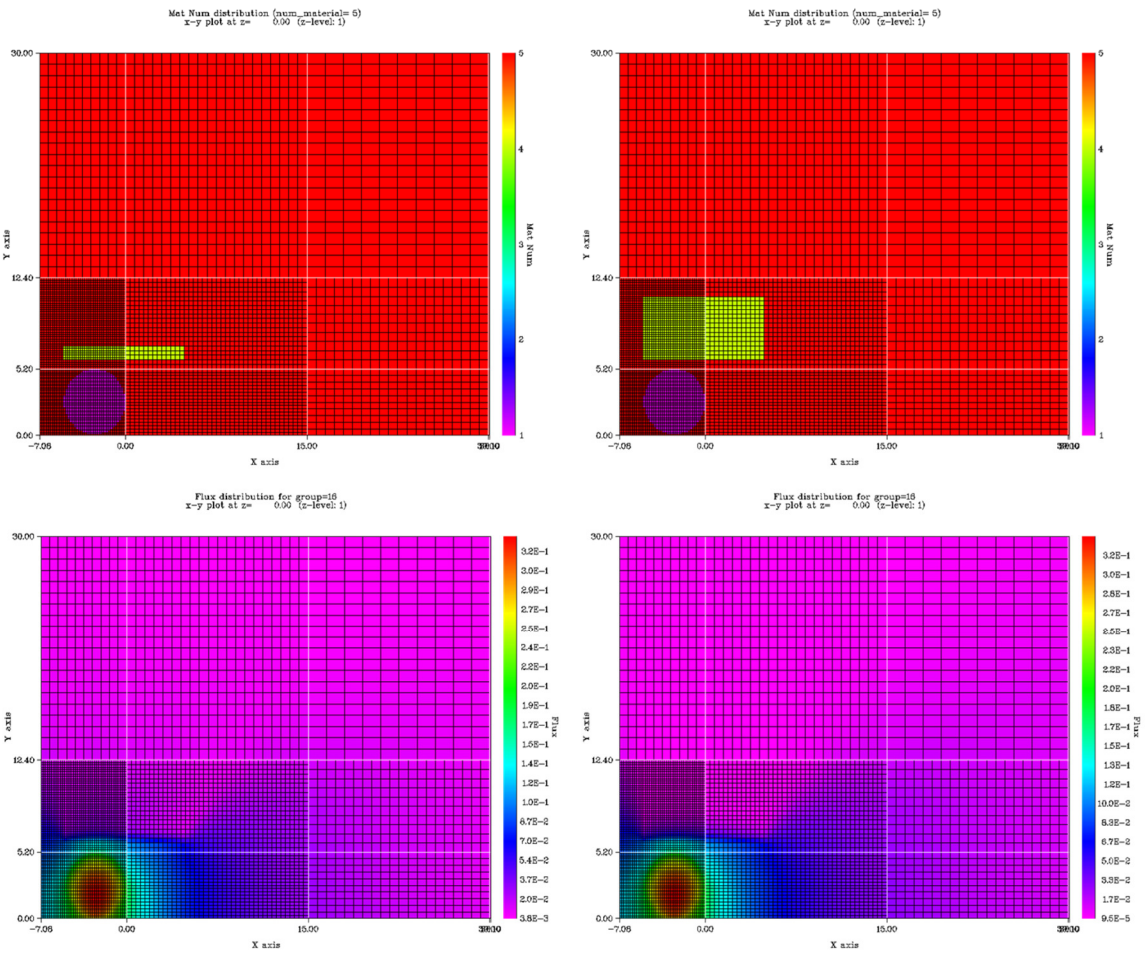

Figure 4.1: Center slices through 3-D adjoint models. (Top): 60 cm long 2.54 cm radius CsI cylindrical detector configuration with 1 cm thick and 5 cm thick, 5 cm long tungsten collimation. Note that the bottom of each image represents a specular reflective boundary condition. (Bottom): Adjoint importances as a function of fine mesh for the 1.001 MeV gamma line.

The adjoint photon importances for the 1.001 MeV gamma line for various detector collimator configurations for the 60 cm long, 2.54 cm radius CsI detector are shown in Figure 4.2 and were interpolated using the 3-D interpolation program 3DI. The effect of increased collimation length is inversely correlated with the adjoint importance along the YZ axis at the edge of the model. As discussed in this report, achieving optimal results for the design depend upon the background radiation and number of detector platforms used to time gate the signal.

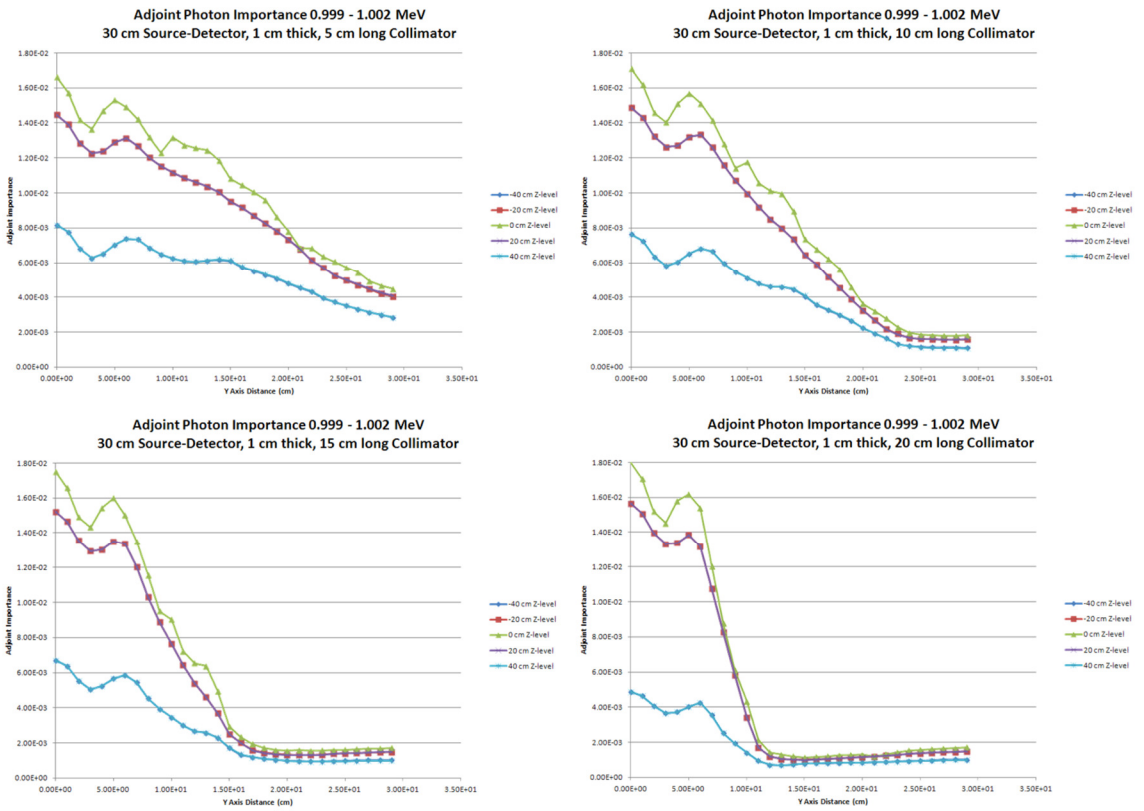

Figure 4.2: Adjoint photon importances (aliased to detector efficiency) for the 1.001 MeV gamma line for various detector collimator configurations for the 60 cm long, 2.54 cm radius CsI detector with various length tungsten collimators each 1 cm thick. From upper left to lower right: 5 cm, 10 cm, 15 cm, and 20 cm long collimator adjoint importances. The five cases shown in each figure are y-axis in the detector at z-levels (-40, -20, 0, 20, and 40 cm, top to bottom labeling).

4.4. Revised Gamma Detector Design

One difficulty with the original detector design is the elongated aspect ratio of the detector itself. Photomultiplier tubes (PMTs) have higher conversion efficiency if the surface area connecting the PMT to the scintillator is relatively small since there are more photons per unit area striking the surface. Taller scintillators suffer from large surface areas along the sides as well as self-shielding: emitted photons are re-absorbed within the detector, making it more difficult for photons to arrive at the end of the PMT [7, 22].

One possible solution is to make the detector less elongated but wider and thicker. Common commercial CsI(Tl) detectors are readily obtainable in $2 \times 4 \times 8$ inch^3 or $4 \times 4 \times 8$ inch^3 volumes. Several transport models were designed based on these two specifications, with two detectors working in tandem as a single unit with a total integrated signal; the $4 \times 4 \times 8$ inch^3 deterministic adjoint model geometry is shown in Figure 4.3.

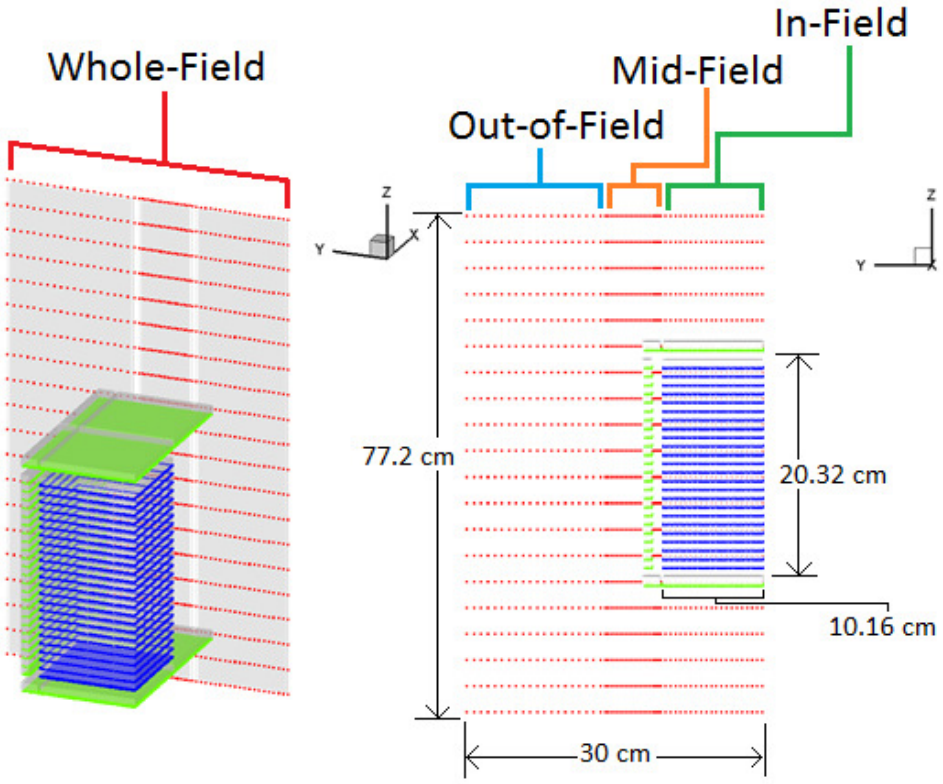

Figure 4.3: (Left) Isotropic view of the $4 \times 4 \times 8$ inch^3 CsI detector and (Right) *y-z* planar view. The background is half of the source plane, and the right portion of each image represents a specular reflective boundary condition. The thin volumetric source plane dimensions in this image are 30 cm × 0.1 cm × 77.2 cm. Three distinct source plane bands mark (from left to right) the Out-of-Field region, the Mid-Field region, and the In-Field region, as shown. When considered together, they are referred to as "Whole Field Region" in this thesis.

In order to determine detector reaction rates for various collimator and source configurations, a series of deterministic S_N adjoint calculations were computed. As

discussed earlier, adjoint calculations have a unique advantage in that they effectively yield a detector efficiency phase space that is independent of the source term, allowing for rapid calculation of reaction rates for different source configurations. Since our analysis characterizes roughly 160 different possible permutations, the ability to easily calculate reaction rates for various source configurations is a definite advantage. Furthermore this reduces the amount of forward calculations dramatically since we determined that our models were adequately converged to achieve total reaction rates by either forward or adjoint methods, and were almost identical (to within two percent). The adjoint approach enabled one to "step" detectors along the field of view relative to multiple sources sequentially to obtain the true counts attributed.

Traditionally the angular dependence in the adjoint importance is preserved when the adjoint current importance is coupled with the forward source current term, as shown in the Eq. 4.4 below.

$$R_{adj}\left[\frac{photons}{second}\right] = \langle J^{\dagger} q_{fwd}^{-} A \rangle \qquad \text{Eq. 4.4}$$

Where $J^{\dagger}$ the adjoint is current $[\frac{\emptyset}{cm^2\ s}]$ streaming away from the detector, q_{fwd}^{-} is the forward source current projected towards the detector $[photons]$, and A is the area of the source plane coupling both regions $[cm^2]$.

For a volumetric source, it is possible to simplify this further, since the source is modeled as a very thin (0.1 cm) volumetric source, and the detector is localized equidistant from the source box plane relative to the SNM source. For a volumetric

problem, it is possible to show in Eq. 2.12 and Eq. 2.13 the equivalency of forward and adjoint reaction rates.

The adjoint reaction rate $\left[\frac{photons}{second}\right]$ interacting in the detector for the volumetric source case can be calculated by Eq. 4.5:

$$R_{adj}\ \left[\frac{photons}{second}\right] = \langle \varphi^{\dagger} q_{fwd} \Delta V_s \rangle \qquad \text{Eq. 4.5}$$

Where the brackets $\langle\ \rangle$ denote integration over the entire phase space, $\varphi^{\dagger}$ is the scalar adjoint importance (unitless), q_{fwd} is the forward source $\left[\frac{photons}{cm^3\ s}\right]$, and ΔV_s are the volumes of the cells occupied by the source (cm^3) [39].

4.5. Transport Methodology

Previous work by Al Basheer, Sjoden, and Ghita (2010) shows that an S_N quadrature order of 32 (1088 directions per mesh) is required to minimize ray-effects for gamma calculations in air in meshes on the order of 1 cm [14]. When computing the source box and collimator models deterministically, an S_N quadrature of 42 (with a total of 1848 directions per mesh) and 30 (a total of 960 directions per mesh) were used, respectively. The mesh density was high enough along with the number of directions such that artificial ray effects indicating directional under-sampling were not observed. An exception is the observable difference in magnitude of the collimator inducing a ray effect outward from the detector in the adjoint models. In optically thin regions such as air, the mesh size was set to roughly 0.1 cm to account for strong gradients in the flux (or adjoint importance) in the vicinity of forward and adjoint sources. The global coarse mesh tolerance for all of these deterministic runs were set to 1.0×10^{-5}.

4.6. Gamma Source Term Treatment

A previous analysis shows that the results of the space-angle dependence of the source for gammas emitted from the source box can be approximated as an isotropic, thin, volumetric source distal from the detector [40]. However, it is important to ensure that the magnitude of the isotropic volumetric source is equivalent to the outward current originating from the source box. The source term from the source book is set up as an absolute rate S_o (photons/sec) emanating from a single YZ side of the outer source box spanning (60 cm × 0.1 cm × 77.2 cm).

To simplify our analysis, the source was modeled as a very thin volumetric source instead of a surface source. This was completed by utilizing the surface current leakage from one side of the source box (photons/sec) and dividing it by an artificially thin volume which is defined over the whole outer source box (denoted as Whole Field). When the adjoint reaction rates are re-calculated this volumetric term is multiplied back out. In order to preserve the source term, transitioning from the single direction $-\widehat{\boldsymbol{\Omega}}_{\boldsymbol{x}}$ to an isotropic source implies doubling the source magnitude to $2S_o$. However, the source term was modeled as a half-source (30 cm × 0.1 cm × 77.2 cm) with a specular reflective boundary; as a half-source the source magnitude then returns to the basis magnitude of S_o. This is graphically shown in Figure 4.4. Ensuring that the source box maintains its proper dimension within the transport models allows for proper coupling of the adjoint importance with the forward source term. This eliminates the need for a "full-physics" model with the SNM canister explicitly modeled, as well as allowing analysis of the axial behavior of the reaction rate.

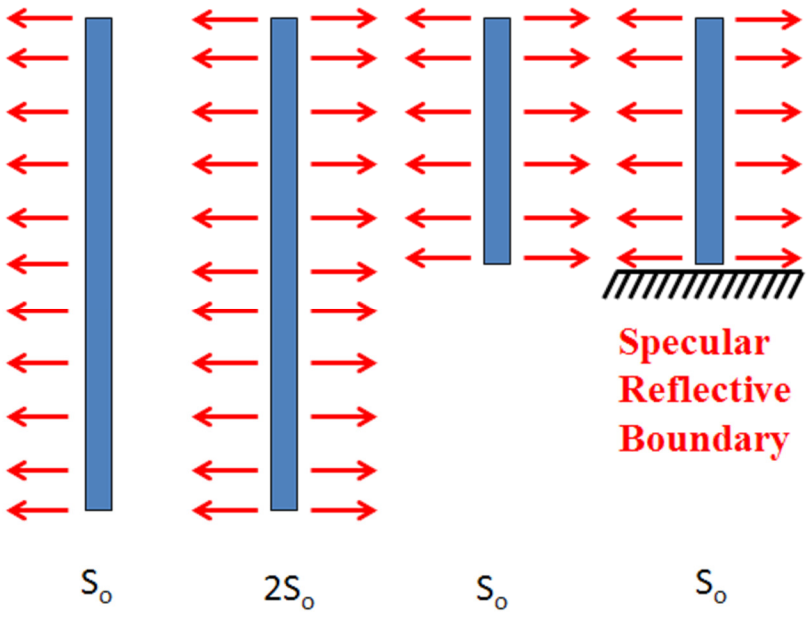

Figure 4.4: Source term treatment modeling. From left to right: Current emanating from full source box with magnitude S_o. Isotropic source modeled from full source box with magnitude $2S_o$. Half-isotropic source with a magnitude of S_o. Half-isotropic source with specular reflective boundaries with a magnitude of S_o.

4.7. Simplified Approximation Using Isotropic Point Source Folded with Detector Adjoint

A very simplified upper bound for expected detector counts can be estimated, since photons emanating from the SNM source will be streaming through air, which has low density (implying a large mean free path), absorption and scattering cross sections. Moreover, a rough estimate can be determined if the source is considered as an isotropic point source that is 30 cm away from the outer source box plane. A $\frac{1}{4\pi r^2}$ correction factor was used to account for spherical divergence from this idealized point source term. The adjoint importances from the 30 cm source-detector case for the $4 \times 4 \times 8$ inch^3 CsI detector without collimation were summed over the In-Field and Out-of-Field regions using 3-D interpolated values in 1 cm increments, as in Eq. 4.6, summed over all

applicable cells. Note this approximate approach does not take into account any further transport effects (scattering, leakage, or streaming) besides those as a consequence of the adjoint importance term.

$$[p]R_{adj}\ dt \approx \frac{1}{4\pi r^2}\left[\frac{1}{cm^2}\right]\sum_{i=1}^{N}\varphi_i^{\dagger}\,[\emptyset]q_{fwd}\left[\frac{p}{cm^3 s}\right]V_{src}[cm^3]A_{plane}[cm^2]dt[s] \qquad \text{Eq. 4.6}$$

In Eq. 4.6, $R_{adj} \cdot dt$ is the total counts at the detector within a defined linear FOV, $\varphi_i^{\dagger}$ is the spatial adjoint importance at a specified mesh i, r is the distance from the isotropic point source to the outer source box plane, q_{fwd} is the idealized forward isotropic volumetric source density term at the center of the SNM canister, V_{src} is the volume of the source (here considered to be 1 cm^3), A_{plane} is the area of the source box plane (30 cm × 77.2 cm), and *dt* is the time taken for the detector to pass through a particular linear FOV at a given speed. Note that the adjoint importances are summed over space and not energy, and that the spatial bounds of summation depend on whether or not the In-Field or Out-of-Field planes are considered.

Table 4.1: Approximate 'In-Field' Gamma detector counts resulting from Eq. 4.6.

Source Type	1 mph	2 mph	3 mph	4 mph	5 mph
HEU 1yr Shell	42.2	21.0	14.0	10.5	8.40
HEU 1 yr Solid	11.9	5.98	3.99	2.99	2.40
HEU 50 yr Shell	42.1	21.1	14.0	10.5	8.43
HEU 50 yr Solid	12.3	6.16	4.11	3.08	2.46
WGPu 22yr Shell	84.2	42.1	28.0	21.0	16.8
WGPu 22yr Solid	24.30	12.1	8.10	6.07	4.86

In general the detector counts from Table 4.1 overestimate the actual values, but provide a reasonable estimate for the approximate magnitude of the actual transport

calculations. Note that cases where >5 counts were registered are labeled in red, 2-5 counts were labeled in yellow, and <2 counts were labeled in green. Since the minimum detectable threshold for the 1.001 MeV line is approximately 4 counts in a half second time gate, the green coloration indicates that it passes the minimum detectable threshold for SNM activity. However, it is important to note that these count rates are upper bounds for the detector, since it does not take into account collisions or attenuation from the celotex/steel materials within the SNM container.

4.8. Equivalency of Forward and Adjoint Response: Model Convergence with Volumetric Source

An equivalent forward and adjoint computation was performed for the $4 \times 4 \times 8$ inch^3 CsI detector with 10 cm long and 1 cm thick tungsten collimator. The forward and adjoint reaction rates can be computed using Eq. 2.12 and Eq. 2.13, and as before the brackets ⟨ ⟩ indicate summation over the entire phase space [39]. In the following equations, we make use of the identity $\langle \psi^\dagger H \psi \rangle = \langle \psi H^\dagger \psi^\dagger \rangle$ discussed previously in Section 2.2 in order to exactly relate the forward and adjoint reaction rates.

Slices through the model center for adjoint (Figure 4.5) and forward (Figure 4.6) for 1.001 MeV gammas reveal the nature of the adjoint calculation aliased to detector efficiency and the forward source particles emitted along the FOV traveling toward the detector. The forward and adjoint models have identical geometries, quadrature, and meshing.

The forward sources provided in the SNM Source Book [12] were divided by the volume of the source in the model then fed into a modified version of Dr. Scottie Walker's volumetric adjoint AREACT code [41]. A separate bash script was created to

run AREACT for an arbitrary amount of forward sources, making the calculation of adjoint reaction rates straightforward.

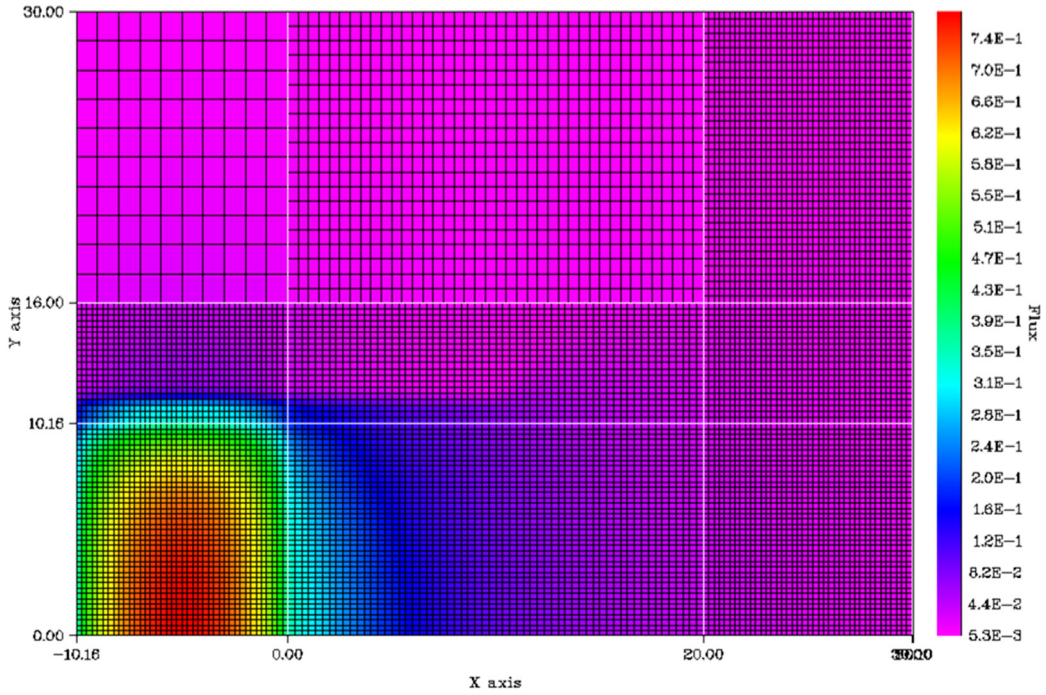

Figure 4.5: Gamma adjoint importances for the 4 × 4 × 8 inch^3 CsI detector with 10 cm long and 1 cm thick tungsten collimator for the 1.001 MeV line.

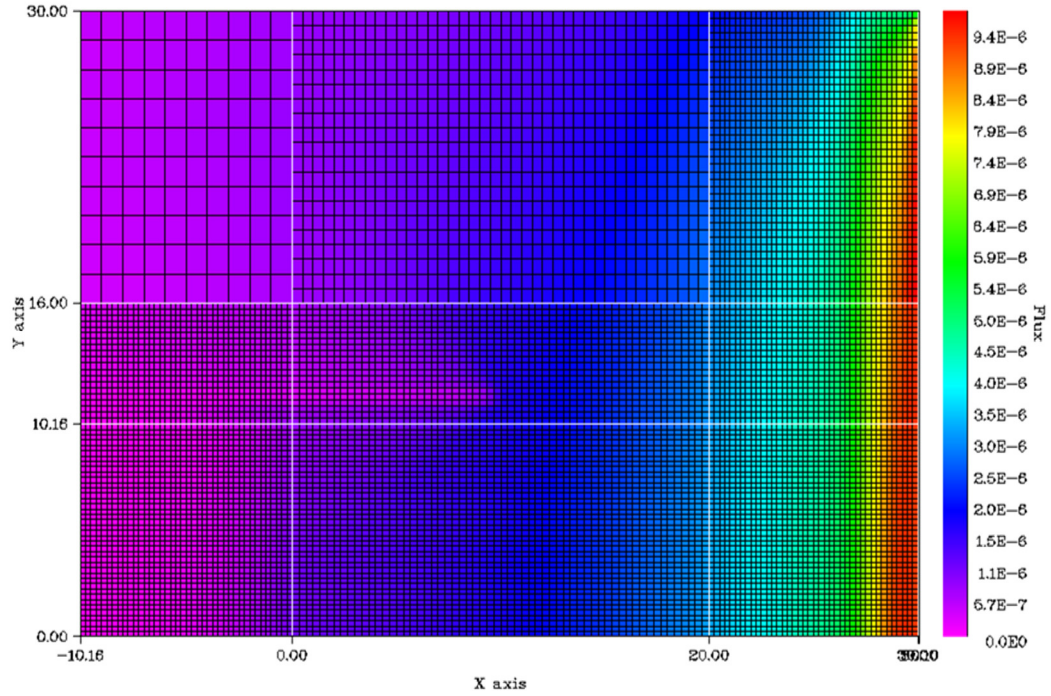

Figure 4.6: Forward photon fluxes for the 4 × 4 × 8 inch^3 CsI detector with 10 cm long and 1 cm thick tungsten collimator for the 1.001 MeV line.

Note that the percent differences are lowest at the lowest energy bin and highest at the highest energy bin. This is because the adjoint and forward reaction rates show differences in how the photons stream from the (forward or adjoint) sources.

The source term used in the forward source is a volumetric isotropic source with a source magnitude equal to the one particle per unit mesh volume. The source term used in the adjoint source was normalized to unity so that the adjoint importance correlate with the overall detector efficiency aliased to the absorption cross section of CsI from group 1 to group 24. The source spectrum for the forward case was the normalized PDF of the HEU gamma line spectrum for 25 kg 1 year HEU shell geometry. The adjoint reaction rates were tallied within the source volume, while the forward reaction rates were tallied within the detector volume as shown in Eq. 2.12 and Eq. 2.13, respectively.

Because of the mathematically different approach to the reaction rate indicated, the differences slightly diverge as a function of energy for an isotropic source. The overall percent difference for the total reaction rate computed with either method was within approximately two percent. While this difference is very small (and in theory should be zero), it is expected that this error can be reduced by phase space refinement; because the two methods use "opposite" approaches, it is clear the models, be it forward or adjoint, are consistent. For our purposes of determining adequate count rates for the detector platform(s), the currently prescribed volumetric tallying of detector response with these models should be adequate.

Table 4.2: Energy-Dependent Forward and Adjoint Volumetric Reaction Rates in Photons/second for equivalent model convergence assessment. Because of the mathematically different approach to the reaction rate indicated, only the total count rate is directly comparable for the two methods.

Group	Upper Energy (MeV)	Lower Energy (MeV)	Adjoint Reaction Rate (Photons/s)	Forward Reaction Rate (Photons/s)
24	0.3000	0.000	3.495	3.572
23	0.741	0.300	2.058×10^{-2}	2.292×10^{-2}
22	0.743	0.741	2.247×10^{-4}	9.918×10^{-5}
21	0.765	0.743	1.027×10^{-4}	8.562×10^{-5}
20	0.767	0.765	4.848×10^{-4}	2.031×10^{-4}
19	0.954	0.767	1.201×10^{-3}	6.554×10^{-4}
18	0.956	0.954	1.917×10^{-3}	7.980×10^{-6}
17	0.999	0.956	1.400×10^{-4}	7.516×10^{-5}
16	1.002	0.999	1.691×10^{-3}	5.599×10^{-4}
15	1.180	1.002	9.865×10^{-5}	4.952×10^{-5}
14	1.200	1.180	3.394×10^{-5}	1.136×10^{-5}
13	1.240	1.200	2.739×10^{-5}	1.055×10^{-5}
12	1.260	1.240	8.225×10^{-6}	3.571×10^{-6}
11	1.500	1.260	1.167×10^{-4}	4.203×10^{-5}
10	1.520	1.500	4.146×10^{-5}	1.102×10^{-5}
9	1.736	1.520	1.071×10^{-4}	3.147×10^{-5}
8	1.740	1.736	6.000×10^{-5}	1.450×10^{-5}
7	1.760	1.740	1.121×10^{-5}	2.969×10^{-6}
6	1.830	1.760	4.820×10^{-5}	1.234×10^{-5}
5	1.832	1.830	4.688×10^{-5}	1.123×10^{-5}
4	2.210	1.832	9.367×10^{-5}	2.355×10^{-5}
3	2.250	2.210	3.435×10^{-7}	8.480×10^{-8}
2	2.749	2.250	3.519×10^{-7}	9.844×10^{-8}
1	2.750	2.749	3.821×10^{-7}	9.811×10^{-8}
Total			3.521	3.597

The total reaction rate of Table 4.2 is 2.15% different between the forward and adjoint cases. The individual group differences deviate at higher energies due to the fundamentally different ways the forward particles and the adjoint "particles" stream out from their respective sources.

4.9. Equivalency of Forward and Adjoint Response: Model Convergence with Surface Source

The standard definition for current (for example in the x direction) in radiation transport are described as:

$$J_x^+ = \int_0^{2\pi} d\phi \int_0^1 \mu \; \psi\left(\vec{r}, \widehat{\Omega}\right) d\mu \qquad \text{Eq. 4.7}$$

$$J_x^- = \int_0^{2\pi} d\phi \int_{-1}^0 \mu \; \psi\left(\vec{r}, \widehat{\Omega}\right) d\mu \qquad \text{Eq. 4.8}$$

Recall that for a surface source the equation for adjoint reaction rate is re-shown as:

$$R_{adj} = \left\langle {J^\dagger}^+ q_{fwd}^- \Delta A_s \right\rangle \qquad \text{Eq. 4.9}$$

Where ${J^\dagger}^+$ is the adjoint current $(unitless)$ streaming from the detector face, J^+ is the forward current $(\frac{particles}{cm^2\ s})$, σ_d is the isotropic detector absorption macroscopic cross section $(\frac{1}{cm})$, and ΔV_d is the detector volume (cm^3), the q_{fwd}^- term is the forward source current projected towards the detector $(\frac{particles}{cm^2\ s})$, and ΔA_s is the area of the source plane coupling both regions (cm^2). The forward source current (JminX-1/2) and the group-flipped adjoint surface current (JplsX-1/2) were pulled as output from PENDATA's J-Net Surface Option.

Note that the surface and volumetric current forward and adjoint cases are not as comparable as their volumetric equivalents; this is due to a number of possible reasons: transport scattering effects in the source region (mitigated by the low density of air defined in the source region), quadrature streaming (a non-isotropic forward source will be streaming particles in a particular direction with a set quadrature, which would be

different than an isotropic adjoint source located at the detector), and space-angle dependence (a non-isotropic forward source has a different spatial profile compared to a mono-directional beam or an isotropic source). These effects were partially compensated by adjusting the volume in Eq. 2.12 and Eq. 2.13 to provide an equivalent current into the detector plane as the forward surface case. An example of this is shown in in Figure 4.9. This analysis was performed for the $4 \times 4 \times 8$ in^3 CsI detector with 10 cm long and 5 cm thick collimator with a precisely defined non-isotropic forward surface source, the respective adjoint and forward flux plots for the 1.001 MeV energy line are shown in Figure 4.7 and Figure 4.8 respectively.

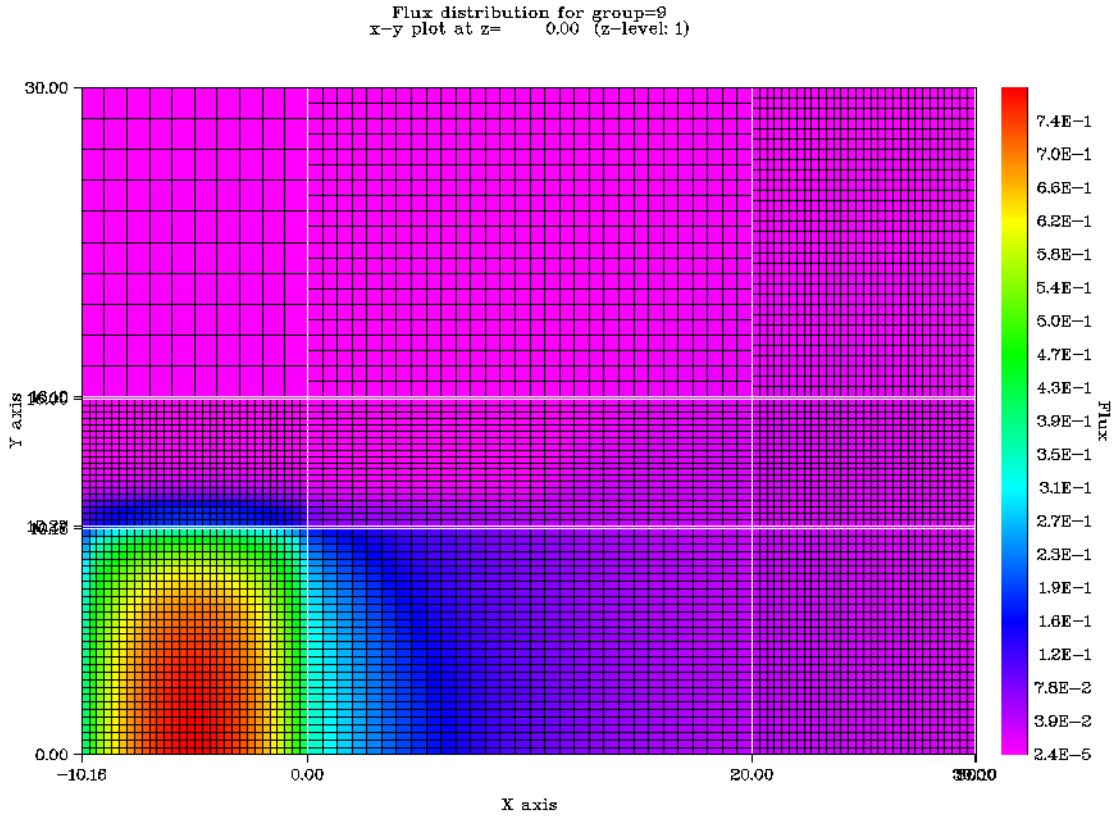

Figure 4.7: Gamma adjoint importances for the $4 \times 4 \times 8$ inch^3 CsI detector with 10 cm long and 5 cm thick tungsten collimator for the 1.001 MeV line.

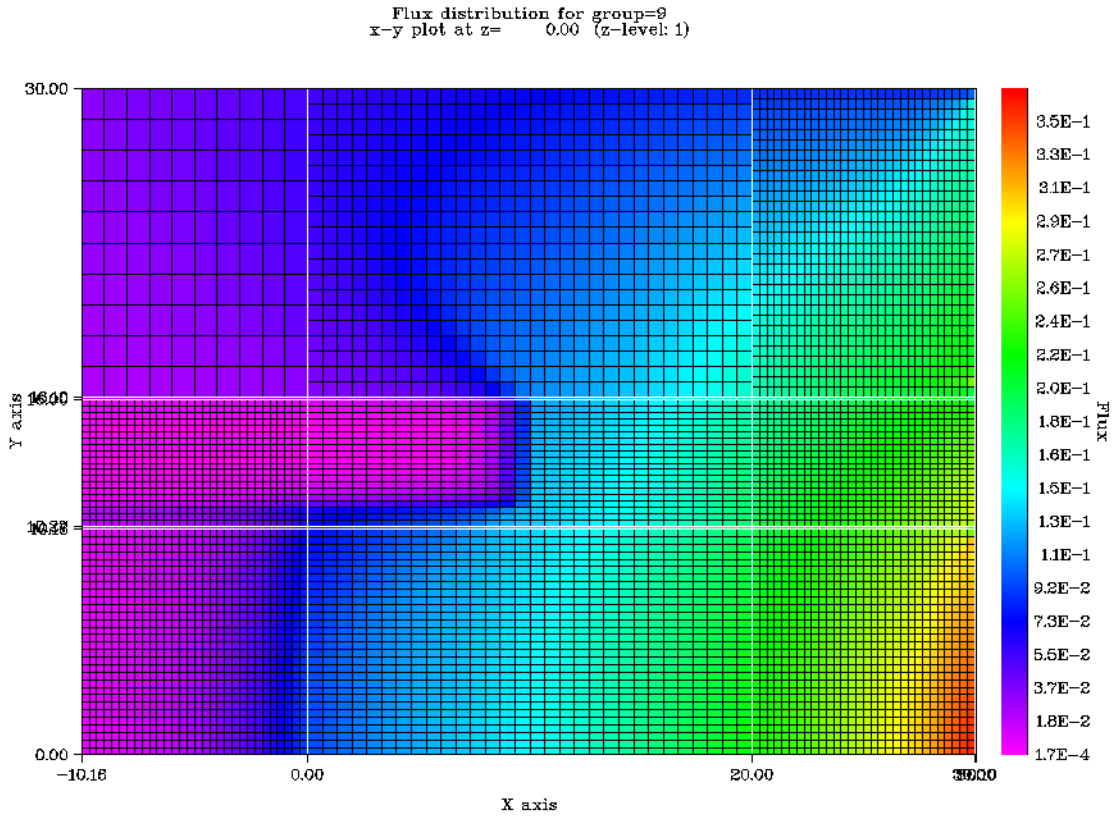

Figure 4.8: Forward photon fluxes for the 4 × 4 × 8 inch^3 CsI detector with 10 cm long and 5 cm thick tungsten collimator for the 1.001 MeV line.

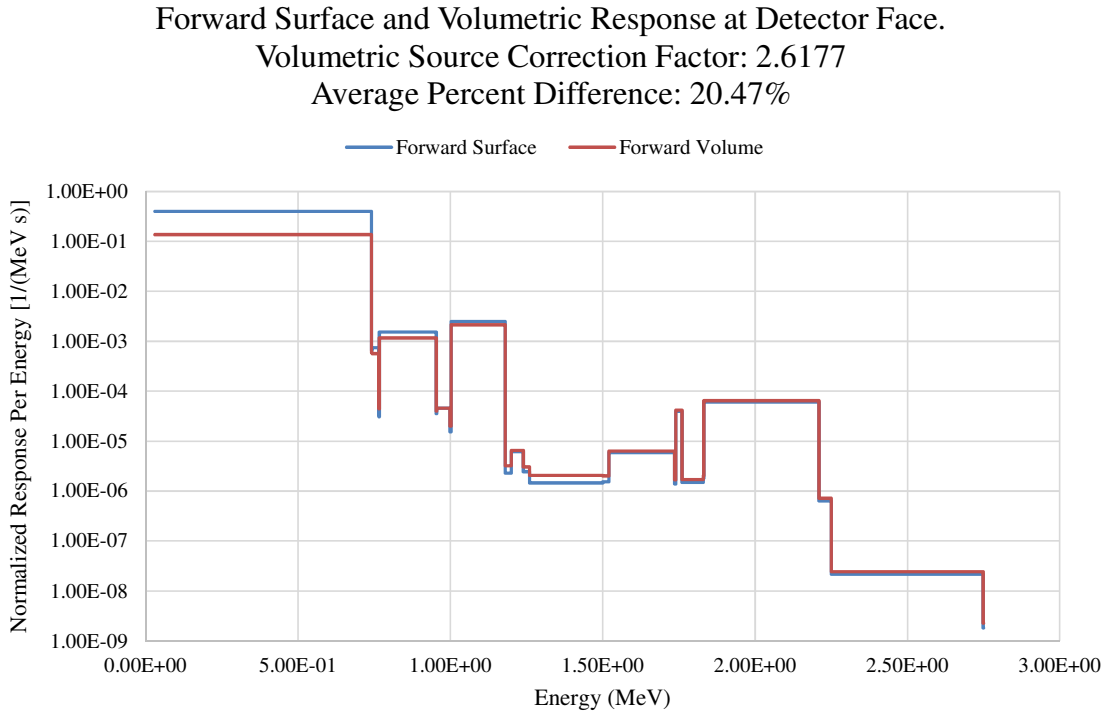

Figure 4.9: Surface and Volumetric Forward Reaction Rate Comparison. Note that the volumetric case was corrected by multiplying the volume by a factor of 2.6177, determined by the average deviation between the two cases without the factor applied. Also note that if the first group is neglected, the average percent difference drops to 17.12%

Tabulated results from Figure 4.9 are shown in Table 4.3. The first group was particularly difficult to get converged results between the two methods due to the extremely low energies involved (both absorption and quadrature effects present skew the answer to positively bias the non-isotropic, forward-peaked surface source compared to the isotropic volume source).

Table 4.3: Energy-Dependent Forward Volumetric Reaction Rates and Forward Surface Reaction Rates in the detector for Normalized Per Source Particle (S_{42} PENTRAN calculation).

Group	Upper Energy (MeV)	Lower Energy (MeV)	Normalized Forward Volume Reaction Rate (Photons/s)	Normalized Forward Surface Reaction Rate (Photons/s)	Percent Difference (%)
24	0.300	0.000	4.090E-02	1.188E-01	97.577
23	0.741	0.300	2.625E-04	2.924E-04	10.783
22	0.743	0.741	1.136E-06	1.481E-06	26.425
21	0.765	0.743	9.804E-07	6.851E-07	35.462
20	0.767	0.765	2.325E-06	3.058E-06	27.226
19	0.954	0.767	7.505E-06	6.667E-06	11.816
18	0.956	0.954	9.138E-08	9.140E-08	0.032
17	0.999	0.956	8.606E-07	6.587E-07	26.577
16	1.002	0.999	6.412E-06	7.525E-06	15.976
15	1.180	1.002	5.670E-07	4.077E-07	32.681
14	1.200	1.180	1.301E-07	1.235E-07	5.240
13	1.240	1.200	1.209E-07	9.787E-08	21.014
12	1.260	1.240	4.089E-08	2.887E-08	34.463
11	1.500	1.260	4.813E-07	3.692E-07	26.355
10	1.520	1.500	1.262E-07	1.190E-07	5.912
9	1.736	1.520	3.603E-07	2.963E-07	19.506
8	1.740	1.736	1.660E-07	1.587E-07	4.507
7	1.760	1.740	3.400E-08	2.976E-08	13.289
6	1.830	1.760	1.413E-07	1.264E-07	11.099
5	1.832	1.830	1.286E-07	1.216E-07	5.567
4	2.210	1.832	2.696E-07	2.388E-07	12.150
3	2.250	2.210	9.711E-10	8.648E-10	11.571
2	2.749	2.250	1.127E-09	8.988E-10	22.546
1	2.750	2.749	1.123E-09	9.809E-10	13.549
Total			4.119E-02	1.192E-01	97.250

A comparison between the adjoint response rates between the surface and the volumetric datasets is shown in Figure 4.10.

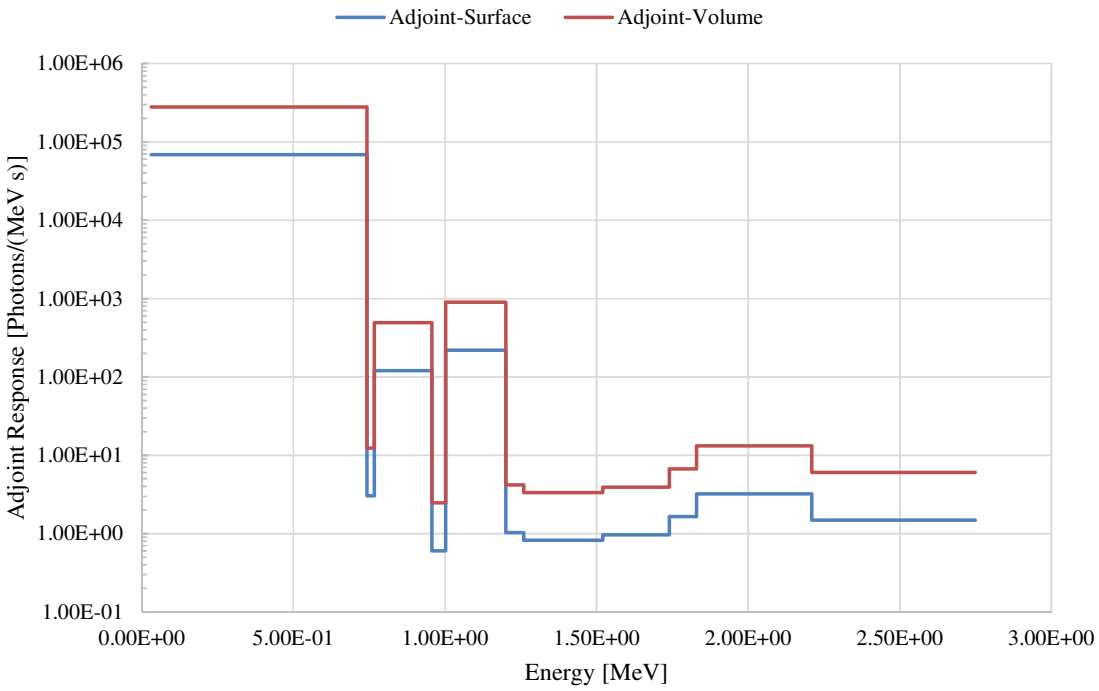

Figure 4.10: Surface and Volumetric Adjoint Reaction Rate Comparison for an isotropic adjoint flux. Note that the adjoint volume calculation is approximately[2] 4 times the adjoint surface calculation, explained by current and flux definition differences.

There was a consistent factor of ~4 magnitude difference between the adjoint surface and adjoint volume case. This is consistent with the relationship between current and flux diffusion relationship (by integrating Eq. 4.7 and Eq. 4.8) [42]:

$$J_{\pm}(\vec{r},t) = \frac{1}{4}\phi(\vec{r},t) \qquad \text{Eq. 4.10}$$

The forward and adjoint surface response rates are found in Table 4.4 and Figure 4.11.

[2] Note: The approximate value averaged over all groups is 4.3712.

Table 4.4: Energy-Dependent Forward and Adjoint Surface Reaction Rates in Photons/second for 4 × 4 × 8 in^3 CsI detector with 10 cm long and 5 cm thick tungsten collimator.

Group	Upper Energy (MeV)	Lower Energy (MeV)	Adjoint Reaction Rate (Photons/s)	Forward Reaction Rate (Photons/s)
24	0.300	0.000	1.590E+04	1.543E+05
23	0.741	0.300	1.051E+02	3.717E+02
22	0.743	0.741	1.220E+00	1.888E+00
21	0.765	0.743	5.413E-01	8.443E-01
20	0.767	0.765	2.493E+00	3.899E+00
19	0.954	0.767	6.395E+00	8.330E+00
18	0.956	0.954	1.053E-01	1.149E-01
17	0.999	0.956	7.739E-01	8.146E-01
16	1.002	0.999	9.327E+00	9.543E+00
15	1.180	1.002	5.560E-01	5.016E-01
14	1.200	1.180	1.982E-01	1.547E-01
13	1.240	1.200	1.638E-01	1.214E-01
12	1.260	1.240	4.976E-02	3.544E-02
11	1.500	1.260	7.240E-01	4.560E-01
10	1.520	1.500	2.664E-01	1.490E-01
9	1.736	1.520	7.026E-01	3.678E-01
8	1.740	1.736	3.932E-01	1.992E-01
7	1.760	1.740	7.396E-02	3.712E-02
6	1.830	1.760	3.274E-01	1.579E-01
5	1.832	1.830	3.294E-01	1.525E-01
4	2.210	1.832	6.427E-01	2.981E-01
3	2.250	2.210	2.288E-03	1.081E-03
2	2.749	2.250	2.481E-03	1.114E-03
1	2.750	2.749	2.988E-03	1.225E-03
Total			1.603E+04	1.547E+05

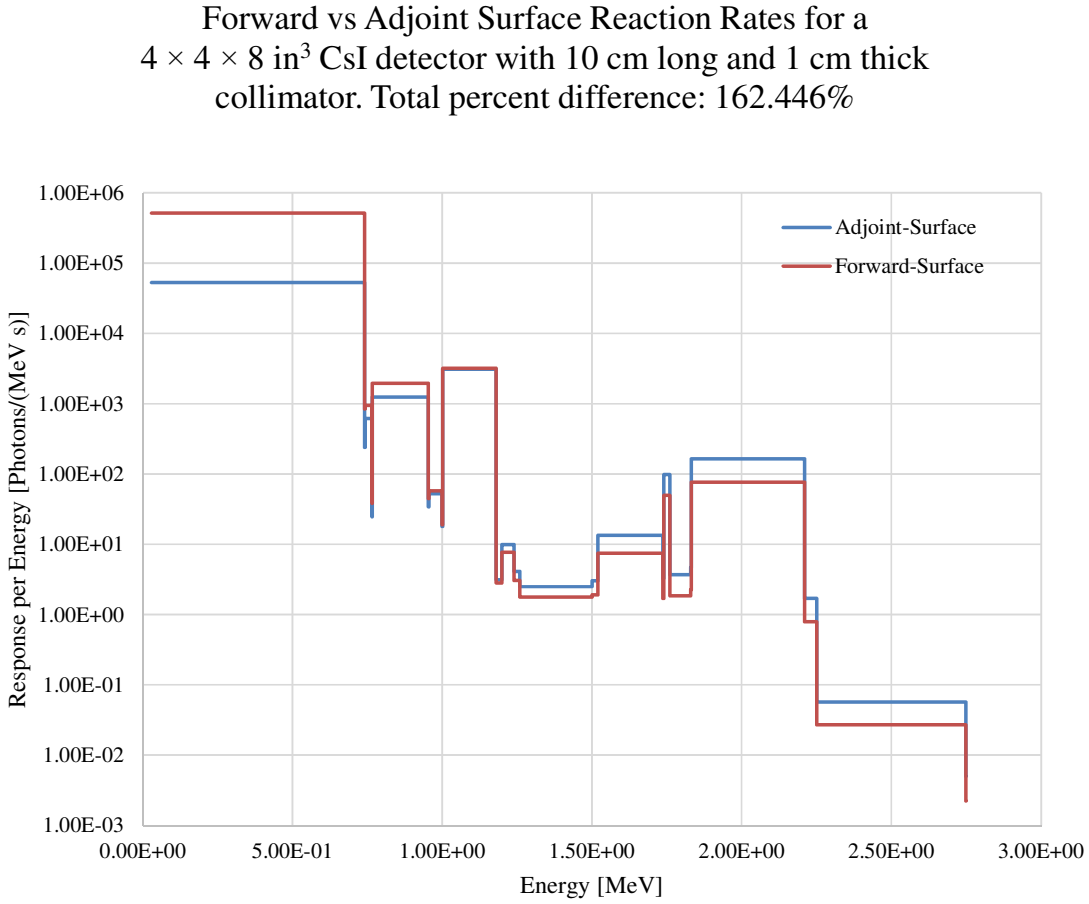

Figure 4.11: Histogram of Table 4.4, Group-dependent Reaction Rates for Forward and Adjoint Volumetric Source Transport Simulation of a 4 × 4 × 8 in^3 CsI detector with 10 cm long and 5 cm thick tungsten collimator.

The discrepancy in the lowest group between the adjoint surface response and the forward surface response in Figure 4.11 can be explained due to lumping all of the lowest energy contributions below 300 keV into a single energy bin as the 24th energy group. Since the $\frac{\mu}{\rho}$ can span several orders of magnitude (10^{-1} to 10^{3}) in this range it is difficult to get the adjoint and forward surface results to match. Since the premise of the MPVS is to look at higher energies (since the lower energy components will not be detected outside the canister) this was assumed to be a valid point.

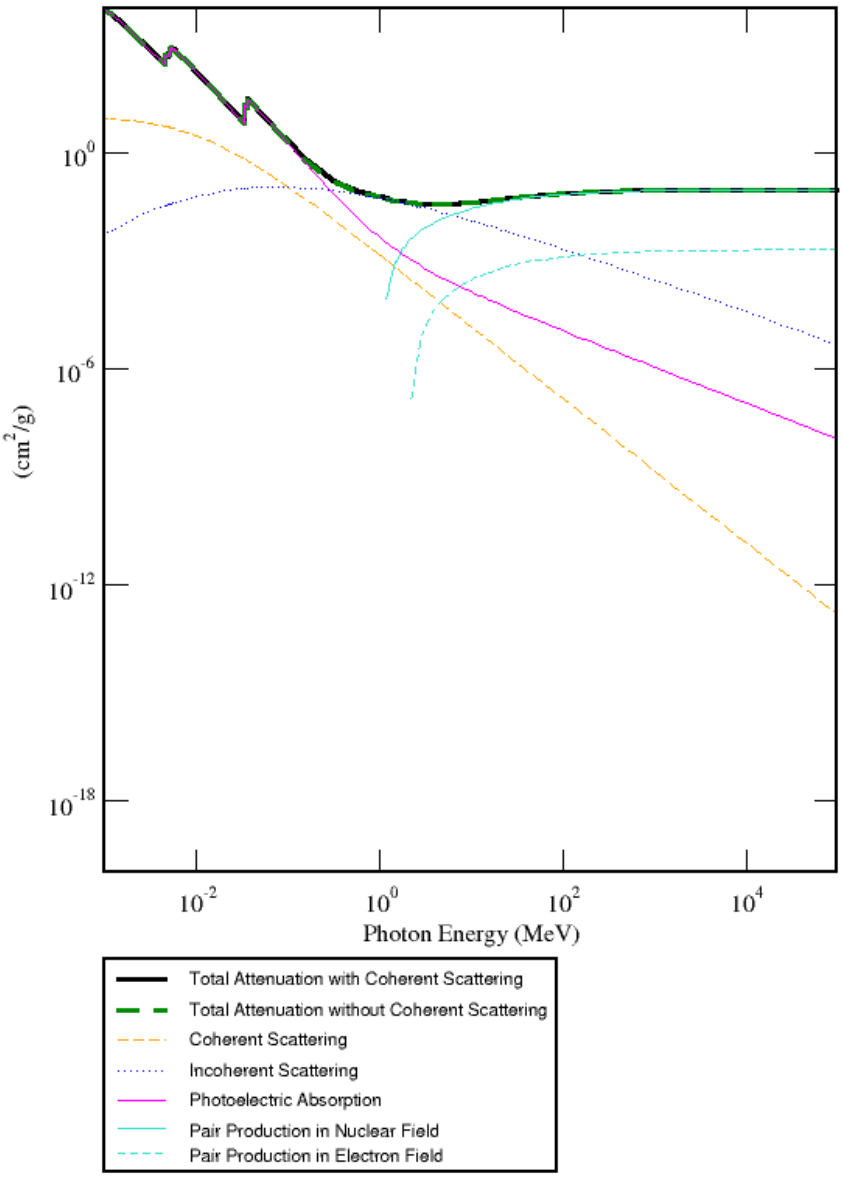

Figure 4.12: Microscopic cross sections (including Photoelectric Absorpion, Compton Scattering, and Pair Production) for CsI as a function of energy [43].

4.10. Gamma Source Centered Detector Counts

An analysis of the source centered response in the original proposed gamma detector design, which was for a 60 cm long 2.54 cm radius CsI cylindrical detector is given in Table 4.5. The data show that there is little difference between the "within FOV" response variation with collimator thickness.

Table 4.5: Source centered response rates using different thickness collimators for 60 cm long 2.54 cm radius CsI cylindrical detector using a thin volumetric source along right edge of model (30.01, 2.60, 0.0) to account for count rate in the FOV.

Collimator thickness→	1cm	5cm	1cm	5cm
Forward Source Case (volumetric)	0.999 – 1.002 MeV Adjoint Response Rate $\left(\frac{photons}{s}\right)$	0.999 – 1.002 MeV Adjoint Response Rate $\left(\frac{photons}{s}\right)$	Total Adjoint Response Rate $\left(\frac{photons}{s}\right)$	Total Adjoint Response Rate $\left(\frac{photons}{s}\right)$
HEU 1 year Shell	58.29	58.28	1.693×10^5	1.693×10^5
HEU 1 year Solid	16.59	16.58	3.434×10^4	3.434×10^4
HEU 50 year Shell	58.47	58.45	1.700×10^5	1.700×10^5
HEU 50 year Solid	17.13	17.13	4.812×10^4	4.812×10^4
WGPu 22.5 year Shell	7.3	7.3	5.370×10^7	5.370×10^7
WGPu 22.5 year Solid	8.5	8.5	2.033×10^7	2.033×10^7

There is not much of a difference between the 1 cm and 5 cm cases, though this is to be expected since the summation in Eq. 2.13 occurred only for the In-Field region only. There is a distinction to be made between the In-Field and Out-of-Field regions, which will be discussed in Section 4.11.

4.11. In-Field vs. Out-of-Field Detector Response Comparisons

The MPVS platform is designed to move at a constant speed and accumulate a signal for each stored weapon pit container, while time-gating intervals of time dt within a particular linear FOV centered on each mass. As such, there are several different ways to handle the ΔV_s volume term in Eq. 2.13; one important question is how to define the adjoint source volume in a consistent manner. Are counts only considered within the linear FOV within the collimator window? How much conflicting signal is possibly mitigated by time-gating to cut off signal counts for the accumulated signal outside the angular FOV of the detector? It turns out that both of these are important considerations which address different design questions. By repeating the analysis from Eq. 4.1, Eq. 4.2, Eq. 4.3 and Eq. 4.5, but only considering the region "outside" the FOV seen by the detector it is possible to assess the impact of "Out-of-Field" counts which implicitly determine the effectiveness of the collimation.

In Figure 4.3 there are three source regions that were defined: In-Field, Mid-Field, and Out-of-Field. The adjoint importance and source volumes ΔV_s within these three regions vary, with the adjoint importance changes shown in Figure 4.2. The impact of the Out-of-Field counts due to the collimation in place should be smaller than the In-Field results given the order of magnitude lower adjoint importance in the Out-of-Field region. A comparison of the 1 cm and 5 cm thick collimators (with all other variables equal) is shown in Table 4.6 and Table 4.7. We note here that below 2 counts is desirable, and more than 5 counts accumulated is deemed problematic for Out of Field sampling nearby a targeted container under inspection (based on the background studies performed). As a

result, in Table 4.6 and Table 4.7, cases >5 counts were labeled in red, 2-5 counts were labeled in yellow, and <2 counts were labeled in green.

Table 4.6: Out-of-Field detector counts for 60 cm long 2.54 cm radius CsI cylindrical detector for the 30 cm source-detector distance, 5 cm long, 1 cm thick Tungsten collimator. Adjoint response tallied for the 1.001 MeV line over 34.68 degree angular FOV with a 41.52 cm linear FOV.

Source Type	1 mph	2 mph	3 mph	4 mph	5 mph
HEU 1yr Shell	30.6	15.3	10.2	7.6	6.1
HEU 1 yr Solid	8.7	4.3	2.9	2.2	1.7
HEU 50 yr Shell	30.6	15.3	10.2	7.7	6.1
HEU 50 yr Solid	9.0	4.5	3.0	2.2	1.8
WGPu 22yr Shell	61.3	30.6	20.4	15.3	12.2
WGPu 22yr Solid	1.4	0.7	0.5	0.3	0.3

Table 4.7: Out-of-Field detector counts for 60 cm long 2.54 cm radius CsI cylindrical detector for the 30 cm source-detector distance, 5 cm long, 5 cm thick Tungsten collimator. Adjoint response tallied for the 1.001 MeV line over 34.68 degree angular FOV with a 41.52 cm linear FOV.

Source Type	1 mph	2 mph	3 mph	4 mph	5 mph
HEU 1yr Shell	19.2	9.6	6.4	4.8	3.8
HEU 1 yr Solid	5.5	2.7	1.8	1.4	1.1
HEU 50 yr Shell	19.3	9.6	6.4	4.8	3.8
HEU 50 yr Solid	5.6	2.8	1.9	1.4	1.1
WGPu 22yr Shell	38.5	19.2	12.8	9.6	7.6
WGPu 22yr Solid	0.9	0.4	0.3	0.2	0.2

The impact of the thicker tungsten collimator in Table 4.7 is noticeable compared to Table 4.6, as it allows for approximately one MFP of perpendicular distance traveled. Since the goal is to maximize the In-Field results while minimizing the Out-of-Field results, this would normally present a significant constraint on how to effectively

collimate the detector. However, the counts in Table 4.6 and Table 4.7 do not have to be lower than a certain threshold value, since the detector count accumulations will be controlled due to time gating the detector circuit while it is entering the Out-of-Field region. One important assumption made when calculating the Out-of-Field counts is that the effective integrated time is the same as that of the In-Field count calculation. By setting the Out-of-Field counts on the same time basis as the In-Field counts, comparisons can be made between collimators of different thicknesses. All things considered, this is an important distinction as it allows us to only consider summed counts within a linear FOV of the In-Field region. Moreover, the adjoint importances between the 1 cm thick case and 5 cm thick case drop by roughly 10% on average over all groups. Since from Table 4.5 we know that the impact of In-Field count rates from the 1 cm and 5 cm cases are practically indistinguishable (and noting the In-Field counts will be used as the baseline for detection), and with time-gating such that the Out-of-Field signal will not be observed, it is sufficient to say that a 1 cm thick collimator should be adequate for most cases. For a very hot background area higher than that considered in Section 2.3, or where containers have closer spacing, it may be necessary to increase the collimation thickness to 5 cm or more to control the out of field radiation influence in this application.

Since the detector platform will be moving, the linear FOV will also be moving with respect to it. In order to account for the relative motion of the detector to the source, one simplification can be made by assuming that the counts can be summed over the entire Whole-Field region, but only integrated within the time interval *dt* with Eq. 4.3. This "smears" out the counts over a larger effective time *dt*, but in practice does not yield

much of a difference since a comparison between the In-Field and Whole-Field region; this is because most (>85%) of the adjoint importance signal resides within the In-Field region.

4.12. FOV Response for Cylindrical CsI Detector

The results for the 2.54 cm radius cylindrical detector for four cases considering detection of radiation focused around the 1.001 MeV energy bin (the largest high energy emission for HEU) for different vehicle speeds are shown in Table 4.8 to Table 4.11, all with 5 cm thickness tungsten collimators. Table 4.8 considers a 30 cm source to detector distance with a 5 cm long collimator; Table 5.7 is similar, but considers a 15 cm long collimator. Table 4.10 and Table 4.11 repeat the determination of detected counts with different length collimators (5 and 15 cm long, respectively), but consider a 50 cm source to detector distance.

The adjoint response rates are shown in Table 4.5, which are then used with Eq. 4.1 to Eq. 4.2, with the result from Eq. 4.3 being multiplied by Eq. 2.13 to yield a total counts observed in the detector, neglecting losses for detector-specific criteria (dead-time, etc). All values in this section utilize an adjoint-coupled methodology (as discussed in more detail in Section 4.8 and Section 4.9) to determine the source response while moving across the detector FOV, where the adjoint variation directly accounts for the detector efficiency as the source moves across the FOV. Note that the FOV is defined as In-Field, Out-of-Field, or Whole Field. Recall that in each of the tables, the green shaded areas represent the detector responses that are > 5 counts over the FOV, yellow indicates a result between 2 and 5 counts gathered in the FOV, and red indicates < 2 counts in the

FOV. The yellow case is considered a "borderline" level of detection, and red cases are considered unacceptable, as they are likely at or below typical threshold count levels for the MPVS application. Note as already discussed, these colors are inverted relative to the Out-of-Field region, as it is more beneficial to have lower detectable counts when outside the field of view of the collimator.

Table 4.8: In-Field detector counts for 60 cm long 2.54 cm radius CsI cylindrical detector for the 30 cm source-detector distance, 5 cm long, 5 cm thick Tungsten collimator. Adjoint response tallied for the 1.001 MeV line over 34.68 degree angular FOV with a 41.52 cm linear FOV.

Source Type	1 mph	2 mph	3 mph	4 mph	5 mph
HEU 1yr Shell	54.1	27.1	18.0	13.5	10.8
HEU 1 yr Solid	15.4	7.7	5.1	3.8	3.1
HEU 50 yr Shell	54.2	27.1	18.0	13.5	10.8
HEU 50 yr Solid	15.9	7.9	5.3	3.9	3.2
WGPu 22yr Shell	6.8	3.4	2.3	1.7	1.3
WGPu 22yr Solid	7.9	3.9	2.6	1.9	1.6

Table 4.9: In-Field detector counts for 60 cm long 2.54 cm radius CsI cylindrical detector for the 30 cm source-detector distance, 15 cm long, 5 cm thick Tungsten collimator. Adjoint response tallied for the 1.001 MeV line over 12.989 degree angular FOV with a 13.84 cm linear FOV.

Source Type	1 mph	2 mph	3 mph	4 mph	5 mph
HEU 1yr Shell	18.3	9.2	6.1	4.6	3.6
HEU 1 yr Solid	5.2	2.6	1.7	1.3	1.0
HEU 50 yr Shell	18.4	9.2	6.1	4.6	3.7
HEU 50 yr Solid	5.4	2.7	1.8	1.3	1.1
WGPu 22yr Shell	2.3	1.1	0.76	0.57	0.46
WGPu 22yr Solid	2.7	1.3	0.89	0.67	0.53

Table 4.10: In-Field detector counts for 60 cm long 2.54 cm radius CsI cylindrical detector for the 50 cm source-detector distance, 5 cm long, 5 cm thick Tungsten collimator. Adjoint response tallied for the 1.001 MeV line over 34.68 degree angular FOV with a 69.2 cm linear FOV.

Source Type	1 mph	2 mph	3 mph	4 mph	5 mph
HEU 1yr Shell	42.3	21.1	14.1	10.6	8.4
HEU 1 yr Solid	12.0	6.0	4.01	3.0	2.4
HEU 50 yr Shell	42.4	21.2	14.1	10.6	8.5
HEU 50 yr Solid	12.4	6.2	4.14	3.1	2.4
WGPu 22yr Shell	5.3	2.6	1.8	1.3	1.1
WGPu 22yr Solid	6.2	3.1	2.0	1.5	1.2

Table 4.11: In-Field detector counts for 60 cm long 2.54 cm radius CsI cylindrical detector for the 50 cm source-detector distance, 15 cm long, 5 cm thick Tungsten collimator. Adjoint response tallied for the 1.001 MeV line over 12.989 degree angular FOV with a 23.06 cm linear FOV.

Source Type	1 mph	2 mph	3 mph	4 mph	5 mph
HEU 1yr Shell	14.4	7.2	4.8	3.6	2.8
HEU 1 yr Solid	4.1	2.0	1.4	1.0	0.82
HEU 50 yr Shell	14.4	7.2	4.8	3.6	2.8
HEU 50 yr Solid	4.2	2.1	1.4	1.1	0.84
WGPu 22yr Shell	1.8	0.90	0.60	0.45	0.36
WGPu 22yr Solid	2.1	1.0	0.69	0.52	0.41

These findings show that the limiting case for HEU detection is the solid configuration due to the inherent self-shielding observed, which lowers the observed counts at the detector. Furthermore, a speed of 2 miles per hour with a 5 cm collimator should be sufficient to handle most cases, although in regions where larger background counts exist, the detector platform can be slowed to 1 mph and the detector collimation can correspondingly be increased. The 1.001 MeV line used as an indicator for the

WGPu is not as strong (and in general decreases with increasing energy), so an alternate gamma energy range, such as the 767-954 keV or surrounding the 740 keV line may also be considered.

Note that there is a tradeoff between increasing the speed of the platform (therefore reducing exposure time) and decreased counts. The same tradeoff exists as more collimation length is added (although as mentioned previously this reduces Out-of-Field signal). Since the alteration of any one parameter changes all other variables, an optimal case does not necessarily exist for all configurations and background cases, suggesting an evaluation of background should baseline the process for thresholds, as discussed in earlier sections. However, a general guideline of using a 30 cm source-detector distance, 10 cm collimation thickness, with at least a 5 cm thick collimator operating at 2 mph with time-gating may offer the most flexible approach to begin in an untested environment for this particular application.

A particular set of "Rules-of-Thumb" can be observed during operational phase of the MPVS:

- If the count rate is too low within the detector…
    - Reduce source-detector distance.
    - Decrease collimation length.
        - Ensure that linear FOV > inter-source spacing.
    - Slow detector train down by 1 mph increments.
        - Note that this may drive the OOF signal beyond acceptable limits.
    - If the above fails, chain multiple detectors together and implement time gating among detectors.
        - As an alternative, couple a CsI and an NaI detector in a Phoswitch configuration as this is optimal for low-count rate, high background sources [22].

While this design is adequate, a particular disadvantage of the cylindrical CsI gamma detector design is that it is too elongated along the vertical axis, presenting problems for light collection along the length of the detector when a photomultiplier tube is attached to it. Furthermore, high energy gammas (particularly the 1.001 MeV line) respond better to thicker geometries, as they present a greater thickness for eventual absorption. Therefore, thick slabs of CsI should be better overall than the cylinders prescribed. An analysis of this is shown in Section 4.13.

4.13. FOV Response for Parallelepiped CsI Detector

To mitigate better absorption of gamma rays, "slab" CsI detectors were also considered. Calculations similar to those carried out for cylindrical detectors were also performed for two new slab detector designs; recall that in Section 2.3, the average efficiency of cylindrical vs. slab detectors as a function of energy group was presented (Figure 2.4 and Figure 2.5), and we note that the average efficiency across all energies is higher and more uniform than for the slab design, assuming similar photomultiplier performance between the two is available, which is a reasonable assumption.

The variation of counts for the source types and vehicle speed are provided in Table 4.12 and Table 4.13 using a 30 cm source to detector distance for the $2 \times 4 \times 8$ inch^3 CsI detector (Table 4.12) and the $4 \times 4 \times 8$ inch^3 CsI detector (Table 4.13). An analysis of the revised detectors compared to the original cylindrical design yielded comparable performance; however the $4 \times 4 \times 8$ inch^3 CsI detector has superior performance compared to the $2 \times 4 \times 8$ inch^3 detector. In particular, a count rate increase of roughly 25% is observed for the $4 \times 4 \times 8$ inch^3 CsI detector compared to the $2 \times 4 \times 8$ inch^3

detector, since the additional 2 inches of CsI enable high energy photons to be captured within the scintillating material. Again, results here indicate the HEU solid configurations are more difficult to detect, and multiple detector trains may be needed depending upon the background.

Table 4.12: Whole-Field detector counts for 2 × 4 × 8 inch^3 CsI detector for the 30 cm source-detector distance with a 10 cm long, 1 cm thick tungsten collimator. Adjoint response tallied for the 1.001 MeV line over 30.6255 degree angular FOV and a linear FOV of 35.52 cm.

Source Type	1 mph	2 mph	3 mph	4 mph	5 mph
HEU 1yr Shell	22.6	11.3	7.5	5.6	4.5
HEU 1 yr Solid	6.4	3.2	2.1	1.6	1.3
HEU 50 yr Shell	22.7	11.3	7.5	5.7	4.5
HEU 50 yr Solid	6.6	3.3	2.2	1.6	1.3
WGPu 22yr Shell	45.3	22.6	15.1	11.3	9.1
WGPu 22yr Solid	1.0	0.52	0.35	0.26	0.21

Table 4.13: Whole-Field detector counts for 4 × 4 × 8 inch^3 CsI detector for the 30 cm source-detector distance with a 10 cm long, 1 cm thick tungsten collimator. Adjoint response tallied for the 1.001 MeV line over 30.6255 degree angular FOV and a linear FOV of 35.52 cm.

Source Type	1 mph	2 mph	3 mph	4 mph	5 mph
HEU 1yr Shell	30.9	15.4	10.3	7.7	6.2
HEU 1 yr Solid	8.8	4.4	2.9	2.2	1.7
HEU 50 yr Shell	31.0	15.5	10.3	7.7	6.2
HEU 50 yr Solid	9.1	4.5	3.0	2.3	1.8
WGPu 22yr Shell	61.8	30.9	20.6	15.5	12.4
WGPu 22yr Solid	1.4	0.72	0.48	0.36	0.28

These findings show that the extra two inches of CsI thickness provides significantly better results that are on-par with the previous cylindrical detector design. The additional two inches provides a larger volume for photons to absorb within the detector and be

picked up by the PMT. As with the cylindrical detector, an optimal speed of 2 miles per hour is considered adequate. Also as before, different plutonium gamma lines can also be considered if insufficient counts are observed for the plutonium gamma line at 1.001 MeV.

4.14. Comparison of Photopeak Driven Results with Pulse Height Analysis

In the laboratory setting, by utilizing a photopeak software such as SmartID™ developed by Sjoden and Yi (2013) [44] it is possible to isolate gamma photopeaks from background radiation through a series of a scoring tallies. Using this methodology it is possible to get results similar to Figure 4.13.

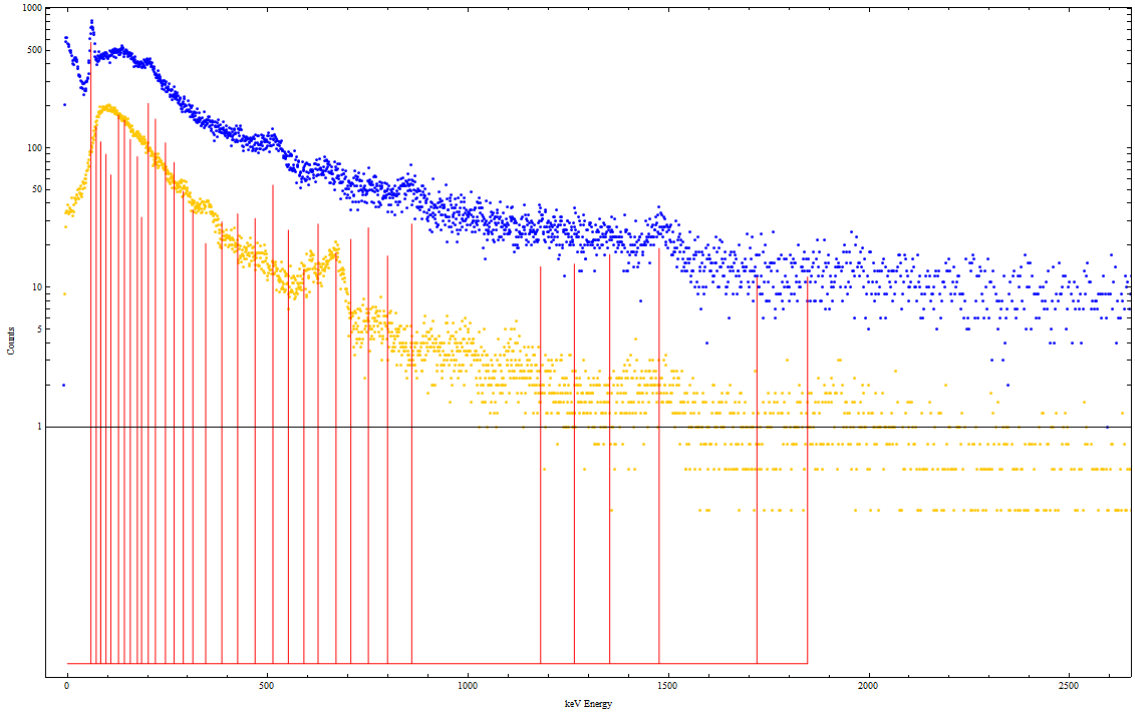

Figure 4.13: Gross (top) ^{239}Pu (6% WGPu,1 Ci PuBe) source, BG (bottom), SmartID attributed photopeak lines (Figure republished from Yi et al.) [44].

Previous analysis until now calculated reaction rates based on the macroscopic absorption cross section (the Photoelectric effect) within the scintillating CsI material. In order to have a more microscopically realistic analysis of reaction rates, including contributions from Compton scattering and pair production was required. A pulse height tally added to the one source collimated case was used to compare the forward volumetric reaction rate (units of photons/second) to the pulse binning in MCNP (units of pulses). Since the absolute efficiency of Sodium Iodide (NaI) detectors is reported [45] as 1.2×10^{-3} and the relative efficiencies of CsI(Tl) (45%) and CsI(Na) (80%) to NaI are reported in the literature [22], the results are scaled by these efficiencies to simulate a detector gain. This comparison is shown in Figure 4.14. An alternate view of this data comparing MCNP absorption tallies is shown in Figure 4.15.

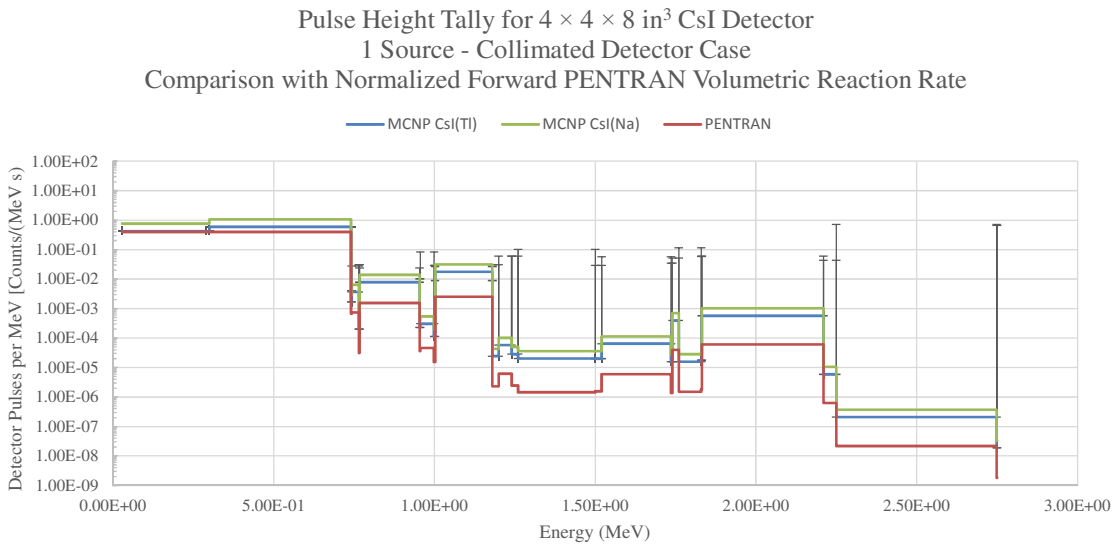

Figure 4.14: Normalized PENTRAN Forward Volumetric Response Rates and MCNP Pulse Height Tallies Corrected with Detector Efficiency.

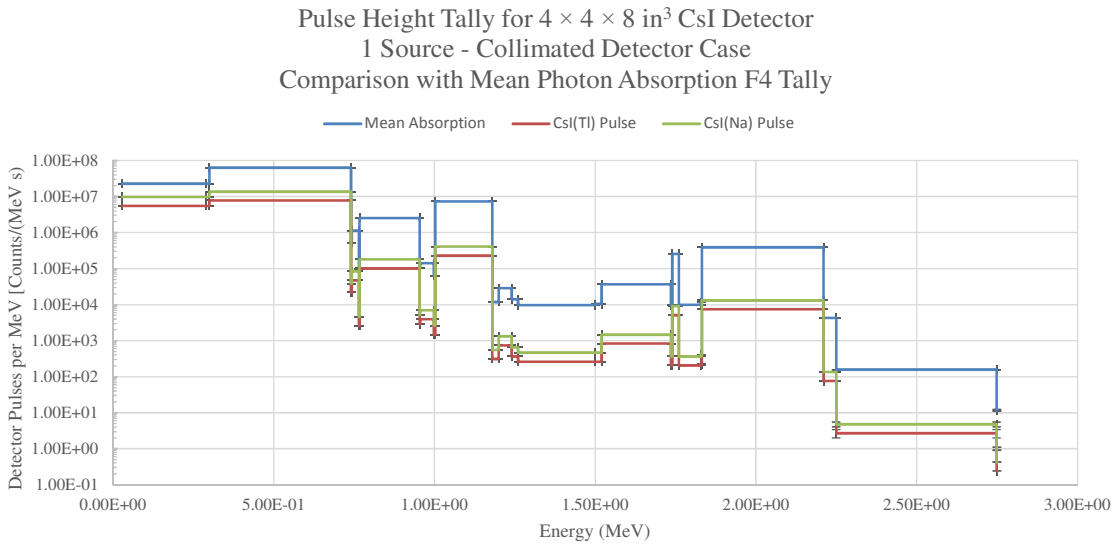

Figure 4.15: Absolute Mean Photon Absorption MCNP Tally Comparison with MCNP Pulse Height Tallies Corrected with Detector Efficiency.

These results show that effects from Compton are fairly significant, dropping the counts received by roughly an order of magnitude. A percent difference plot of Figure 4.15 is shown in Figure 4.16. The average percent difference between the efficiency-corrected CsI detector for both cases compared to purely absorptive CsI over all energy groups was 185.98% and 176.38% respectively.

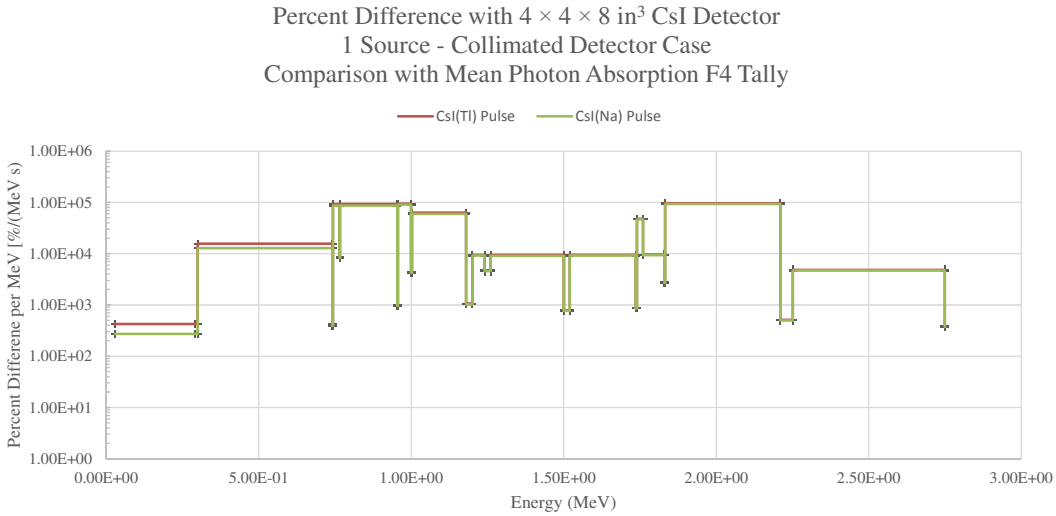

Figure 4.16: Percent Difference in CsI(Tl) and CsI(Na) to the Purely Absorbing Case.

It is possible to take these results and determine the counts that result from a moving detector with a FOV defined by a 30 cm source-detector distance and a 10 cm long collimator for a 1 year aged HEU spherical shell source. These results are shown in Table 4.14.

Table 4.14: Whole-Field detector counts for 4 × 4 × 8 inch^3 CsI detector for the 30 cm source-detector distance with a 10 cm long, 5 cm thick tungsten collimator for a 1 year aged HEU spherical shell source. Pulse Height Tallied on the 1.001 MeV line over 30.6255 degree angular FOV and a linear FOV of 35.52 cm.

Source Type	1 mph	2 mph	3 mph	4 mph	5 mph
PENTRAN Adj RR	30.9	15.4	10.3	7.7	6.2
CsI(Tl) MCNP Pulse	24.9	12.5	8.3	6.2	4.9
CsI(Na) MCNP Pulse	44.3	22.1	14.7	11.9	8.8

The total integrated counts in the FOV are somewhat comparable between the two sets. However, the 2σ uncertainty in the pulse height tally was significant in the 1.001 MeV energy bin (8.8×10^{-3}) compared to the PENTRAN tolerance (1.0×10^{-5}) defined globally over all fine meshes. This uncertainty in the MCNP does not translate well throughout the process described in Section 4.2, so the particular results in should be considered approximate in the absence of a detailed error propagation analysis.

4.15. Number of Detectors Required at Given Speeds

Since the analysis presented in Section 4.14 provides the minimum required counts to be statistically significant, it is possible to combine these thresholds on a per-group basis with the integrated count rate from the adjoint detector response in Section 4.13 to determine the minimum number of detectors required at a given energy range. Since the angular and linear FOV are coupled by geometry, the exposed time the detector faces the

source is variable. However, for simplicity, the minimum detectable threshold was set to 0.5 seconds. As we shall see, this figure is not too far off from actual calculated FOV times based on calculations performed in Section 4.2.

Since one of the limiting cases is the solid geometry, emphasis in this section was placed on analyzing the 1 year HEU solid geometry with the $4 \times 4 \times 8$ in^3 CsI detector with 30 cm long, 1 cm and 5 cm thick collimator. It is important to note that these particular results are integrated counts over the whole field of the source FOV plane for a single source, the influence of more sources is covered in Section 5.4. The integrated counts for each speed from the adjoint reaction rate scenarios are shown in Table 4.15 and Table 4.16.

The number of gamma blocks required is based on Eq. 4.11, where $\boldsymbol{N_D}$ is the Real Activity Threshold count, $\boldsymbol{L_c}$ is the Currie limit decision threshold, $\dot{\boldsymbol{D}}$ is the SNM count rate (aliased from the reaction rate), and $\boldsymbol{T}$ is the counting time which is determined as a function of detector speed and linear FOV. The zero mile per hour case shown in the tables below are calculated based on the 1 mph time-gate value.

$$n_{\gamma,blocks} = \frac{(N_D - L_c)}{\dot{D}T} \qquad \text{Eq. 4.11}$$

The tables below use a relative color reference scale to visually highlight the predominant gamma lines based on their relative strength. The color scale for the integrated count rates show the lowest integrated counts with red going towards the highest integrated counts in green. The color scale for the minimum number of detectors is inverted, with the smallest number of detectors colored red with the gradient extending toward the largest number of detectors in red.

Table 4.15: Integrated Count Rate (Photons) for a 1 year HEU Solid Source from Adjoint Reaction Rate Calculation. This particular case is for a 4 × 4 × 8 in^3 CsI detector with a 10 cm long, 1 cm thick tungsten collimator. Coloring is based on a relative scale with green signifying the highest counts and red for the lowest counts.

Group	Upper Energy (MeV)	Lower Energy (MeV)	0 mph	1 mph	2 mph	3 mph	4 mph	5 mph
1	2.750	2.749	0.003	0.002	0.001	0.001	0.001	0.000
2	2.749	2.250	0.003	0.002	0.001	0.001	0.001	0.000
3	2.250	2.210	0.002	0.002	0.001	0.001	0.000	0.000
4	2.210	1.832	0.652	0.558	0.279	0.186	0.139	0.112
5	1.832	1.830	0.320	0.274	0.137	0.091	0.068	0.055
6	1.830	1.760	0.330	0.282	0.141	0.094	0.070	0.056
7	1.760	1.740	0.076	0.065	0.033	0.022	0.016	0.013
8	1.740	1.736	0.402	0.344	0.172	0.115	0.086	0.069
9	1.736	1.520	0.762	0.652	0.326	0.217	0.163	0.130
10	1.520	1.500	0.279	0.239	0.119	0.080	0.060	0.048
11	1.500	1.260	0.835	0.714	0.357	0.238	0.179	0.143
12	1.260	1.240	0.061	0.053	0.026	0.018	0.013	0.011
13	1.240	1.200	0.190	0.162	0.081	0.054	0.041	0.032
14	1.200	1.180	0.224	0.192	0.096	0.064	0.048	0.038
15	1.180	1.002	0.708	0.605	0.303	0.202	0.151	0.121
16	1.002	0.999	10.274	8.789	4.394	2.930	2.197	1.758
17	0.999	0.956	0.925	0.792	0.396	0.264	0.198	0.158
18	0.956	0.954	0.120	0.103	0.051	0.034	0.026	0.021
19	0.954	0.767	7.556	6.464	3.232	2.155	1.616	1.293
20	0.767	0.765	2.803	2.398	1.199	0.799	0.599	0.480
21	0.765	0.743	0.662	0.566	0.283	0.189	0.142	0.113
22	0.743	0.741	1.294	1.107	0.553	0.369	0.277	0.221
23	0.741	0.300	116.102	99.324	44.662	33.108	24.831	19.865
24	0.300	0.000	15101.500	12919.200	6459.580	4306.380	3229.790	2583.830

Table 4.16: Integrated Count Rate (Photons) for a 1 year HEU Solid Source from Adjoint Reaction Rate Calculation. This particular case is for a 4 × 4 × 8 in^3 CsI detector with a 10 cm long, 5 cm thick tungsten collimator. Coloring is based on a relative scale with green signifying the highest counts and red for the lowest counts.

Group	Upper Energy (MeV)	Lower Energy (MeV)	0 mph	1 mph	2 mph	3 mph	4 mph	5 mph
1	2.750	2.749	0.003	0.003	0.001	0.001	0.001	0.001
2	2.749	2.250	0.003	0.003	0.001	0.001	0.001	0.001
3	2.250	2.210	0.003	0.002	0.001	0.001	0.001	0.000
4	2.210	1.832	0.743	0.636	0.318	0.212	0.159	0.127
5	1.832	1.830	0.364	0.312	0.156	0.104	0.078	0.062
6	1.830	1.760	0.375	0.321	0.160	0.107	0.080	0.064
7	1.760	1.740	0.087	0.074	0.037	0.025	0.019	0.015
8	1.740	1.736	0.458	0.392	0.196	0.131	0.098	0.078
9	1.736	1.520	0.865	0.740	0.370	0.247	0.185	0.148
10	1.520	1.500	0.317	0.271	0.135	0.090	0.068	0.054
11	1.500	1.260	0.946	0.809	0.404	0.270	0.202	0.162
12	1.260	1.240	0.069	0.059	0.030	0.020	0.015	0.012
13	1.240	1.200	0.214	0.183	0.092	0.061	0.046	0.037
14	1.200	1.180	0.253	0.217	0.108	0.072	0.054	0.043
15	1.180	1.002	0.798	0.682	0.341	0.227	0.171	0.136
16	1.002	0.999	11.564	9.893	4.946	3.298	2.473	1.979
17	0.999	0.956	1.041	0.891	0.445	0.297	0.223	0.178
18	0.956	0.954	0.135	0.116	0.058	0.039	0.029	0.023
19	0.954	0.767	8.486	7.260	3.630	2.420	1.815	1.452
20	0.767	0.765	3.142	2.688	1.344	0.896	0.672	0.538
21	0.765	0.743	0.742	0.635	0.317	0.212	0.159	0.127
22	0.743	0.741	1.450	1.240	0.620	0.413	0.310	0.248
23	0.741	0.300	129.556	110.834	55.417	36.945	27.709	22.167
24	0.300	0.000	16716.600	14300.800	7150.420	4766.950	3575.210	2860.170

By applying Eq. 4.11 we get the minimum number of banked CsI detectors required to detect SNM while taking into account the group-dependent background rate. This is shown in Table 4.17 and Table 4.18.

Table 4.17: Number of Banked Detectors required for a 1 year HEU Solid Source from Adjoint Reaction Rate Calculation. This particular case is for a 4 × 4 × 8 in^3 CsI detector with a 10 cm long, 1 cm thick tungsten collimator. Coloring is based on a relative scale with green signifying the lowest number of detectors required and red for the highest number of detectors required.

Group	Upper Energy (MeV)	Lower Energy (MeV)	0 mph	1 mph	2 mph	3 mph	4 mph	5 mph
1	2.750	2.749	17.760	12.133	48.533	72.800	97.067	121.333
2	2.749	2.250	3971.852	2713.511	10854.044	16281.067	21708.144	27135.179
3	2.250	2.210	1498.668	1023.868	4095.478	6143.218	8190.978	10238.722
4	2.210	1.832	22.465	15.348	61.392	92.088	122.784	153.481
5	1.832	1.830	1.642	1.122	4.487	6.730	8.973	11.217
6	1.830	1.760	27.080	18.501	74.003	111.004	148.006	185.007
7	1.760	1.740	76.579	52.318	209.270	313.905	418.541	523.176
8	1.740	1.736	8.257	5.641	22.565	33.848	45.131	56.414
9	1.736	1.520	25.061	17.121	68.485	102.727	136.970	171.212
10	1.520	1.500	23.505	16.058	64.233	96.349	128.465	160.582
11	1.500	1.260	31.247	21.348	85.390	128.085	170.781	213.476
12	1.260	1.240	127.851	87.346	349.383	524.074	698.768	873.459
13	1.240	1.200	64.233	43.883	175.533	263.300	351.068	438.834
14	1.200	1.180	39.107	26.717	106.870	160.304	213.740	267.175
15	1.180	1.002	43.858	29.963	119.852	179.779	239.706	299.632
16	1.002	0.999	0.427	0.292	1.168	1.752	2.336	2.920
17	0.999	0.956	18.936	12.937	51.746	77.619	103.493	129.366
18	0.956	0.954	44.785	30.597	122.386	183.579	244.772	305.965
19	0.954	0.767	6.150	4.202	16.807	25.211	33.615	42.019
20	0.767	0.765	2.587	1.767	7.070	10.605	14.140	17.675
21	0.765	0.743	32.386	22.126	88.502	132.754	177.005	221.257
22	0.743	0.741	4.276	2.922	11.686	17.529	23.373	29.216
23	0.741	0.300	2.268	1.549	6.890	10.336	13.781	17.226
24	0.300	0.000	0.000	0.000	0.000	0.000	0.000	0.000

Table 4.18: Number of Banked Detectors required for a 1 year HEU Solid Source from Adjoint Reaction Rate Calculation. This particular case is for a 4 × 4 × 8 in^3 CsI detector with a 10 cm long, 5 cm thick tungsten collimator. Coloring is based on a relative scale with green signifying the lowest number of detectors required and red for the highest number of detectors required.

Group	Upper Energy (MeV)	Lower Energy (MeV)	0 mph	1 mph	2 mph	3 mph	4 mph	5 mph
1	2.750	2.749	15.557	10.628	42.512	63.769	85.025	106.281
2	2.749	2.250	3479.510	2377.155	9508.582	14262.873	19017.212	23771.515
3	2.250	2.210	1313.687	897.494	3589.975	5384.963	7179.968	8974.960
4	2.210	1.832	19.708	13.465	53.858	80.787	107.716	134.646
5	1.832	1.830	1.442	0.985	3.941	5.912	7.882	9.853
6	1.830	1.760	23.793	16.255	65.021	97.532	130.043	162.553
7	1.760	1.740	67.313	45.987	183.948	275.923	367.898	459.872
8	1.740	1.736	7.259	4.959	19.838	29.756	39.675	49.594
9	1.736	1.520	22.058	15.070	60.279	90.419	120.559	150.699
10	1.520	1.500	20.712	14.150	56.601	84.901	113.201	141.502
11	1.500	1.260	27.588	18.848	75.391	113.086	150.782	188.477
12	1.260	1.240	113.112	77.277	309.106	463.659	618.214	772.767
13	1.240	1.200	56.858	38.845	155.378	233.067	310.757	388.446
14	1.200	1.180	34.632	23.660	94.641	141.961	189.282	236.603
15	1.180	1.002	38.902	26.578	106.311	159.466	212.622	265.777
16	1.002	0.999	0.380	0.259	1.038	1.556	2.075	2.594
17	0.999	0.956	16.829	11.497	45.989	68.984	91.979	114.974
18	0.956	0.954	39.818	27.203	108.812	163.218	217.624	272.030
19	0.954	0.767	5.476	3.741	14.965	22.448	29.930	37.413
20	0.767	0.765	2.307	1.576	6.305	9.458	12.611	15.763
21	0.765	0.743	28.889	19.737	78.946	118.420	157.893	197.366
22	0.743	0.741	3.815	2.607	10.426	15.639	20.853	26.066
23	0.741	0.300	2.032	1.388	5.553	8.330	11.106	13.883
24	0.300	0.000	0.000	0.000	0.000	0.000	0.000	0.000

These results show that for the limiting case of 1 year HEU solid sources, one set of banked dual gamma blocks (two adjacent 4 × 4 × 8 in^3 CsI detectors) is sufficient for the 1.001 MeV gamma line at 2 mph, and this validates previous results of 2 mph being an optimal speed in most circumstances. Multiple detectors are required for the highest energy bins (generally past 2.2 MeV).

An interesting note is compared to the MPVS, the sister platform T-SADS gamma analysis performed by Edgar et al. (2013) [46] shows that multiple (at least 6-10) detectors are required for the 1.001 MeV line to be above statistical significance for

vehicles traveling 30 mph relative to the roadside detector. Since the MPVS is moving at a much slower speed, the number of detectors is somewhat smaller, allowing for a single baggage tug to be able to pull in most cases a single banked detector (although the baggage tug should be capable of pulling upwards of around 10 detectors, see Section 6.2.

The integrated count rates shown in the previous tables were then subjected to the gamma ratio technique discussed in previous sections. Two ratios between different gamma peaks were then calculated: Ratio 1, shown in Eq. 4.12 which covers the range (830-1060 keV)/(741-3000 keV), and Ratio 2, shown in Eq. 4.13 which covers the range (830-1060 keV)/(1060-3000 keV).

$$\frac{\left(0.5\,N_{15,D}+\sum_{16}^{18}N_D+0.5\,N_{19,D}\right)-\left(0.5\,L_{15,C}+\sum_{16}^{18}L_C+0.5\,L_{19,C}\right)}{\sum_{1}^{22}\dot{D}\,T} \qquad \text{Eq. 4.12}$$

$$\frac{\left(0.5\,N_{15,D}+\sum_{16}^{18}N_D+0.5\,N_{19,D}\right)-\left(0.5\,L_{15,C}+\sum_{16}^{18}L_C+0.5\,L_{19,C}\right)}{\left(0.5\,\dot{D}_{15}+\sum_{1}^{14}\dot{D}\right)T} \qquad \text{Eq. 4.13}$$

These results are summarized in Table 4.19. Ratio 2 is superior in that fewer number of detectors are required, and the energy bands are structured such that it is invariant on detector speed unlike Ratio 1. If the first ratio is used, a nominal 1 mph speed is used while the second ratio can be operated greater than this speed.

Table 4.19: Minimum number of detectors required as a function of detector speed using the gamma ratio technique along with time-gating. Note that the results are applicable only for the energy ranges for each respective ratio.

		Speed (mph)					
Ratio Comparison	Energy Range (keV)	0	1	2	3	4	5
Ratio 1	(767-1180)/(741-2750)	5.376	1.836	7.346	16.528	29.382	45.910
Ratio 2	(767-1180)/(1180-2750)	0.136	0.136	0.136	0.136	0.136	0.136

4.16. Conclusions

The increased performance in the 1.001 MeV gamma line of the $4 \times 4 \times 8$ in^3 parallelepiped CsI detector relative to both the $2 \times 4 \times 8$ in^3 parallelepiped detector and the cylindrical 1 inch diameter detector. Assuming an isotropic source distribution the volumetric forward and adjoint reaction rate totals match up within 2 percent difference of each other. Modeling a full surface source shows fairly good agreement between the adjoint surface and the adjoint volume cases (being within a factor of 4 different which is explained by the difference in current and flux), and good agreement between adjoint volume and forward volume comparisons. The reaction rates were also compared against a theoretical upper bound to frame the reaction rates with a reasonable count rate. A brief comparison with MCNP Pulse Height tallies was performed and compared with integrated reaction rates from PENTRAN. The minimum number of detectors for a given speed and energy were also tabulated, and showed that a single detector should be sufficient for most applications below 2.2 MeV.

The results from the gamma ratio analysis indicate that 2 mph is more than adequate with the second ratio, and that the second ratio allows fairly high speeds to be attained.

Chapter 5: Effect of Moving Detector and Multiple Sources

5.1. Objective

The purpose of this chapter is to assess the impact of multiple sources on the optimized detector configuration ($4 \times 4 \times 8$ in^3 CsI detector with 10 cm long and 5 cm thick tungsten collimator) in both PENTRAN and MCNP.

5.2. Monte Carlo Models

A series of Monte Carlo models showing the optimized gamma block and the T-SADS neutron block, as shown in Figure 5.1. Instead of using the Source Book data to replicate a surface source (i.e. certain models by Paul [12] and Chin) this particular configuration uses the "Full Source" configuration where the detector and source(s) are modeled with the full SNM canister. As in previous comparison analyses, the 1 year HEU shell source was picked as a baseline configuration, with a source-detector distance of 30 cm and inter-source spacing of 1 meter.

Three classes of Monte Carlo models were created: collimated and uncollimated one source models, collimated and uncollimated three source models, and a "moving collimated detector" set of models with three sources. This latter part is "moving" in the sense that multiple forward continuous energy steady-state Monte Carlo calculations were performed with the detector in various positions (ranging from -100 cm to 100 cm with the gamma block in front of the center SNM source canister).

Tallies were evaluated at several positions in the model: Mean Absorption in the Detector (F4 in the CsI volume), Current Tally at Detector Face (F1 at the CsI detector plane facing the source), Pulse-Height Tally in the Detector (F8), Flux Tally at In-Field-

Plane on the Outer Source Box (F2), Flux Tally at the Mid-Field Plane (F2), and Flux Tally at the OOF Plane (F2). Since the outer source box is not near any highly scattering surfaces and the probability of backscatter from the detector is considered small, using flux tallies should be adequate for purposes of this analysis.

The spherical HEU shells were modeled as sources using the FCEL notation to describe multiple sources for the three source case with a single source definition card, and energy binning was identical to the 24 group mentioned in Table 3.2. The tally multiplier for the one source model was the total number of photons in a single source while the tally multiplier for the three source was three times the total number of photons in a single source. The source histogram used was the normalized distribution provided directly from ORIGEN-ARP/SCALE6 for a HEU source [3, 30].

For each of these models 1.0×10^{12} (1 trillion) histories were sampled to ensure decent statistics on each of the tallies. However one significant limitation with any Monte Carlo method is that convergence in some groups is extremely difficult even with 1.0×10^{12} histories. As we shall see in the following sections, the 2σ standard deviation is considerable in a few of the highest energy groups from lack of interaction due to streaming in optically transparent materials present (such as air) in the model. For this reason it was considered important to benchmark at least one of these cases (the one source collimated case) with PENTRAN as the tolerances in deterministic models tend to be fairly flat across the entire energy phase space.

The random generator selected in MCNP was the L'Ecuyer 63 bit random number generator #1 with a periodicity of 9.2×10^{18} random numbers [21]. The seed was consistent across all cases; for the "moving detector" case the different location of the

detector should sufficiently randomize the surface and absorption tallies due to different directionalities of each of the sampled histories.

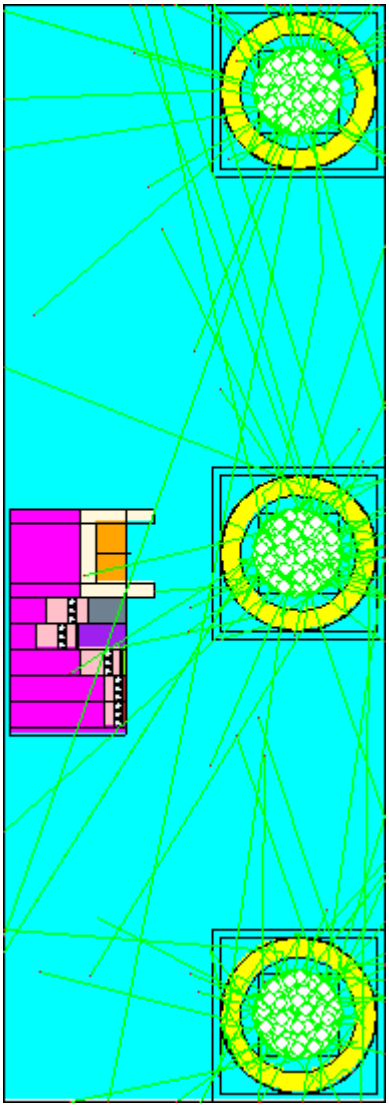

Figure 5.1: MPVS Gamma and Neutron Blocks Simulated in MCNP with 3 HEU Spherical Shell Sources. There were 10,000 Histories sampled in this illustrative example.

5.3. PENTRAN Deterministic Transport Models

The 30 cm source-detector, $4 \times 4 \times 8$ in^3 CsI detector with 10 cm long, 5 cm thick tungsten collimator was selected as a deterministic comparison to the equivalent MCNP case, however the source used was a surface source instead of modeling the full SNM canister. Symmetry was employed along the bottom –Y axis as in previous models to leverage computational resources and higher quadrature.

A few of the advanced features of PENTRAN were used to simulate the spherical shell within the SNM canister as a surface source in PENTRAN: Fine mesh spatial probability distributions were utilized from earlier in this report (see

Figure 3.18) to establish a half-source distribution; Angular dependence was explicitly specified on a per-octant basis for S_{42} quadrature to conform to a source pointing in the –X direction. As there are three surface sources specified across three coarse meshes of the model, special precautions needed to be made to ensure a correct probability density function of the integral source magnitude across three sources. The integral source magnitude was set to a total source magnitude of 1.29621×10^7 photons that are then distributed over three sources and normalized by the relative surface area (to the total surface area of the half-source plane) of the In-Field source, Mid-Field source, and OOF source. This is because the smag variable in PENTRAN implicitly defines a rough probability density function which can then be refined on a fine mesh basis with the spacpf variable. These source magnitudes are shown in Table 5.1.

Table 5.1: Integral Source Magnitude for each PENTRAN Surface Source. Note that the sources are defined on Coarse Mesh 4, 12, and 20 and correspond to In-Field, Mid-Field, and OOF sources.

	YZ Surface Area (cm^2)	Fraction of Total	Fractional Source Magnitude (photons/sec)
Coarse Mesh 4	784.352	0.33866667	4.38983E+06
Coarse Mesh 12	450.848	0.19466667	2.52329E+06
Coarse Mesh 20	1080.8	0.46666667	6.04898E+06
Total	2316	1	1.29621E+07

The fine mesh spatial probability density function provided by the linearly interpolated line from the YZ space-angle probability distribution in Figure 3.18b was computed for each of the 20 × 20 meshes (400 fine meshes total per source coarse mesh). Since this result added up to greater than 1 per source, the distributions were then normalized to unity for each surface source. Since this would not adequately represent the physics of a single surface source distributed across three surface sources, this distribution is then *renormalized* such that the total sum of each surface source would add up to 1 and weighted by each source's respective normalized sums.

The omegap variable was defined to provide a direction defined along the –X axis projecting towards the detector for S_{42} quadrature for all three sources. Combined with the integral source magnitude probability density function, this representation of the surface source accurately models the spherical shell distributed amongst a steel cylindrical container as a single planar source.

5.4. Detector Response Comparison – One Source vs. Three Sources

An interesting subject that closely ties into collimator design is to assess the detector response for a single source compared to three sources. MCNP simulations at the 0 cm detector-source Y plane (gamma detector centered on the source) were performed with one source and three source for both collimated and uncollimated models to see what percent difference, if any, exist between the cases. Comparisons to PENTRAN with the 0 cm case with a single source was also performed, and are shown in Figure 5.2.

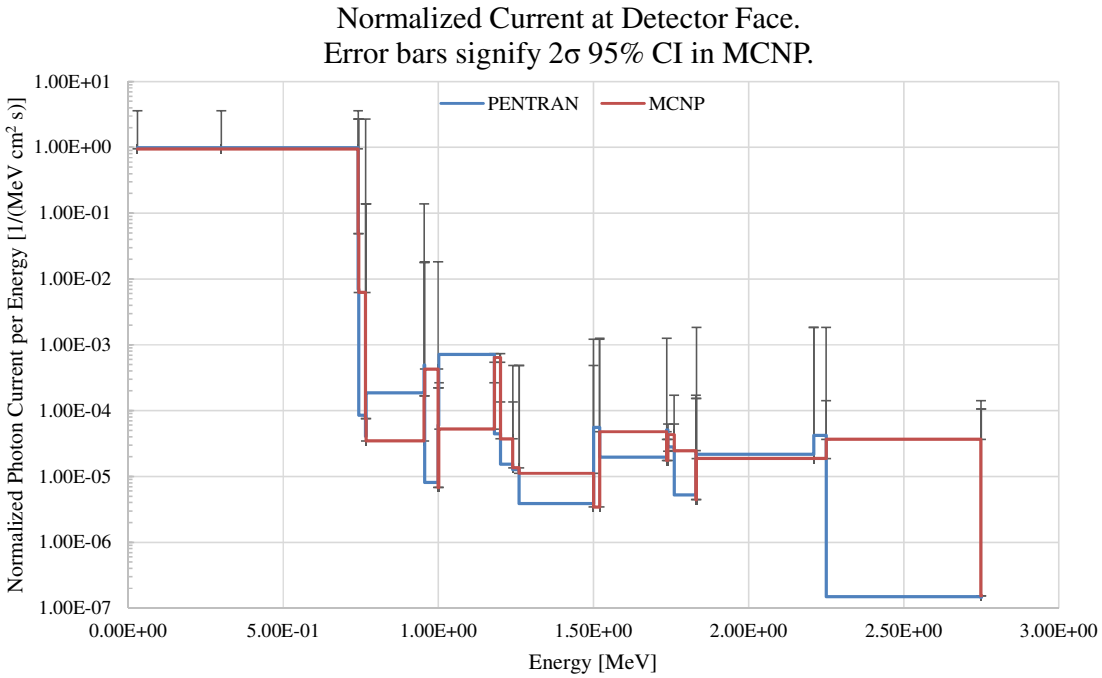

Figure 5.2: MCNP and PENTRAN 0cm Uncollided Flux Comparison for a Single Source. MCNP normalization factor: 1.2916×10^{7} photons. PENTRAN normalization factor: 4.2914×10^{6} photons.

The results from Figure 5.2 show order-of-magnitude agreement between MCNP and PENTRAN. The 2σ standard deviation[3] was still fairly significant for the MCNP run with 1.0×10^{12} histories sampled, and is very pronounced in energy groups that were either narrow (a few tens of keV different) or very high energy (greater than 2.74 MeV).

As expected, three source models would typically have higher responses in spite of the collimator (although the collimator would mitigate some of the response from OOF sources).

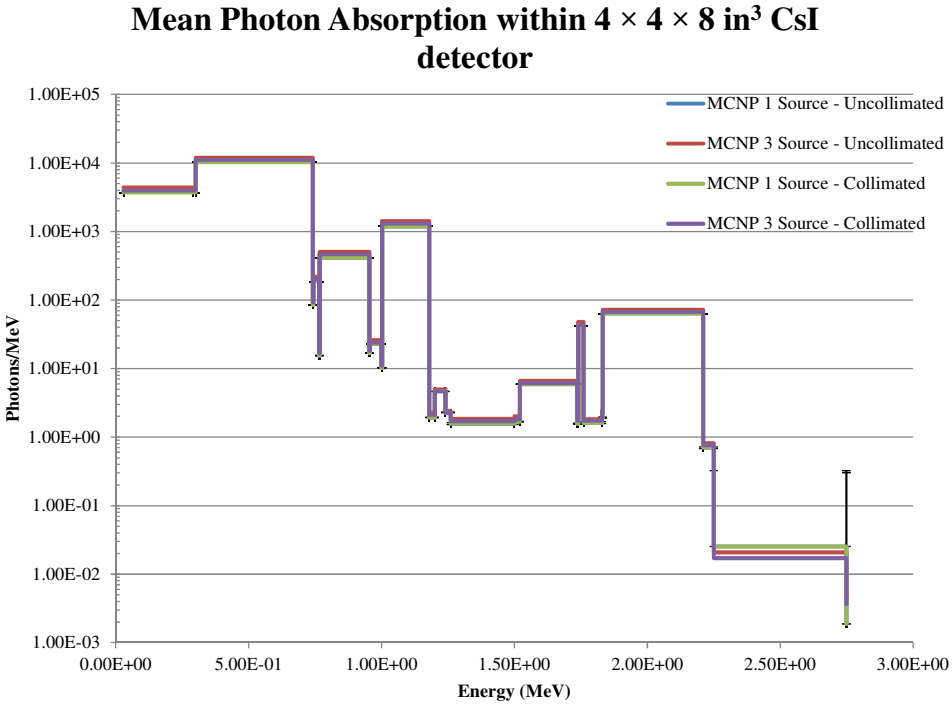

Figure 5.3: Mean Photon Absorption in 4 × 4 × 8 in³ CsI detector in MCNP for one and three sources with collimated and uncollimated detectors. Error bars shown for the one source uncollimated case, other cases have similar uncertainties[4].

---

[3] The average 2σ standard deviation for Figure 5.2 is 1.835594×10^{-1}. When the fastest two energy groups are removed, this number drops to 1.050473×10^{-1}.
[4] The average total 2σ MCNP error was 8.34653×10^{-2}, when considering everything except the fastest two groups the average total 2σ MCNP error was 3.73381×10^{-2}.

The behavior of Figure 5.3 shows that the photon absorption in general follows the energy distribution specified in normalized source leakage currents specified in Figure 3.9. While this is generally acceptable in a single source scenario, Figure 5.3 doesn't describe subtle differences when other sources are added in addition to the primary SNM canister the detector is facing. To better explain the differences it is important to look at the relative differences of these cases compared to the baseline one source with uncollimated detector, which is shown in Figure 5.4.

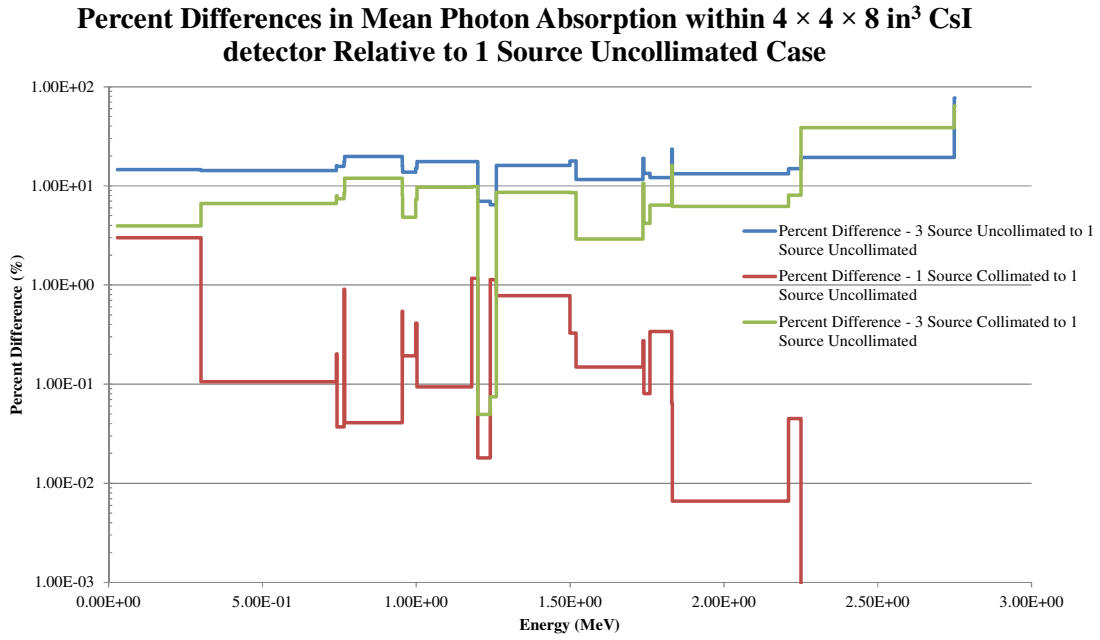

Figure 5.4: Relative Difference of Figure 5.3 compared to one source with uncollimated detector.

Figure 5.4 shows that the collimator does reduce the absorption of photons in the detector as expected (this reduction is expected to come from photons being absorbed/scattered in the collimator and considered sufficiently out of the FOV of the collimation hence a smaller percent difference), but the changes are subtle and within the same order of magnitude.

5.5. Detector Uncollided Surface Flux Comparison – Moving Detector

The uncollided photon current was calculated for the three source case in MCNP with multiple simulations with the MPVS detector configured from -100 cm to 100 cm along the Y axis of the model shown in Figure 5.1. As the detector moves across a given source and the signal is time-gated relative to the linear FOV of the collimated detector this would reveal some insight into the "spread" of the signal as it travels in-between multiple sources.

The uncollided photon current shown in Figure 5.5 shows the spectral distribution of the uncollided current as a function of energy and also as a function of detector distance from the source centerline. The maxima, as would be expected of a detector centered on the source, is consistently largest for the 0 cm case. The largest deviation are at the extrema of -100 cm and 100 cm coinciding when the detector is in-between either of the two adjacent sources. The cases in between the maxima and minima consistently are between these extreme points.

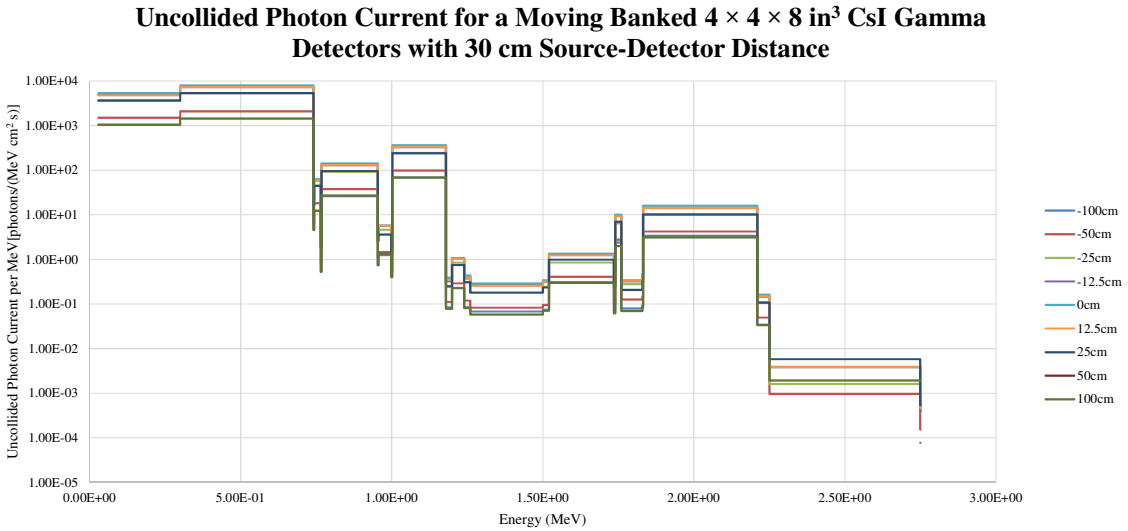

Figure 5.5: Uncollided photon current for a moving bank of two 4 × 4 × 8 in³ CsI gamma detectors.

Since Figure 5.5 tells us the spread of the signal as a function of distance and not detailed information about how much it deviates from the centerline case, Figure 5.6 addresses this by plotting relative percent difference between the centerline case and the moving detector configurations. The differences tend to be mostly flat across the energy spectrum but can deviate upwards of 140% in most groups for the -100 cm and 100 cm cases.

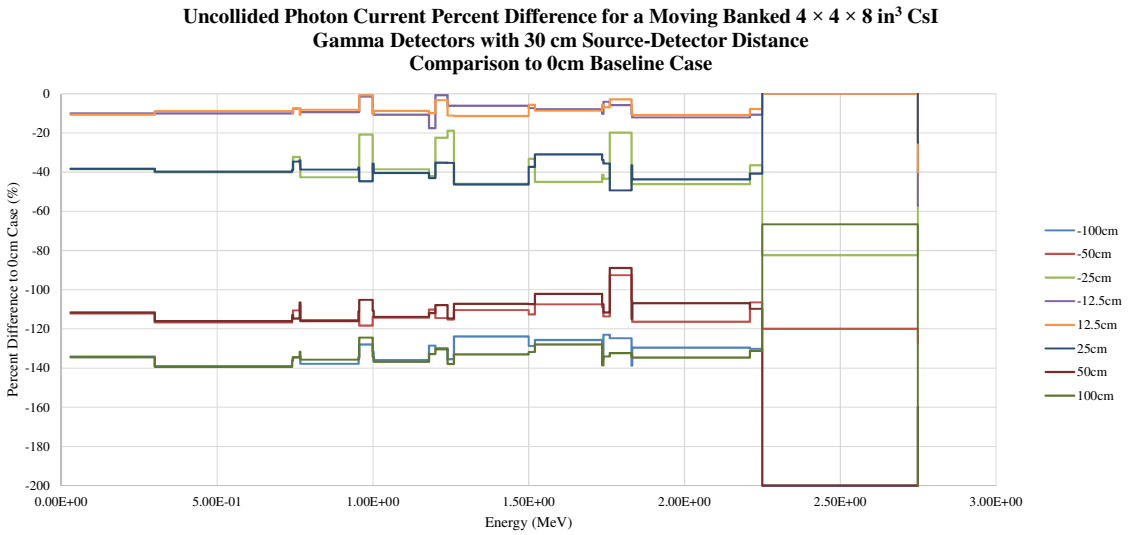

Figure 5.6: Absolute Percent Difference Relative to 0 cm Source-Centered Case.

5.6. Implications for In-Field and Out-of-Field Response

Although the geometry effects shown in Figure 5.5 and Figure 5.6 show percent differences of around roughly 140 percent on average, the currents are still within the same order of magnitude. Care must be taken to address these subtle spectral shifts and although it is possible using the patented Gamma Ratio technique by Sjoden & Maniscalco [23] in addition to matching the spectral profile to known HEU sources of spherical shell and solid configuration [38, 47], the problem of accurately identifying whether the spectral shift is due to the presence of other adjacent sources or otherwise due to mass or shape differences of the source remains non-trivial.

5.7. Conclusions

The previous sections outlined that subtle spectral magnitude shifts can occur within the detector when either the collimator isn't present or if the detector is not aligned perpendicularly from the source. A good way to mitigate these effects are to time gate the detector just as it is within the FOV of the source, however the user must take into consideration that possible discrepancies in signal magnitude may occur if the shapes and amount of mass deviate from 1 SQ quantities of SNM sources.

Chapter 6: Final Design Specifications

6.1. Description

The MPVS unit dimensions for the default configuration are shown in Table 6.1. For higher counts it is best to minimize the source-detector distance as much as possible. The "fixed" tungsten slabs are located directly adjacent to the gamma detector, while the "movable" tungsten slabs can be configured to meet the specific situations that may arise during MPVS operation. Assume an XY view (as shown in Figure 6.1 or 6.2) when referring to the plate orientation (i.e. "Back" plate is –Y, "Top & Bottom" plates refer to +Z and –Z respectively, and "Side" plates refer to –X and +X).

Table 6.1: Revised Gamma Detector and Photon Collimation Parameters

Gamma Detector Type	CsI (Thallium Activation) Scintillator
Neutron Detector Type	Helium-3 Proportional Gas Detector
Overall Unit Dimension (Neutron + Gamma Blocks)	54.32 cm × 30 cm × 30 cm
Cesium Iodide Dimensions (Single block)	10.16 cm × 10.16 cm × 20.32 cm
Helium-3 Dimensions	Radius: 1.27 cm. Height: 30 cm
Fixed Tungsten Slab Dimensions	Back Plate: 22.16 cm × 5 cm × 22.32 cm Side Plates: 5 cm × 10.16 cm × 22.32 cm Top & Bottom Plate: 22.16 cm × 5 cm × 5 cm
Movable Tungsten Slab Dimensions (Length is adjustable, but default is 10 cm)	Side Plates: 5 cm × Y cm × 22.32 cm Top & Bottom Plate: 22.16 cm × Y cm × 22.32 cm
Source-Detector Distance	30 cm – 50 cm

Both the original MPVS detector design and the revised MPVS detector design XY diagrams are shown in Figure 6.1 and Figure 6.2.

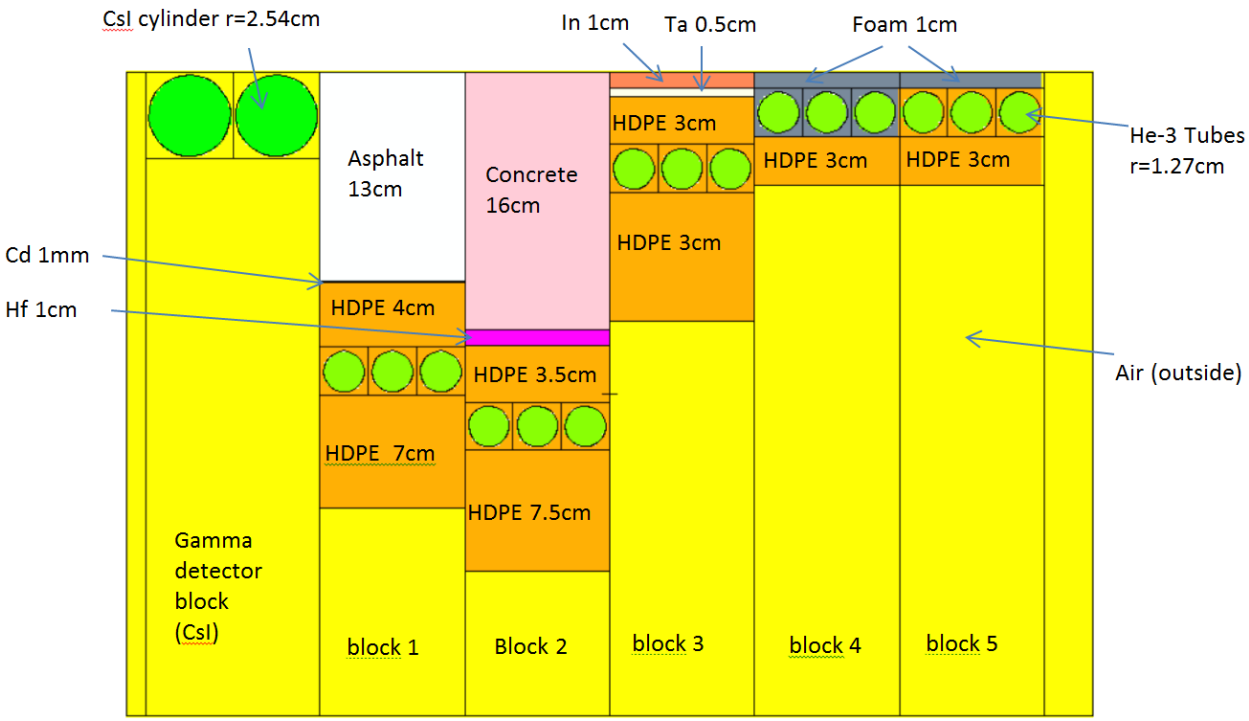

Figure 6.1: Original MPVS Design *x-y* View – CsI cylindrical detectors and He-3 neutron detectors without collimation. Note: the neutron module designs were derived from an in-depth analysis for neutron spectroscopy for a high speed SNM source detection system from a project funded at Georgia Tech by NNSA (Transport Simulation and Validation of a Synthetic Aperture SNM Detection System ("T-SADS")).

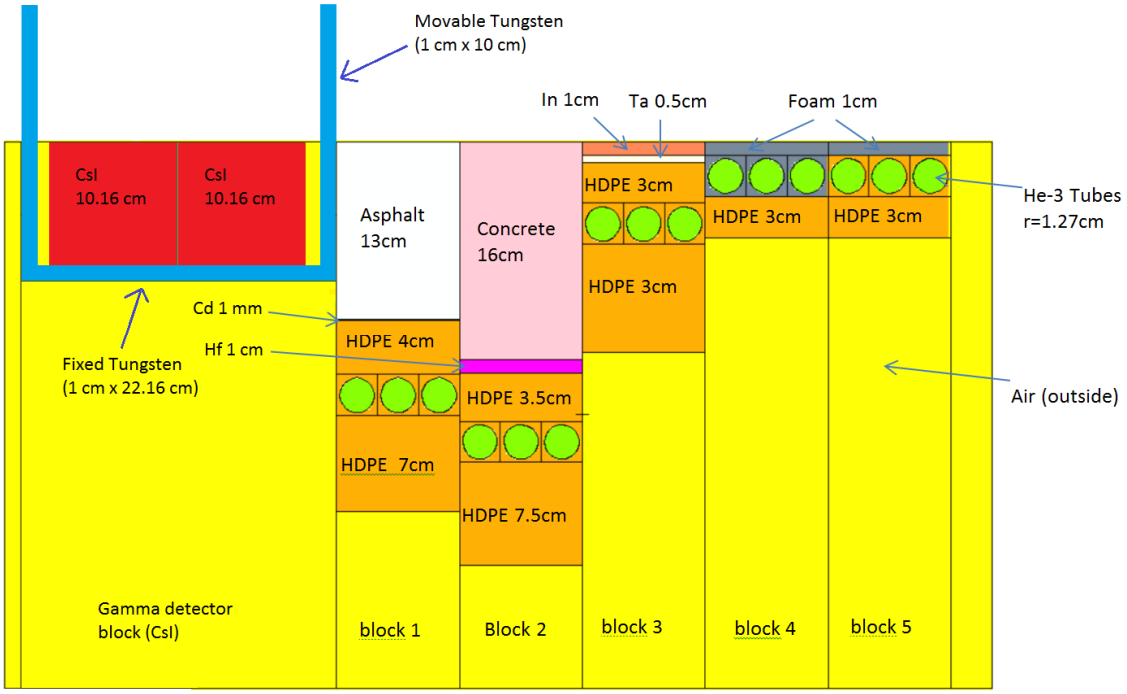

Figure 6.2: Revised MPVS Design XY View – CsI block detectors and He-3 neutron detectors with fixed and movable collimation (1 cm thick collimator shown).

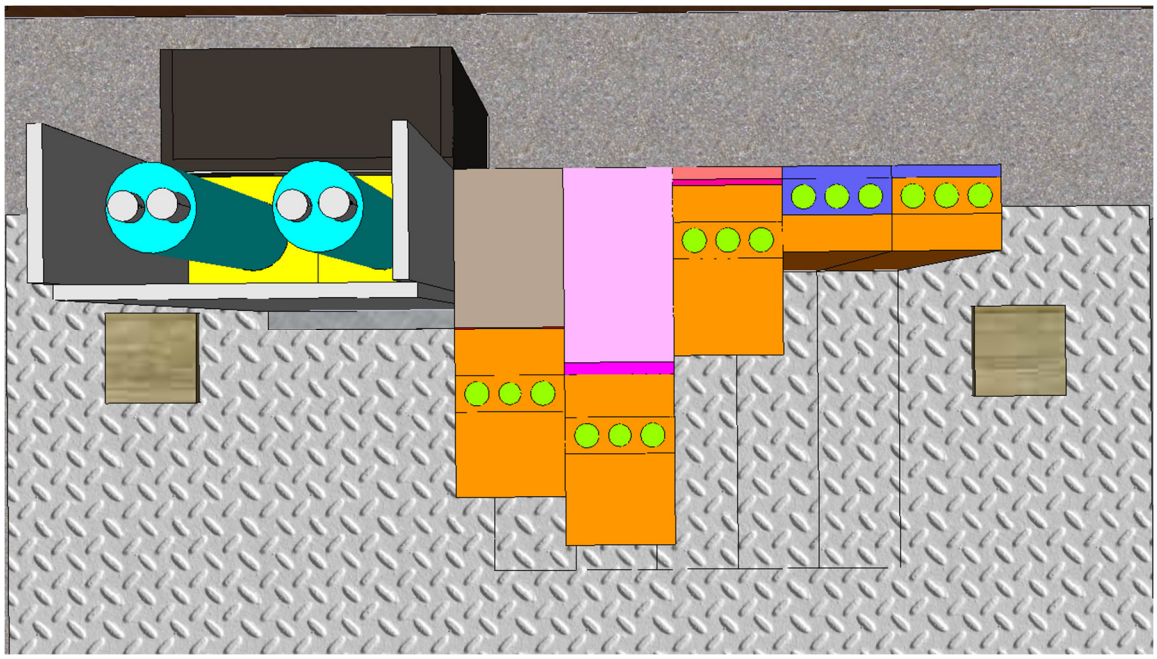

Figure 6.3: Detailed x-y view of 3-D Rendering of CsI block detectors and T-SADS neutron block.

6.2. Detector Specifications

Table 6.2 gives volumetric and mass information on all the components used to design the MPVS, assuming a collimation length of 10 cm. Table 6.3 can be used to correlate source-detector distance and collimation length with angular FOV and linear FOV. This is useful when different scenarios arise (different source-detector distances) so that collimation lengths can be adjusted accordingly.

Table 6.2: Component material specifications for a single unit detector with 10 cm long, 1 cm thick Tungsten collimator.

Component	Volume (cm^3)	Density (g/cm^3)	Mass (g)
CsI(Tl) (pair of 4 × 4 × 8 in^3)	4195.088	4.510	18920
Tungsten (4 slabs 1 cm × 10 cm × 22.32 cm); 1 slab 1 cm × 22.16 cm × 22.32 cm)	1140.797	19.350	20579.97
Helium-3	180.6	5.4788×10^{-4}	0.09895
Cadmium	184.5	8.5	1568
Polyethylene	1512	0.95	1436
Tantalum	135	16.6	2241
Indium	270	7.3	1971
DOW™ Foam	1197.987	0.035	41.92
Asphalt	1560.9	2.115	3301
Concrete	4320	2.3	9936
Hafnium	270	13.31	1797
Total	14543.78	-----	56897.2

Table 6.3: Component material specifications for a single unit detector with 10 cm long, 5 cm thick Tungsten collimator.

Component	Volume (cm^3)	Density (g/cm^3)	Mass (g)
CsI (pair of 4 × 4 × 8 in^3)	20471.8464	4.51	92328.03
Tungsten (4 slabs 5 cm × 10 cm × 22.32 cm); 1 slab 5 cm × 22.16 cm × 22.32 cm)	717.709	19.35	13887.67
He-3	180.6	0.00054788	0.098947
Cd	184.5	8.5	1568.25
Poly	1512	0.95	1436.4
Ta	135	16.6	2241
In	270	7.3	1971
Dow	1197.987	0.035	41.92955
Asphalt	1560.9	2.115	3301.304
Concrete	4320	2.3	9936
Hf	270	13.31	3593.7
Total	30820.5424	----	130305.4

Table 6.4: Linear FOV as Function of Source-Detector Distance and Movable Collimator Length. Note that the Linear FOV must be smaller than the inter-source spacing for collimation to be effective. Also note that as the source-detector distance increases, the detected counts will drop by roughly 10%. Significant drops (50-100%) in total counts detected may occur as the collimation length increases.

Source-Detector Distance (cm)	Movable Collimator Length (cm)	Angular FOV (degrees)	Linear FOV (cm)
30	5	49.8157	71.04
30	10	30.6255	35.52
30	15	21.5375	23.68
30	20	16.4888	17.76
40	5	49.8157	94.72
40	10	30.6255	47.36
40	15	21.5375	31.57
40	20	16.4888	23.68
50	5	49.8157	118.4
50	10	30.6255	59.20
50	15	21.5375	39.46
50	20	16.4888	29.60

Table 6.5: Time gating interval (s) as a Function of Speed, Collimator Length, and Source-Detector Distance. Green to Red axis indicates length of time on a relative color gradient (where green indicates longer time gating intervals).

Source-Detector Distance (cm)	Collimator Length (cm)	Speed (mph)				
		1	2	3	4	5
30	5	0.928778	0.464389	0.309593	0.232195	0.185756
	10	0.464389	0.232195	0.154796	0.116097	0.092878
	15	0.309593	0.154796	0.103198	0.077398	0.061919
	20	0.232195	0.116097	0.077398	0.058049	0.046439
40	5	1.23837	0.619186	0.41279	0.309593	0.247674
	10	0.619186	0.309593	0.206395	0.154796	0.123837
	15	0.41279	0.206395	0.137597	0.103198	0.082558
	20	0.309593	0.154796	0.103198	0.077398	0.061919
50	5	1.54796	0.773982	0.515988	0.386991	0.309593
	10	0.773982	0.386991	0.257994	0.193495	0.154796
	15	0.515988	0.257994	0.171996	0.128997	0.103198
	20	0.386991	0.193495	0.128997	0.096748	0.077398

6.3. List of Components

- One Baggage Tug – 3000 lbm (1360.78 kg) draw bar pull
- One Four-Wheeled Flatbed Cart – 3000 lbm (1360.78 kg) Capacity
- Two 4 × 4 × 8 inch^3 CsI detectors (10.16 cm × 10.16 cm × 20.32 cm)
- Two Photomultiplier Tubes & Associated Electronics
- Fifteen Helium-3 cylindrical detectors (radius = 1.27 cm, height = 30 cm)
- Five Fixed Tungsten Slabs
    - Back Plate: 22.16 cm × 5 cm × 22.32 cm
    - Side Plates: 5 cm × 10.16 cm × 22.32 cm
    - Top & Bottom Plate: 22.16 cm × 5 cm × 5 cm
- Four Modular Tungsten Slabs (the Y value can be changed as needed)
    - Side Plates: 5 cm × 10 cm × 22.32 cm
    - Top & Bottom Plate: 22.16 cm × 10 cm × 22.32 cm
- High Density Polyethylene
    - Four slabs: 9 cm × 3 cm × 30 cm. Note that one slab has three 1.27 cm radius holes for He-3.
    - One slab: 9 cm × 3 cm × 30 cm
    - One slab: 9 cm × 3.5 cm × 30 cm
    - One slab: 9 cm × 7.5 cm × 30 cm
    - One slab: 9 cm × 7 cm × 30 cm
    - One slab: 9 cm × 4 cm × 30 cm
- NRC-Regulatory Concrete: 9 cm × 16 cm × 30 cm
- Asphalt: 9 cm × 13 cm × 30 cm
- Indium: 9 cm × 1 cm × 30 cm
- Tantalum: 0.5 cm × 1 cm × 30 cm
- Cadmium: 9 cm × 0.1 cm × 30 cm
- Hafnium: 9 cm × 1 cm × 30 cm

6.4. Conclusions

The previous sections have outlined most of the components required to assemble a prototype MPVS platform. The system should maintain its robustness if many detectors are chained together even with the heavy tungsten plates as the mass of each detector system is approximately 130.5 kg, about 1/10th of the draw bar weight of a typical baggage tug.

6.5. Additional Figures

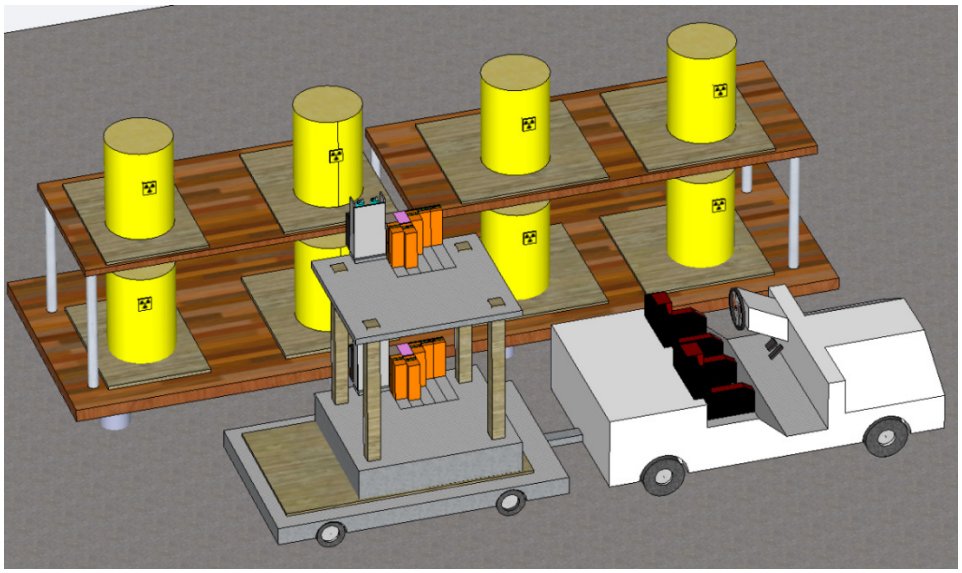

Figure 6.4: Isotropic view of the entire MPVS system, including baggage tug.

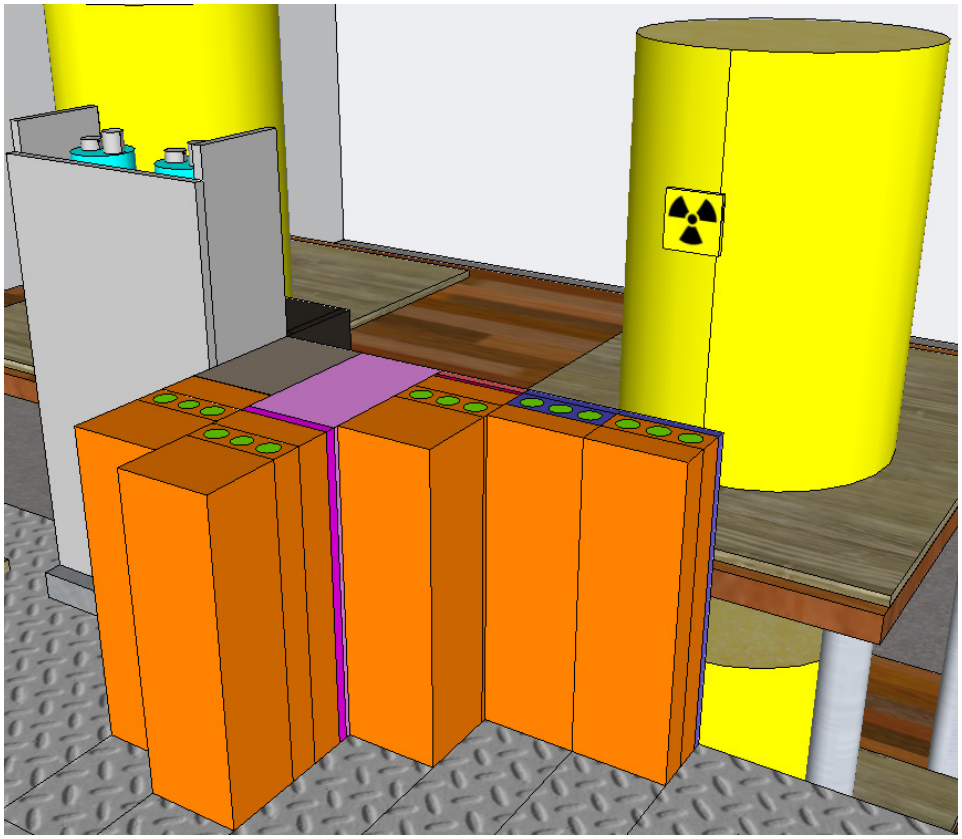

Figure 6.5: Isometric view of the source from the detector block.

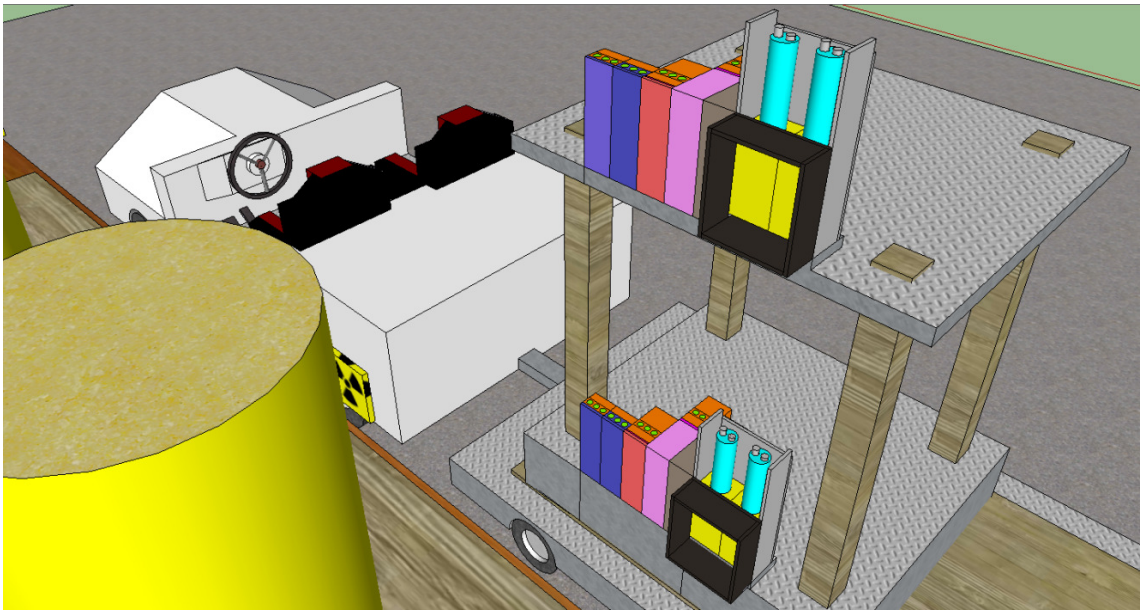

Figure 6.6: Isometric view of the MPVS detector. Detector blocks are numbered 5 to 1 from left to right, with the gamma block at rightmost with PMTs attached.

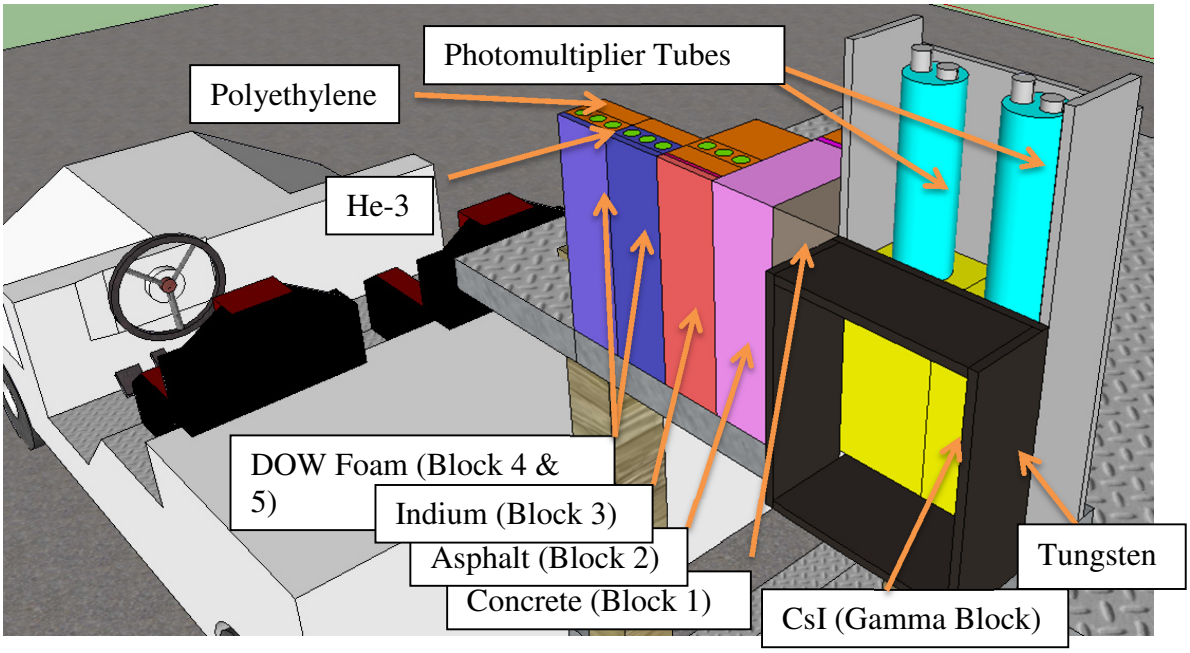

Figure 6.7: Detailed Isometric view of the MPVS detector. Detector blocks are numbered 5 to 1 from left to right, with the gamma block at rightmost with PMTs attached. Note there is a thin 1 mm Cadmium layer not shown in Block 1.

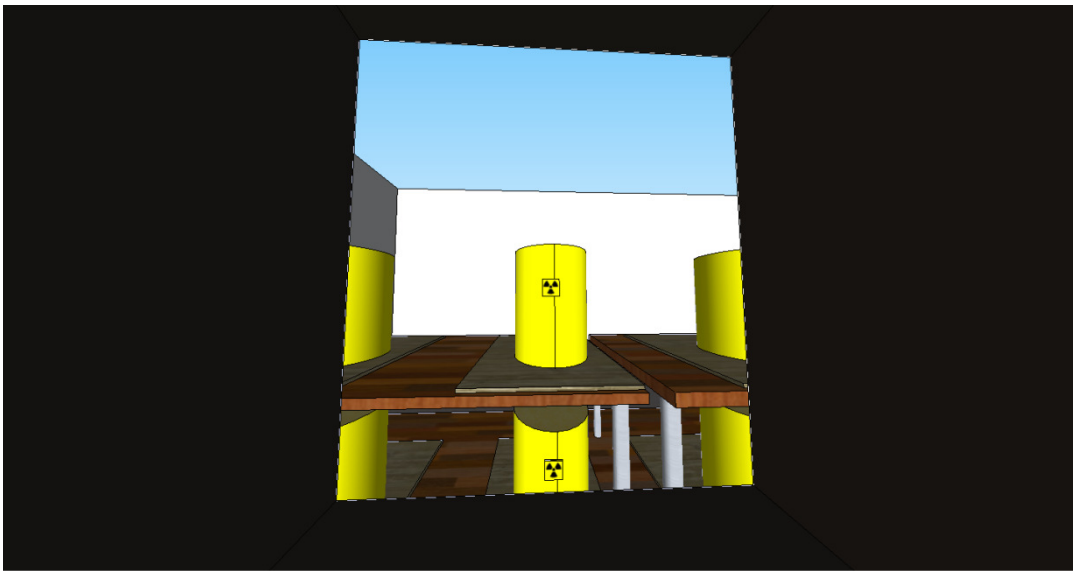

Figure 6.8: View of the source as seen from the CsI gamma detector (the "Adjoint" view).

Chapter 7: Conclusions and Future Work

7.1. Conclusions

This thesis presents the analytical and computational basics required to construct a T-SADS neutron detector block with CsI gamma detectors for the purposes of SNM verification. The optimized design for most situations, as mentioned in Chapter 6, is a $4 \times 4 \times 8$ in^3 CsI(Tl) scintillating gamma detector with 10 cm long and 5 cm thick tungsten collimators surrounding the gamma detector operating at a nominal 2 mph to accurately determine count rates for HEU of various ages and geometries.

Emphasis was placed on optimizing collimation for high energy photons inside the FOV of the detector in Chapter 4 in addition to providing a comprehensive framework for future analysis with source terms for common aged SNM in Chapter 3. Forward and adjoint deterministic transport was utilized for much of the analysis presented here in addition to stochastic Monte Carlo methods, shown also in Chapter 4. Good agreement was observed between the various forward and adjoint surface and volume cases, and likewise observed between the MCNP and PENTRAN scenarios (where direct computational equivalence existed).

Chapter 6 provides the final specifications for a MPVS with most of the components outlined. It should be possible from this analysis and Jessica Paul's neutron age-since-separation work, to build this system and perform field tests based on this work.

7.2. Future Work

There are multiple ways in which this analysis can be expanded. Applying the gamma ratio technique for WGPu using adjoint and forward detector response with

appropriate time gating is another way to validate the presence of SNM. Furthermore, applying the uncollided flux at multiple locations could be done to determine an effective Transport Correction Function in order to pre-compute most of the radiation transport beforehand in order to accurately verify the presence of aged SNM (or unknown age if the gamma ratio technique is used). Field-testing of the prototype MPVS and validation with theoretical and computational results would also be a promising avenue to pursue. Various ways of spoofing the SNM signature with alternative actinides is also an open question: is it possible to create a false positive signal by changing the shielding materials or adjusting the isotopic contributions of various sources? How will this vary the mass estimates compared to 1 SQ of HEU or WGPu?

Recent work from Dr. Scottie Walker [41] on an alternative for He-3 neutron detectors (using materials such as BF_3) for the T-SADS neutron blocks can also make this mobile system more robust given the current shortage in He-3 stockpiles. This would also have the side effect of making this system more affordable for end users.

If possible, leveraging these techniques could provide a valuable method of determining SNM on the fly and could have multiple applications within the field of nuclear non-proliferation and safeguards. The MPVS system, if built, could be a useful asset for agencies such as the United States State Department, the U.S. Department of Homeland Security, and the International Atomic Energy Agency.

REFERENCES

[1] J. C. Fahrenholtz, "Development of an automated pit packaging system for Pantex," SAND--97-2163; Other: ON: DE98000061; TRN: TRN: 97:005374, 1997.

[2] L. E. Fischer, R. F. Hafner, J. Hovingh, S. C. Keeton, E. W. Russell, and J. Lemmings, "Conceptual designs for the AT-400MO package," UCRL-ID--126191; Other: ON: DE98050702, 1997.

[3] S. M. Bowman, J. E. Horwedel, I. C. Gauld, and D. Barnett, "ORIGEN-ARP: a new windows pc package for ORIGEN users," in *American Nuclear Society, 12 th Biennial RPSD Topical Meeting, Santa Fe, New Mexico*, 2002.

[4] L. J. Lorence, "CEPXS/ONELD Version 2.0: A discrete ordinates code package for general one-dimensional coupled electron-photon transport," *Nuclear Science, IEEE Transactions on,* vol. 39, pp. 1031-1034, 1992.

[5] M. Fritz, "CSR MATERIAL SAFETY DATA SHEET (MSDS): CELOTEX Mineral Fibre Ceiling Products (Hytone)," F. C. Systems, Ed., ed. Chatswood, Australia, 2008.

[6] G. Bell and S. Glasstone, *Nuclear Reactor Theory*: Van Nostrand Reinhold Company, 1970.

[7] G. F. Knoll, *Radiation Detection and Measurement*, 4 ed. United States of America: Wiley, 2010.

[8] G. Sjoden, J. Maniscalco, and M. Chapman, "Recent Advances in the Use of ASEDRA in Post Processing Scintillator Spectra for Resolution Enhancement," *Journal of Radioanalytical and Nuclear Chemistry,* vol. 291, pp. 365-371, 2012.

[9] G. Sjoden and C. Yi, "Transport Simulation and Validation of a Synthetic Aperture SNM Detection System ("T-SADS") July Quarterly Report," Georgia Institute of Technology, Georgia Institute of Technology2012.

[10] D. J. Mitchell and P. L. George, "Calculation of Background Radiation for Gamma-Ray and Neutron Detectors," *Sandia Rep. SAND2008-4478,* 2008.

[11] J. F. Ziegler, "Terrestrial cosmic rays," *IBM journal of research and development,* vol. 40, pp. 19-39, 1996.

[12] J. N. Paul, "Exploiting Passive Gamma Signals from Weapons Grade Plutonium and Highly Enriched Uranium for Weapons Pit Storage," Masters of Science, Nuclear Engineering and Medical Physics, Georgia Institute of Technology, Atlanta, GA, 2013.

[13] M. Molinar, "SNM Neutron Detection Using a Time-Gated Synthetic Aperture Hybrid Approach," Masters of Science in Nuclear Engineering Masters, Woodruff Department of Mechanical Engineering, Georgia Institute of Technology, Atlanta, GA, 2013.

[14] AL-BASHEER, #160, A. K., SJODEN, G. E., GHITA*, et al.*, *CRITICAL DISCRETIZATION ISSUES IN 3-D S[N] SIMULATIONS RELEVANT TO DOSIMETRY AND MEDICAL PHYSICS* vol. 169. La Grange Park, IL, ETATS-UNIS: American Nuclear Society, 2010.

[15] E. E. Lewis and W. F. Miller, *Computational Methods of Neutron Transport*: Wiley-Interscience, 1993.

[16] G. Longoni and A. Haghighat, "Development of new quadrature sets with the 'ordinate splitting'technique," in *Proc. of Int. Meeting on Mathematical Methods For Nuclear Application, Salt Lake City, Utah, September*, 2001.
[17] B. Petrovic and A. Haghighat, "New Directional Theta-Weighted Sn Differencing Scheme," *Transactions of the American Nuclear Society,* vol. 73, pp. 195-197, 1996.
[18] K. Mathews, G. Sjoden, and B. Minor, "Exponential characteristics spatial quadrature for discrete ordinates radiation transport in slab geometry," *Nuclear Science and Engineering;(United States),* vol. 118, 1994.
[19] G. Sjoden and A. Haghighat, "PENTRAN-Parallel Environment Neutral-particle TRANsport in 3-D Cartesian Geometry," in *Proc. Int. Conf. on Mathematical Methods and Supercomputing for Nuclear Applications*, 1997, pp. 232-234.
[20] G. Sjoden and A. Haghighat, "A New Adaptive Differencing Strategy in the PENTRAN 3-D Parallel Sn Code," *Transactions of the American Nuclear Society,* vol. 75, 1996.
[21] M. C. Team, "MCNP–A General Monte Carlo N-Particle Transport Code, Version 5," *Book MCNP-A General Monte Carlo N-Particle Transport Code Version,* vol. 5, 2003.
[22] N. Tsoulfanidis and S. Landsberger, *Measurement and Detection of Radiation*, 3 ed. Boca Raton: CRC Press, 2011.
[23] J. MANISCALCO and G. SJODEN, "RADIOACTIVE ANOMALY DISCRIMINATION FROM SPECTRAL RATIOS," US Patent App. 13/338,538 Patent, 2011.
[24] M. C. Higginson, "Westinghouse Hanford Company Special Nuclear Material Vault Storage Study," in *Westinghouse Hanford Company*, U. S. D. o. Energy, Ed., 1 ed, April 1996.
[25] I. A. E. Agency, *IAEA Safeguards Glossary* vol. 3. Vienna, Austria, 2001.
[26] L. F. Hansen, "A Comparison of the Shielding Performances of the AT-400A, Model FL, and Model AL-R8 Containers," in *Defense Programs 2nd Annual Packaging Workshop*, San Francisco, CA, June 1995.
[27] S. Couture and R. Hafner, "Celotex replacement study," *Lawrence Livermore National Laboratory Report UCRL-ID-151168,* 2002.
[28] A. Diaz-Ortiz, J. Stolk, J. Kim, J. Sanchez, and A. Manthiram, "Characterization of celotex and thermodynamic calculations of the formation of corrosion precursors on beryllium," Amarillo National Resource Center for Plutonium, TX (United States)1999.
[29] W. C. Quirk, June; Kirvel, Robert D.; Vore, Lauren de; Kroopnik, Harriet; Gleason, Kevin; McElroy, Lori, *Dismantling the Cold War Arsenal*. Springfield, Virginia: Lawrence Livermore National Laboratory, November-December 1993.
[30] S. M. Bowman, "SCALE 6: Comprehensive Nuclear Safety Analysis Code System," *Nuclear Technology,* vol. 174, pp. 126-148, 2011.
[31] J. E. White, "Bugle-96: Coupled 47 Neutron, 20 Gamma-Ray Group Cross Section Library Derived from ENDIF-B-VI for LWR Shielding and Pressure Vessel Dosimetry Applications," vol. DLC-185 D00185 ALLCP 00, ed: RSICC Data Library Collection, March 1996.

[32] D. E. Reilly, Norbert; Smith, Hastings, "PANDA - Passive Nondestructive Assay of Nuclear Materials," U. S. N. R. C. Office of Nuclear Regulatory Research, Ed., ed. Washington, D.C., March 1991.
[33] "The Modern Pit Facility (MPF)," *American Physical Society Panel on Public Affairs,* April 2004.
[34] O. R. N. Laboratory, "CEPXS - One Dimensional Coupled Electron-Photon Multigroup Discrete Ordinates Code System," ed: RSICC Data Library Collection and UT-Battelle, 2001.
[35] O. R. N. Laboratory, "SCALE6," vol. C00785 MNYCP 00, 6.0 ed: RSICC Data Library Collection, 2009, p. A Comprehensive Modeling and Simulation Suite for Nuclear Safety Analysis and Design; Includes ORIGEN (Source & Executables).
[36] B. Weiss and R. Stickler, "Phase instabilities during high temperature exposure of 316 austenitic stainless steel," *Metallurgical and Materials Transactions B,* vol. 3, pp. 851-866, 1972.
[37] C. Yi and A. Haghighat, "PENMSHXP Manual, Version 2.5 b," *Univ. of Florida,* 2008.
[38] M. Chin, J. Paul, and G. Sjoden, "Source Term Characterization for SNM Pit Storage Facilities," presented at the PHYSOR 2012 – Advances in Reactor Physics – Linking Research, Industry, and Education, Knoxville, TN, 2012.
[39] G. Sjoden, "Deterministic adjoint transport applications for He-3 neutron detector design," *Annals of Nuclear Energy,* vol. 29, pp. 1055-1071, 2002.
[40] J. Paul, M. Chin, and G. Sjoden, "Source Term Characterization for SNM Pit Storage Facilities," *Journal of Nuclear Materials Management,* vol. 638, p. 11, 2012.
[41] S. Walker, "Spectrally-Matched Neutron Detectors Designed Using Computational Adjoint Sn for Plug-In Replacement of He-3," Doctorate of Philosophy in Nuclear Engineering, Nuclear and Radiological Engineering, Georgia Institute of Technology, Atlanta, Georgia, 2013.
[42] J. Duderstadt and L. Hamilton, *Nuclear Reactor Analysis*: Wiley, 1976.
[43] M. J. Berger, J. H. Hubbell, S. M. Seltzer, J. Chang, J. S. Coursey, R. Sukumar*, et al.*, "XCOM: Photon Cross Section Database," N. I. o. S. a. T.-R. a. B. P. Division, Ed., 8 ed, 1998.
[44] C. Yi, J. Paul, and G. Sjoden, "SYNTHETIC SCORING SCHEME FOR ISOTOPE IDENTIFICATION IN SMARTID," presented at the International Nuclear Materials Management, Palm Desert, California, 2013.
[45] H. A. Smith and M. Lucas, "Passive Non-Destructive Assay (PANDA) Manual," LA-UR-90-732, Ed., ed: Los Alamos National Laboratory 2007, pp. 58-62.
[46] C. Edgar, C. Yi, and G. Sjoden, "GAMMA RESPONSE IN A SYNTHETIC APERTURE SYSTEM FOR ROADSIDE
DETECTION OF SPECIAL NUCLEAR MATERIAL," presented at the International Nuclear Materials Management 2013, Palm Desert, California, 2013.
[47] M. Chin, K. Manalo, C. Edgar, J. Paul, M. Molinar, E. Redd*, et al.*, "Optimization of Multi-Group Cross Sections for Fast Reactor Analysis," *International Conference Mathematics and Computational Methods Applied to Nuclear Science and Engineering,* 2013.